Development of analysis tools for gamma-ray spectrometry

Jiaxin Xu

université
PARIS-SACLAY

Development of analysis tools for gamma-ray spectrometry

Thèse de doctorat de l'université Paris-Saclay

École doctorale n° 580, sciences et technologies de l'information et de la communication (STIC)
Spécialité de doctorat: Traitement du signal et des images
Unité de recherche: Université Paris-Saclay, CEA, Département d'Electronique des Détecteurs et d'Informatique pour la Physique, 91191, Gif-sur-Yvette, France.
Référent: Faculté des sciences dOrsay

Thèse présentée et soutenue en visioconférence totale, le 25/11/2020, par

JIAXIN XU

Composition du jury:

Thomas Rodet Professeur, ENS Paris-Saclay	Président
Jean-François Giovannelli Professeur, Université de Bordeaux	Rapporteur & Examinateur
Michel Paindavoine Professeur, Université de Bourgogne	Rapporteur & Examinateur
Biagio Zaffora Ingénieur de recherche, CERN	Examinateur
Mai Nguyen-Verger Professeur, Université de Cergy	Examinatrice
Jérôme Bobin Chercheur, CEA Saclay	Directeur de thèse
Anne De Vismes Ott Chercheur, IRSN	Invitée
Christophe Bobin Chercheur, CEA Saclay	Invité

Thèse de doctorat

NNT: 2020UPASG030

Remerciements

Je tiens tout d'abord à remercier les rapporteurs de la thèse Jean-François Giovannelli et Michel Paindavoine, pour leur lecture attentive de ma thèse. Je tiens à remercier Thomas Rodet d'avoir accepté d'être président du jury. Je remercie également tous les membres du jury d'avoir accepté d'assister à la présentation de ce travail.

Je tiens à remercier mon directeur de thèse, Jérôme Bobin et ma tutrice de thèse, Anne De Vismes Ott, qui m'ont apporté un encadrement exceptionnel tout au long de ces trois ans de thèse. Les discussions que nous avons eues ainsi que leurs conseils sont pour beaucoup dans le résultat final de ce travail. Je remercie également Christophe Bobin et Rémi André pour leurs aide et collaboration.

Je voudrais aussi remercier les membres de l'équipe du LMRE, ainsi que Christophe Ardois, le chef de laboratoire, de m'y avoir accueilli chaleureusement avec les meilleures conditions de travail. Je pense plus particulièrement à l'équipe gamma, pour leur aide et partage des expériences en spectrométrie gamma.

J'ai également apprécié le temps passé au sein du groupe CosmoStat. Particulièrement pour tous les thésards avec qui j'ai partagé beaucoup de bons moments.

Enfin, merci à mes amis et ma famille, qui m'ont apporté leur soutien moral pendant ces années d'études.

Résumé

Dans le cadre de la mission de surveillance radiologique de l'environnement de l'Institut de Radioprotection et de Sûreté Nucléaire (IRSN), le Laboratoire de métrologie de la radioactivité dans l'environnement (LMRE) effectue des mesures de la radioactivité des échantillons prélevés dans l'environnement afin d'identifier et quantifier les radionucléides, naturels et artificiels. La radioactivité dans les échantillons de l'environnement est, entre autres techniques, mesurée par spectrométrie gamma, mesure rapide, non-destructive et multi-élémentaire. L'objectif de la thèse est d'améliorer les performances de cette technique, en particulier en termes de limites de détection, en proposant de nouvelles méthodes d'analyse, qui permettent de rendre la détection des radionucléides plus sensible. Cette sensibilité accrue permet d'atteindre les niveaux traces des radionucléides artificiels rencontrés dans les mesures de routine, mais également d'avoir des mesures plus courtes, ce qui est particulièrement intéressant en situation de crise.

Contexte de la thèse

Le contexte des mesures de la radioactivité de l'environnement par spectrométrie gamma est présenté dans le chapitre 2. Un spectre est la distribution en fréquence des dépôts d'énergie dans le détecteur due aux photons incidents. Il est composé, pour un photon d'énergie E, d'un pic d'absorption totale à l'énergie E, ainsi qu'un fond continu, appelé fond Compton, à plus basse énergie. Un radionucléide pouvant émettre plusieurs photons, le spectre individuel du radionucléide est composé de plusieurs pics et fonds associés. Enfin, un échantillon de l'environnement contient plusieurs radionucléides induisant un spectre complexe qui est la somme des spectres individuels des radionucléides.

L'analyse d'un spectre gamma est habituellement basée sur l'étude des pics : les énergies des pics pour identifier les radionucléides et le nombre d'événements dans les pics pour quantifier l'activité de chaque radionucléide. Cependant, cette approche présente des limitations, car elle n'exploite que

les informations des pics et elle ne prend pas en compte la statistique de Poisson du processus physique de la détection. Dans le cadre de la thèse, nous proposons de prendre en compte le spectre de chaque radionucléide dans sa globalité, qui permet d'utiliser l'ensemble de l'information disponible dans toute la gamme d'énergie, ainsi que la statistique de Poisson du modèle.

Démélange spectral

Dans le chapitre 3, nous proposons d'analyser des spectres gamma par le démélange spectral, qui consiste à séparer un spectre gamma en spectres individuels des radionucléides. Considérant le spectre comme un vecteur, l'estimation des activités des radionucléides consiste à estimer les poids de mélange associés aux signatures spectrales des radionucléides. D'un point de vue mathématique, ce problème peut s'écrire comme un problème inverse régularisé, les signatures spectrales étant connues, le démélange spectral est d'abord étudié avec une contrainte de non-négativité.

Les expériences sur les spectres simulés démontrent que, comparé aux estimateurs des moindres carrés, le démélange spectral basé sur la statistique de Poisson permet d'améliorer la précision de l'estimation avec des biais d'estimation et des incertitudes plus faibles. L'analyse d'un spectre dans sa globalité est plus efficace que les méthodes basées sur les pics, en particulier pour les radionucléides dont les spectres sont fortement corrélés. La méthode présente également une amélioration de la sensibilité lors de l'analyse des mesures d'échantillons de filtres d'aérosols, où la méthode standard présente toujours des difficultés pour la détection de ^{137}Cs, un radionucléide présent à l'état de trace dans l'environnement. Le démélange spectral permet ainsi de diminuer le temps nécessaire à sa détection de 8 jours à 4 jours.

En pratique, l'ensemble des radionucléides présents dans un échantillon de l'environnement n'est jamais parfaitement connu. Le démélange avec un ensemble supposé de radionucléides plus grand ou plus petit que ceux réellement présents peut générer des biais de l'estimation, ainsi que de fausses identifications de radionucléides qui ne sont pas présents dans l'échantillon. Ceci nécessite la sélection de modèle de la combinaison linéaire des signatures spectrales. Pour ce faire, dans le chapitre 4, nous proposons d'estimer conjointement l'ensemble des radionucléides actifs et leur poids de mélange. Cette approche appelée démélange spectral parcimonieux est étudiée afin de trouver le plus petit ensemble de radionucléides qui permet d'expliquer le spectre mesuré. Pour ce faire, nous proposons un nouvel algorithme OMP (Orthogonal Matching Pursuit) basé sur la statistique de Poisson. Cet algorithme sélectionne séquentiellement le radionucléide qui maximise la vraisemblance

de Poisson et estime les poids de mélange des radionucléides sélectionnés avec l'algorithme de démélange spectral.

Nous montrons que l'algorithme du démélange spectral parcimonieux proposé permet d'améliorer la précision de l'estimation en limitant les fausses identifications et diminue les biais de l'estimation pour les radionucléides actifs.

Utilisation métrologique du démélange spectral

Dans les chapitres 3 et 4, les études sont effectuées sur l'analyse des spectres gamma par le démélange spectral. En général, l'utilisation métrologique d'un algorithme d'analyse nécessite l'évaluation des limites caractéristiques pour la prise de décision et l'étalonnage du détecteur pour l'analyse quantitative des résultats.

Nous nous concentrons essentiellement sur deux limites caractéristiques dans le chapitre 5: le seuil de décision et les limites de l'intervalle de confiance. i), Le seuil de décision (SD) permet de décider si un radionucléide est présent ou non. Le SD associé à un certain taux de faux positif pour un radionucléide est déterminé par un test statistique basé sur le fond équivalent estimé dans le modèle de démélange spectral. ii), Nous proposons également d'estimer les intervalles de confiance à partir de la matrice de Fisher. La variance de la distribution de l'estimation est approximée par l'inverse de la matrice de Fisher. Ces approches sont évaluées avec les spectres gamma simulés, ceci permet de valider leurs applications pour analyser les spectres de mesure.

Dans le chapitre 6, l'étalonnage est étudié pour un détecteur du laboratoire en utilisant le démélange spectral. L'étalonnage en rendement de détection et en résolution consiste à ajuster le modèle de simulation pour que les signatures spectrales simulées reproduisent les réponses expérimentales. Le ré-étalonnage en énergie permet de corriger le décalage en énergie des signatures spectrales simulées. Ces étapes d'étalonnage sont évaluées et validées avec une source d'étalonnage dont les activités sont connues.

Les résultats obtenus pour les mesures expérimentales montrent que la nouvelle méthode démélange spectral est plus sensible que l'analyse standard, plus particulièrement pour la détection et la quantification des radionucléides à faible niveau.

Contents

1 Introduction **1**

2 Context of the radioactivity measurements with gamma-ray spectrometry **5**

2.1 Environment radioactivity measurements 6
2.1.1 The radioactivity phenomenon 6
2.1.2 Why measuring radioactivity in the environment ? . . 7
2.1.3 Quantitative analysis with gamma-ray spectrometry . . 8
2.1.4 Gamma-ray spectrometry measurements in the laboratory 11
2.2 Description of gamma-ray spectra 12
2.2.1 Detectors and data acquisition 12
2.2.2 Photon interactions with matter 13
2.2.3 Gamma-ray spectrum contributions 15
2.3 Improvement of the detection limits with gamma-ray spectrometry 16
2.4 State of the art of gamma-ray spectrum analysis 17
2.4.1 Peak-based gamma-ray spectrum analysis 17
2.4.2 Full spectrum analysis 19
2.4.3 Machine learning algorithm in gamma-ray spectrum analysis 20
2.4.4 Conclusion 20

3 Spectral unmixing **23**

3.1 From statistical modeling to an optimization problem 25
3.2 Spectral unmixing algorithms 27
3.2.1 Least squares unmixing algorithm 27
3.2.2 Poisson statistics-based unmixing algorithms 30
3.3 Experiments on the combination of two radioactive sources . . 32
3.3.1 Experiments on simulations of HPGe detector 32
3.3.2 Experiments on simulations of NaI detector 33

3.3.3 Results on two radioactive sources mixture 34
3.4 Realistic simulations of routine aerosol samples 35
3.4.1 Convergence rate of algorithms 38
3.4.2 Comparisons of the unmixing algorithms in different counting regimes 41
3.4.3 Evaluation of unmixing algorithms for low-level artificial radionuclide 41
3.5 Experimental results with real spectra from aerosol samples' measurements 44
3.5.1 Dimension of the spectral dictionary 45
3.5.2 Comparisons with peak-based analysis 50
3.6 Discussion 54

4 Sparse spectral unmixing 57
4.1 A model selection approach 58
4.2 Sparse solution 60
4.3 Greedy algorithm to identify active radionuclides 61
4.3.1 Greedy algorithms in least squares problem 61
4.3.2 The Poisson OMP Algorithm 61
4.3.3 Stopping criteria for radionuclides identification 62
4.4 Application of $\mathcal{P}$-OMP to HPGe measurements 65
4.4.1 Data description 65
4.4.2 Evaluation on simulated spectra 65
4.4.3 Evaluation on measured spectra 67
4.5 Application of $\mathcal{P}$-OMP to NaI measurements 68
4.5.1 Description of the data 68
4.5.2 Application to NaI measurements - scenario I 69
4.5.3 Application to NaI measurements - scenario II 72
4.5.4 Application to NaI measurements - scenario III 74
4.5.5 Stopping rule, comparing the deviance-based test with information criteria 76
4.6 Summary of the sparse spectral unmixing 77

5 Characteristic limits in spectral unmixing 79
5.1 Characteristic limits in radioactivity measurements 80
5.2 Quantification with Monte Carlo simulations 82
5.3 Quantifying the decision threshold 85
5.3.1 Decision threshold in peak-based analysis 85
5.3.2 Decision threshold in spectral unmixing analysis 86
5.3.3 Evaluation of the decision threshold determination . . 89
5.4 Confidence interval 95

5.4.1 Fisher information to compute confidence intervals . . 95
5.4.2 Evaluation of confidence interval in spectral unmixing . 96
5.5 Discussion 98

6 Analysis of HPGe gamma-ray spectra measurements 101
6.1 Challenges of calibrations in gamma-ray spectrum analysis . . 102
6.1.1 Calibrations in peak based analysis 103
6.1.2 Towards calibrations for spectral unmixing 105
6.2 Efficiency calibration and resolution calibration in simulation process 106
6.2.1 Efficiency calibration 107
6.2.2 Resolution calibration in spectral unmixing 108
6.3 Complexity of the spectral signatures 109
6.4 Re-calibration of energy in spectral unmixing 110
6.5 Validation with the standard source analysis 116
6.6 Experiments on aerosol measurements 118
6.6.1 Uncertainty budget of the aerosol measurements . . . 118
6.6.2 Re-analysis of aerosol measurements 120
6.7 Conclusion 122

7 Conclusion and perspectives 127
7.1 Conclusion 127
7.2 Perspectives 129
7.2.1 Spectral unmixing with temporal signatures 129
7.2.2 Making profit of the past processed data, learn to unmix 133
7.3 Open questions 140
7.4 Publications 142

A Nuclear data of radionuclides 145

B Proximal algorithms for spectral unmixing 147
B.1 Optimization problem underlying the spectral unmixing 147
B.2 Proximal operators and proximal algorithms 148
B.2.1 Definition of the proximal operator 148
B.2.2 Proximal algorithms used in this work 148
B.2.3 Proximal operators calculation 150

C The MCNP simulation code 153

List of notations

General notations

$\boldsymbol{x}$	vector
x_i	the i^{th} entry of $\boldsymbol{x}$
$\boldsymbol{X}$	matrix
X_{ij}	the $[i,j]^{th}$ entry of $\boldsymbol{X}$
$\boldsymbol{x}_j$	the j^{th} column of $\boldsymbol{X}$
$\mathrm{diag}\,(\boldsymbol{x})$	diagonal matrix with diagonal elements: $x_1, ...x_n$
$\boldsymbol{X}^\dagger$	pseudo inverse matrix of $\boldsymbol{X}$

Specific notations of gamma-ray spectrum model

$\boldsymbol{x}$	$M \times 1$ column vector (measured spectrum)
$\boldsymbol{b}$	$M \times 1$ column vector (background spectrum)
$\boldsymbol{\Phi}$	$M \times N$ matrix (spectral signatures)
$\boldsymbol{a}$	$N \times 1$ column vector (mixing weights)
$-M$	number of channels
$-N$	number of radionuclides
$f(\boldsymbol{a})$	data fidelity term
$g(\boldsymbol{a})$	regularization term

Notations of radioactivity

${}^A_Z\mathrm{X}$	element symbol X
$A = N + Z$	mass number
Z	number of protons
N	number of neutrons
$T_{1/2}$	the half-life of a radionuclide
becquerel (Bq)	unit of activity

List of operators

$\|\boldsymbol{x}\|_0$	norm ℓ_0: number of non-zeros elements in $\boldsymbol{x}$
$\|\boldsymbol{x}\|_2$	spectral norm of $\boldsymbol{x}$, its largest eigenvalue
$\odot$	Hadamard product
$\nabla f(.)$	gradient of function f
$\text{prox}_{\rho h}(y)$	proximal operator of the function h defined in Appendix B.
$\mathcal{L}(x\|\theta)$	cost function, neg-log-likelihood ($f(x\|\theta)$ for likelihood)
$I_x(\theta)$	Fisher information

List of Abbreviations

HPGe	High Purity Germanium
NaI(Tl)	Sodium Iodide (Thallium doped)
ROI	Region of Interest
FSA	Full spectrum analysis
LS	least squares
WLS	weighted least squares
FBS	Forward Backward Splitting
OMP	Orthogonal Matching Pursuit
$\mathcal{P}$-OMP	Poisson-based Orthogonal Matching Pursuit
FPR	false positive rate
FNR	false negative rate
DT	decision threshold
DL	detection limit
CDF	cumulative distribution function

List of Constants and Units

Plank constant	$h = 6.62607004 \times 10^{-34}$ m^2 kg/s
Speed of light in vacuum	$c = 299,792,458$ m/s
Electronvolt	1 eV $= 1.602176634 \times 10^{-19}$ J
Becquerel	1 Bq = 1 disintegration per second

CHAPTER 1

Introduction

This thesis focuses on the development of analysis tools for gamma-ray spectrometry. Involved in the radioactivity monitoring work, gamma-ray spectrometry measurements need to be as sensitive and rapid as possible to provide timely and reliable information to the population and the authority. In this context, the study to improve the gamma-ray spectrum analysis has attracted more and more attention in the scientific community. The key contribution of this work is the solution it provides for the gamma-ray spectrum analysis.

In the first part of the thesis, we thoroughly investigate the spectral unmixing methods for gamma-ray spectrum analysis, as well as their applications to different types of measurements. Such methods have been evaluated with both synthetically generated data and experimental data. They present significant advantages in the task of providing more sensitive analysis than standard methods.

In the second part, we explore the metrological use of the investigated spectral unmixing methods. The accurate quantitative analysis requires the proper instrumentation calibrations and needs to cope with the standards in radioactivity measurements. Different metrological aspects of the quantitative analysis have been investigated and further applied to analyze experimental measurements performed in IRSN (French Institute for Radiation Protection and Nuclear Safety) laboratory/LMRE. The contribution of this thesis is as follows:

- In Chapter 2, we firstly present the environment radioactivity measurements with the gamma-ray spectrometry technique. Next, we introduce the gamma-ray spectrometry instrumentation, including the main components of a gamma spectrometer and specific installations in the laboratory. To better understand the features of a gamma-ray

spectrum (*i.e.*, data to be analyzed), we briefly discuss the photon interactions that characterize a gamma-ray spectrum. We end up with the review of the state-of-the-art studies in the field of gamma-ray spectrum analysis, where we present the existing analysis methods and their limitations.

- In Chapter 3, we start by overcoming the activity estimation with spectral unmixing techniques, which allows accounting for the full spectrum analysis of a gamma-ray spectrum. More precisely, we formulate the problem as a regularized inverse problem, where activities appear as mixing weights related to individual spectra (*i.e.*, spectral signatures) and the non-negativity constraint of the radionuclides' activities is taken into account. We investigate different approaches to solve the underlying spectral unmixing problem:

  - Standard least squares regression and re-weighted least squares regression that can better account for the Poisson statistics.
  - Poisson based spectral unmixing that takes into account the precise physical model underlying the detection process.

  Their estimation performances are evaluated as follows:

  - The algorithms are first applied to the experiments on gamma-ray spectra simulations of two radioactive sources, which enables us to compare the proposed approaches and better understand the limitations of standard gamma-ray spectrum analysis methods. As a result, the Poisson-based full spectrum analysis presents significant advantages with lower estimation errors and lower uncertainties.
  - Next, we further evaluate the estimation performances with realistic simulations of real data, and particularly the ability to estimate the low-level artificial radionuclides as a challenging issue in real data analysis.
  - Finally, the study on real data contains two aspects: i), assessing the impact of the spectral signatures' dictionary. ii), comparing the sensibility of the Poisson-based spectral unmixing to the standard method used in the laboratory. The main conclusion that can be drawn is that the Poisson-based spectral unmixing allows reducing the time to detect the low-level ^{137}Cs in environmental samples from 8 days to 4 days.

While providing promising results on both simulated and real data, the proposed Poison-based spectral unmixing analysis is however sensitive to the spectral signatures' dictionary, which requires the identification of active radionuclides present in the measurement.

- In Chapter 4, the identification of the spectral signatures' dictionary is further investigated, which amounts to finding the subset of active radionuclides present in a gamma-ray spectrum measurement. For this purpose, the spectral unmixing is extended to jointly estimate the subset of active radionuclides and their activities, which requires adding a model complexity penalty in the spectral unmixing.

  To identify the smallest subset of active radionuclides that best explains the measured spectrum, we investigate the spectral unmixing with a sparsity constraint. By reviewing available approaches that enforce the sparsity constraint in optimization problems, we propose the Orthogonal Matching Pursuit (OMP) algorithm that sequentially selects active radionuclides from a measured spectrum. However, the Poisson statistics of the gamma-ray spectrum data makes the selection procedure difficult. We propose a novel Poisson-based OMP algorithm. Such a greedy sparse regression method sequentially selects the radionuclide that maximizes the Poisson likelihood and stops selecting new radionuclides using a statistical deviance test.

  Experimental results on both simulated and measured spectra are presented and compared to the standard OMP algorithm, the proposed Poisson based OMP algorithm presents the following advantages:

  - Comparing to the OMP algorithm that not fully accounts for the Poisson statistics, the Poisson-based OMP algorithm is shown to improve the gamma-ray spectrum analysis while limiting the false identification of radionuclides that not present in the measurement, and reducing the estimation bias of active radionuclides.
  - The proposed deviance-based stopping rule is compared to other information criteria. As a result, the deviance-based stopping rule provides more accurate radionuclides' identification.

  The Poisson-based spectral unmixing approach for gamma-ray spectrum analysis is thoroughly investigated in Chapter 3 and 4. The main focus of the second part of the thesis is the metrological use of the proposed algorithms. The aim is to provide accurate quantitative analysis of gamma-ray spectra measurements that cope with standards of the radioactivity measurements.

- In Chapter 5, we present the assessment of two characteristic limits: the decision threshold and the limits of the confidence intervals. These characteristic limits are related to statistical limits for decision making purposes in experimental data analysis.

  The chapter starts with the definitions of the characteristic limits, where we present how these limits are related to the statistical hypothesis framework. Next, we discuss the quantification of the exact characteristic limits with Monte Carlo simulations, which can not be used in practice due to the massive computation. Therefore, we propose alternative approaches and compare the results to those carried out with the Monte Carlo simulations.

  - The decision threshold of the Poisson-based spectral unmixing algorithm is firstly investigated, we propose a statistical test-based approach that enables accounting for the full spectrum information.
  - Next, we explored the use of Fisher information matrix to derive the confidence intervals of the results.

  The above methods are evaluated with realistic data of the routine measurements, which confirms the validation of the procedures to analyze experimental data performed in the laboratory.

- In Chapter 6, we focus on the quantitative analysis of a gamma-ray spectrum, which depends on not only the spectrum analysis algorithm, but also the proper calibrations of the instrument. As the standard calibration procedures in standard peak-based analysis can not be used in the spectral unmixing analysis, we propose novel calibration methods that adapt to the full spectrum analysis.

  The main calibration steps include the energy calibration, the resolution calibration, and the efficiency calibration. The evaluation of these calibration steps with a standard gamma source (*i.e.*, with known activities) allows validating a pipeline to analyze gamma-ray spectra of routine aerosol filter measurements performed with the same detection system.

  Finally, the calibrated detection system is applied to analyze experimental data. The results show a significant improvement of the sensitivity to detect low-level artificial radionuclides.

CHAPTER 2

Context of the radioactivity measurements with gamma-ray spectrometry

Contents

2.1 Environment radioactivity measurements 6

2.1.1 The radioactivity phenomenon 6

2.1.2 Why measuring radioactivity in the environment ? 7

2.1.3 Quantitative analysis with gamma-ray spectrometry 8

2.1.4 Gamma-ray spectrometry measurements in the laboratory 11

2.2 Description of gamma-ray spectra 12

2.2.1 Detectors and data acquisition 12

2.2.2 Photon interactions with matter 13

2.2.3 Gamma-ray spectrum contributions 15

2.3 Improvement of the detection limits with gamma-ray spectrometry 16

2.4 State of the art of gamma-ray spectrum analysis 17

2.4.1 Peak-based gamma-ray spectrum analysis 17

2.4.2 Full spectrum analysis 19

2.4.3 Machine learning algorithm in gamma-ray spectrum analysis 20

2.4.4 Conclusion 20

In this chapter, we introduce the basics of the gamma-ray spectrometry and its application to radioactivity measurements. In Section 2.1, we present the radioactivity measurements, as well as the quantitative analysis of radioactivity. At the end of the section, we present the gamma-ray spectrometry measurements in the laboratory and the procedure of typical aerosol measurements investigated in this thesis. In Section 2.2, we present the instrumentation of the gamma-ray spectrometry, where we firstly present the detection principle of different detectors and their data acquisition system. Next, we focus on the detection mechanisms, how photons transfer energy to electrons, and the major features of a photon spectrum, which enables us to understand the contributions of a gamma-ray spectrum. Section 2.3 provides the studies to improve the detection limits with gamma-ray spectrometry. The chapter ends up with the state of the art of the gamma-ray spectrum analysis in Section 2.4.

2.1 Environment radioactivity measurements

2.1.1 The radioactivity phenomenon

The radioactivity is the phenomenon in which a nucleus, unstable due to an excess of protons and/or neutrons, disintegrates into another nucleus. We begin with some basic nuclear notations:

- A chemical element is determined by its number of electrons Z (*i.e.*, atomic number) related to its name and its chemical symbol. *e.g.*, the chemical symbol "C" for carbon that has an atomic number of $Z = 6$. The elements and their corresponding symbols can be found in the periodic table of elements, which is a tabular display of the chemical elements arranged by atomic number (see Appendix A).

- A nuclide is characterized by the number of protons (equal to the number of electrons Z), the number of neutrons (N) and the energy state of the nucleus. It is noted as ${}^{A}_{Z}\mathrm{X}$, where X is the chemical symbol, Z is the number of protons, and $A = Z + N$ is the mass number. *e.g.*, ${}^{12}_{6}\mathrm{C}$ with 6 protons and 6 neutrons, usually simply noted with its mass number ${}^{12}\mathrm{C}$.

- Isotopes of a given element have the same number of protons but different numbers of neutrons. For instance, the nuclides ${}^{12}\mathrm{C}$, ${}^{13}\mathrm{C}$ and ${}^{14}\mathrm{C}$ are isotopes of carbon. ${}^{12}\mathrm{C}$ is stable, while ${}^{13}\mathrm{C}$ and ${}^{14}\mathrm{C}$ are unstable isotopes of carbon.

- A radionuclide is an unstable nuclide that has excess of nuclear energy and decays by the emission of nuclear radiation to achieve the stability (*e.g.*, ^{60}Co).

The disintegration of a radionuclide (called "parent") into another nuclide (called "daughter") is accompanied by the emission of alpha radiation or beta radiation. The alpha decay emits an alpha particle identical to $^4_2$He with two protons and two neutrons. The beta decay transforms a neutron into a proton through the emission of an electron (β^-), or transforms a proton into a neutron through the emission of a positron (β^+).

$$\begin{aligned}
\alpha: &\quad {}^A_Z\mathrm{X} \rightarrow {}^{A-4}_{Z-2}\mathrm{Y} + {}^4_2\mathrm{He} \\
\beta^-: &\quad {}^A_Z\mathrm{X} \rightarrow {}^A_{Z+1}\mathrm{Y} + e^- + \overline{\nu} \\
\beta^+: &\quad {}^A_Z\mathrm{X} \rightarrow {}^A_{Z-1}\mathrm{Y} + e^+ + \nu
\end{aligned}$$

The daughter nuclide can be created in its fundamental energy level, but more often in an excited level. The decay is thus followed by the deexcitation of the daughter radionuclide accompanied by the emission of a photon (*i.e.*, electromagnetic radiation) called "gamma-ray". Some other physical phenomena lead to the emission of other photons, called "X -ray". The difference between gamma-ray and X-ray is that they are of different origin, while the gamma-ray originates from the deexcitation of the nucleus and the X-ray originates from the deexcitation of the atom from an excited level to a level of lower energy. The emitted photon energy is equal to the difference between the energies of the initial excited state and the final state.

The photon energy according to the emission of a photon is:

$$E = \frac{hc}{\lambda} \tag{2.1}$$

where h is the Planck constant, c is the speed of light in vacuum, and λ is the wavelength of the photon.

The commonly used unit of photon energy is the electronvolt (eV):

$$1\mathrm{eV} = 1.602176634 \times 10^{-19}\mathrm{J}$$

2.1.2 Why measuring radioactivity in the environment ?

Environment radioactivity measurements, which are performed in worldwide laboratories, play a central role in the field of radiation protection.

Within the French Institute for Radiation Protection and Nuclear Safety (IRSN), the Laboratory of Environment Radioactivity Metrology (LMRE) is in charge of environmental radioactivity measurements for several purposes:

- Monitoring the environmental radioactivity [1] in France to ensure that the activity level in the environment is consistent with regular radioactive releases from industrial and human activities.
- Rapid detection and rapid characterization of sources under emergency conditions, such as increasing radioactivity levels due to an incident or an accident with radioactive releases.
- Radioecology studies for a better understanding of the behavior and transfer mechanisms of the radionuclides in the environment, *e.g.*, modeling the dispersion of radionuclides in the environment can help us to predict the atmospheric dispersion of artificial radionuclides in case of incident or accident. The transfer model of radionuclides in the environment can also be used to assess the human health effects resulting from the radioactive contamination in the environment.

For instance, the monitoring of activity concentration of ^{137}Cs (Half-life = 30.17 years) in the air measured in the environment in France is shown in Figure 2.1. It is an artificial radionuclide resulting mainly from post-atmospheric nuclear weapon tests and the Chernobyl accident.

Measuring radioactivity in the environment requires tackling the quantification of the radionuclides' activity in environmental samples, *e.g.*, aerosols, sediments, biological samples (fauna and flora), etc. It is a challenging problem since a given radionuclide can occur more than one mode of decay and more than one radionuclide can be present in the sample to be measured. Next, we will present the quantitative analysis of gamma-ray emitting radionuclides.

2.1.3 Quantitative analysis with gamma-ray spectrometry

Modeling radioactivity measurements first necessitates accounting for the time evolution of the radioactivity phenomenon. The radioactive decay process can be described by:

$$\frac{dN}{dt} = -\lambda N \tag{2.2}$$

where N is the number of radioactive nuclei, λ (s^{-1}) is the decay constant that is specific for each radionuclide.

[1] `https://www.mesure-radioactivite.fr`

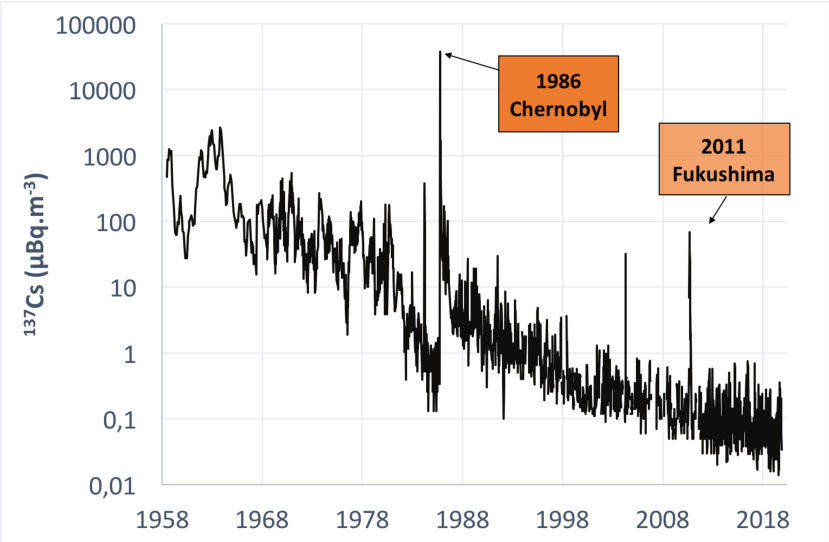

Figure 2.1 – Activity concentration of ^{137}Cs in the air measured in France (1958-2018).

The activity (A) of a radionuclide at a given time is defined as the number of disintegrations per unit time:

$$A = \lambda N \tag{2.3}$$

where the unit of activity (A) is becquerel, 1 becquerel (Bq) = 1 disintegration per second. The well-known exponential decay equation is the solution of Eq.(2.2):

$$N(t) = N(0)e^{-\lambda t} \tag{2.4}$$

It describes the number of remaining nuclei at time t and also holds for the activity:

$$A(t) = A(0)e^{-\lambda t} = A(0)e^{-\frac{ln(2)}{T_{1/2}}.t} \tag{2.5}$$

while $T_{1/2}$ is the half-life of the radionuclide, *e.g.*, 2.7 years for ^{60}Co, 53 days for ^{7}Be, 26.9 min for ^{214}Pb (the half-life of radionuclides mentioned in this thesis can be found in Appendix A).

Many techniques are involved in the radioactivity measurement, such as alpha spectrometry, liquid scintillation and mass spectrometry. Gamma-ray spectrometry is a widely used technique to measure gamma-ray emitting radionuclides' activities, which allows performing direct, non-destructive, and multi-elementary measurements.

The gamma-ray spectrometry determines the activities of radionuclides by measuring the number of emitted photons. More precisely, the number of

emitted photons of different energies is directly related to the radionuclide's activity by their emission probabilities, also called intensities. The emission probability of a photon energy is defined as the number of emitted photons of this energy per 100 disintegrations.

The decay process of each radionuclide is summarized by its decay scheme, which contains its "daughter nuclide" and the α or β decay, as well as the gamma-ray emissions. Taking the example of ^{60}Co for which the simplified decay scheme is shown in Figure 2.2.[1].

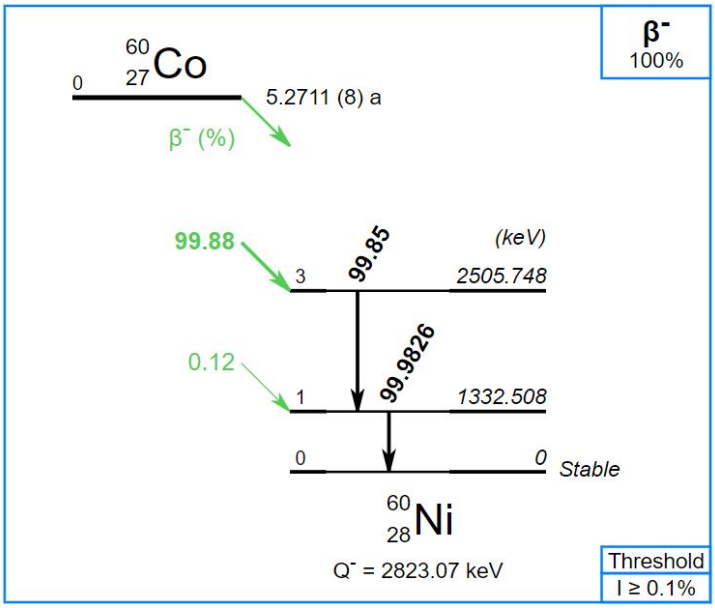

Figure 2.2 – Simplified decay scheme of ^{60}Co.

The ^{60}Co disintegrates by β^{-1} emission to excited levels of ^{60}Ni, mainly to the 2505.7 keV energy level (99.88 % of the disintegrations of ^{60}Co). As illustrated in the decay scheme, this decay is mainly accompanied by the emission of two photons with their according intensities:

- Photon of 1173 keV due to the deexcitation of the daughter nuclide ^{60}Ni from its excited level at 2505.7 keV to another level at 1332.5 keV, intensity = 99.85 %.

- Photon of 1332.5 keV due to the deexcitation of ^{60}Ni from the excited level 1332.5 keV to its fundamental level, intensity = 99.9826 %.

[1] `http://www.nucleide.org/Laraweb/index.php`

In general, for a given radionuclide, the number of emitted photons per second of an energy level, noted N, with its according intensity, noted I, enables calculating the activity of the radionuclide:

$$\text{Activity (Bq)} = \frac{N(\text{number of emitted photons of energy E}/s)}{I(\text{intensity of energy E})} \tag{2.6}$$

In this context, measuring an energy spectrum of a gamma-emitting source allows the identification and the quantification of radionuclides. For instance, the detection of gamma rays of 1173 keV and 1332.5 keV in such an energy spectrum reveals the presence of ^{60}Co in the sample, and the number of photons (1173 keV and 1332.5 keV) observed in the spectrum related to the number of emitted photons by the detection efficiency, provides the activity of ^{60}Co in becquerel (Bq).

2.1.4 Gamma-ray spectrometry measurements in the laboratory

In the framework of radioactivity measurements, different environmental samples are measured in IRSN/LMRE. The samples of different origins, such as waters, aerosol filters, mineral samples (soils, sediments), and biological samples (fauna and flora) are collected, prepared (*e.g.*, dried, freeze-dried, evaporated, calcined, ground, sieved, homogenized) and packed into cylindrical polyethylene containers. Next, we measure the activities of radionuclides in a sample (*i.e.*, gamma-ray and X-ray source), which are:

- Naturally occurring radionuclides including cosmic ray induced radionuclides (*e.g.*, ^{7}Be, ^{22}Na) and telluric radiation (*e.g.*, ^{40}K, ^{210}Pb, ^{228}Ac).
- Artificial radionuclides that are:
  - present at trace levels in the environment due to the normal discharges of the nuclear facilities (*e.g.*, ^{129}I, ^{60}Co, ^{110m}Ag), and the global fallout due to the atmospheric nuclear weapon tests and the Chernobyl accident (*e.g.*, ^{137}Cs).
  - potentially released in case of incident or accident (*e.g.*, ^{131}I, ^{134}Cs).

My investigations focused mainly on aerosol filter measurements intending to detect releases due to low-magnitude incident or accident with higher magnitude but farther away. This is particularly interesting as the first contamination vector for a release is the air transfer. The main steps to measure aerosol samples in the laboratory are described in Figure 2.3.

In the analysis of environmental radioactivity using gamma-ray spectrometry, the activity estimation of low-level radionuclides is particularly required

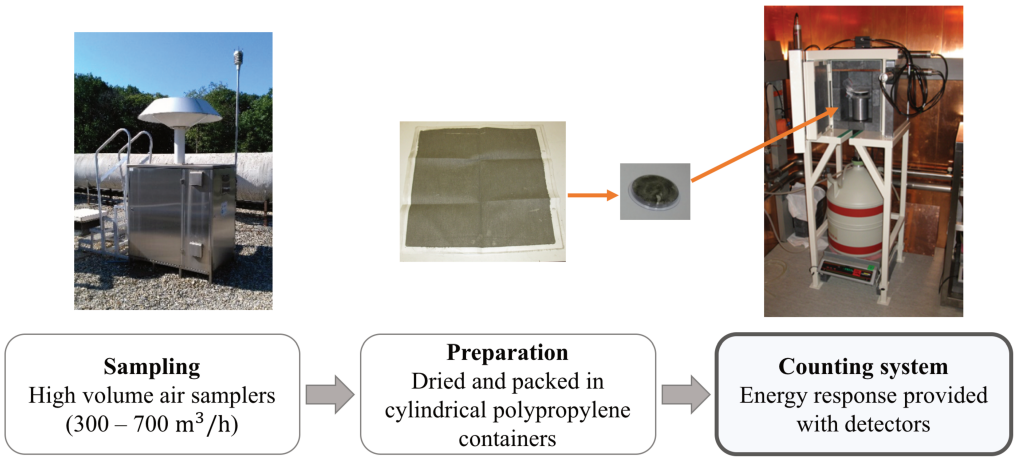

Figure 2.3 – Schema of the aerosol filter measurement.

by the rapid detection and the rapid characterization of sources under emergency conditions. Moreover, the results need to be more accurate and sensitive for the environmental radioactivity monitoring work due to the decreasing levels of artificial radionuclides over the past years. *e.g.*, as shown in Figure 2.1, the activity concentration of ^{137}Cs in the air in France is lower than 1, even 0.1, μBq/m^3. Despite the high sampled volume around 100 000 m^3, the activity to be measured is around a few mBq and the measurement of ^{137}Cs thus requires a long counting time.

2.2 Description of gamma-ray spectra

2.2.1 Detectors and data acquisition

The gamma-ray spectrometry provides the quantitative analysis of radionuclides from an energy spectrum of gamma-rays or X-rays. The measurements can be performed with different types of detectors: semi-conductor detectors *e.g.*, High Purity Germanium detectors (HPGe), and the scintillation detectors *e.g.*, Sodium Iodide (thallium doped) NaI(Tl) or plastic. The detector is the core of a gamma-ray spectrometry system, in which the photons interact with the material of the detector and transfer their energies to electrons. For HPGe detectors, the energy deposited in the detector creates electron-hole pairs in the detector. The electrons are then collected thanks to an applied electric field. A typical gamma-ray spectrometry system is illustrated in Figure 2.4 (see [Knoll, 2010] for details).

The data acquisition starts by transferring the incident photon energy to

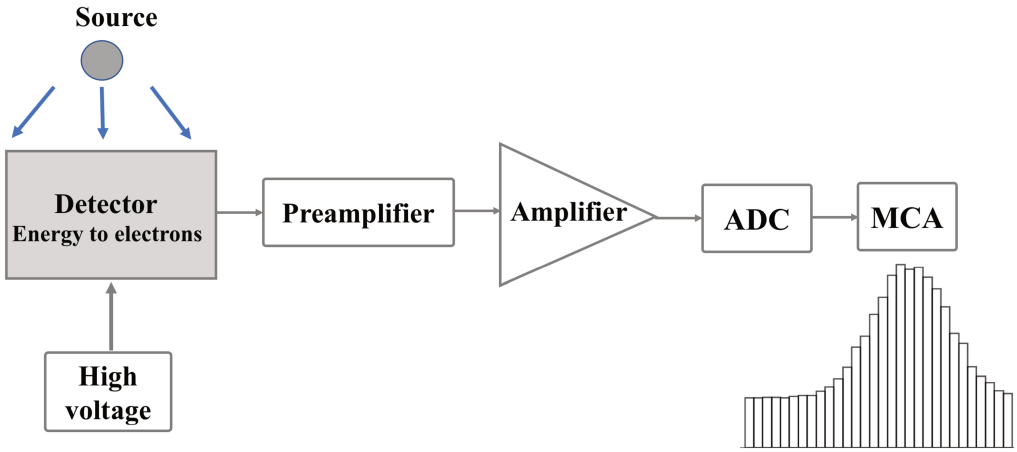

Figure 2.4 – Block diagram of the data acquisition for a gamma-ray detection system.

electrons through the detector material. Next, the electric pulse provided by the detector is amplified and shaped by a preamplifier and an amplifier. While the pulse height is proportional to the deposited energy, the amplifier gain is adjusted to cover the energy range of the photon energies. The signal is subsequently converted by an analog-digital converter (ADC), and finally the multichannel analyzer (MCA) collects pulses and sorts them by pulse height in a fixed number of channels, *e.g.*, 16384 channels covering pulse height from 0 up to 12 Volt. The measured spectrum is therefore the histogram of the number of detected events as a function of the energy that is deposited by the gamma-ray or X-ray in the detector and is called an "energy spectrum". The calibration that relates the channel numbers to deposited energy bins will be investigated in Chapter 6.

2.2.2 Photon interactions with matter

For a better understanding of a gamma-ray spectrum, we briefly describe the main interactions of photons:

- **Photoelectric effect**: the incident photon (gamma-ray or X-ray) disappears by transferring its energy to an electron of the matter.
- **Compton scattering**: the incident photon scatters on an electron by transferring part of its energy to this electron. The energy of the scattered photon is equal to the difference between the initial energy and the energy of the scattered electron, and depends on the scattering angle.

- **Pair production**: if the photon energy is higher than 1022 keV (*i.e.*, twice the mass energy of the electron 511 keV), the incident photon disappears by creating an electron-positron pair. The electron transfers its whole energy to the matter. After losing almost its whole energy by ionization, the positron is annihilated in the contact of a free electron, by emitting two 511 keV photons.

Depending on the probability of the occurrence of the interactions mentioned above, the gamma-ray spectrum of a mono-energetic source can produce spectral features described in Table 2.1. The spectra produced by different photons are shown in Figure 2.5 respectively.

Spectral feature	Energy range	Interaction
Full-energy peak	E_p	Photoelectric effect
Compton continuum	$< E_p$	Compton scattering
Annihilation peak	511 keV	Pair production
Double/single escape peaks	$E_p - 1022keV$ $E_p - 511keV$	Pair production: one or two annihilation gamma-rays escapes from the detector without interaction.

Table 2.1 – Spectral features due to different interactions of gamma-rays or X-rays with matter (energy = E_p).

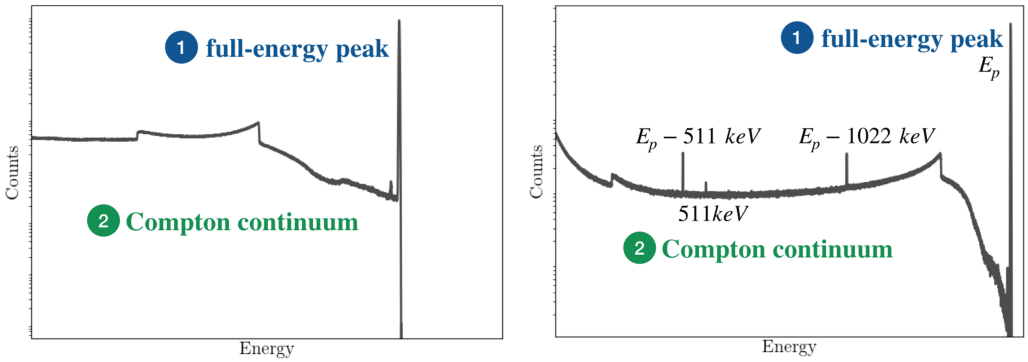

(a) spectrum of photons at $E_p < 1022keV$ (b) spectrum of photons at $E_p > 1022keV$

Figure 2.5 – gamma-ray spectra illustration of monoenergetic source photons.

2.2.3 Gamma-ray spectrum contributions

A measured gamma-ray spectrum can be described as follows:

- As described in Figure 2.5, a photon spectrum is characterized by its energy level (*i.e.*, $E_p < 1022$ keV or $E_p > 1022$ keV).
- A radionuclide can emit photons with different energies depending on its decay scheme thus leading to a spectrum with several peaks and associated continua.
- The measured gamma-ray spectrum of a source containing several radionuclides thus consists of individual spectra of radionuclides.

Meanwhile, a spectrum of the background radiation contributes to the measured spectrum, since gamma-ray emitting radionuclides in the environment can be simultaneously detected. This measure of radiation present in the environment but not originating from the sample is known as "background radiation".

Finally, as illustrated in Figure 2.6, a measured gamma-ray spectrum is the sum of individual spectra of each radionuclide and the background spectrum.

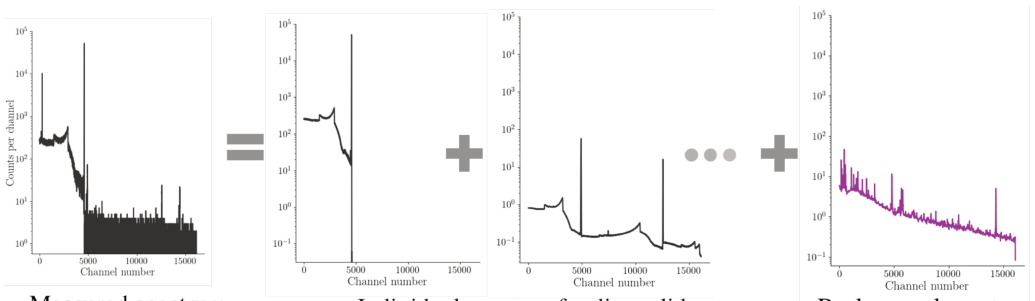

Figure 2.6 – Illustration of gamma-ray spectrum contributions with simulated spectra of HPGe detector.

As a contribution of the measured spectrum, the background spectrum need to be considered in the spectrum analysis. To perform a good estimation of the background spectrum, in the laboratory, the background spectrum is measured every two months for each detector. The radionuclides commonly present in the background are ^{40}K, ^{208}Tl, ^{210}Pb, ^{212}Bi, ^{212}Pb, ^{214}Bi, ^{214}Pb, ^{228}Ac, ^{234}Th, and ^{235}U. Figure 2.7 shows a typical background spectrum measured in the laboratory with some peaks illustrated in colors.

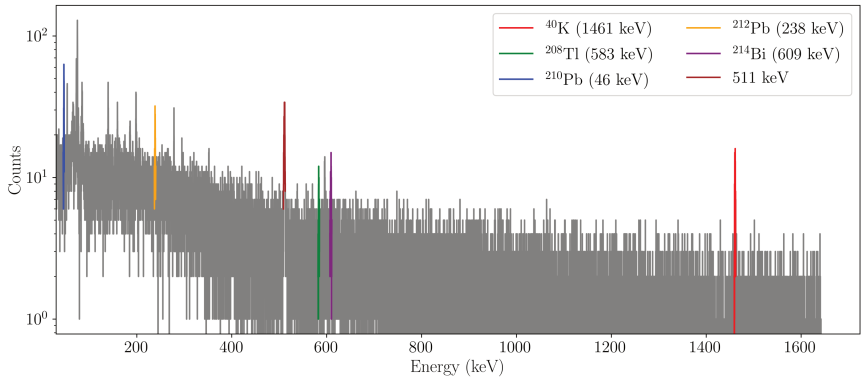

Figure 2.7 – Example of background spectrum measurement.

2.3 Improvement of the detection limits with gamma-ray spectrometry

Involved in the rapid detection of radionuclides, investigations have been carried out in the laboratory to improve the detection limits (*i.e,* the smallest value that can be detected with high reliability):

- On the one hand, developments have been performed in the laboratory with the aim of increasing the signal in the measured spectrum, such as using High volume air samplers to increase the amount of matter to be measured, preparing the samples into small containers (*e.g.*, 10 mL) to increase the detection efficiency (*i.e.,* ratio of the number of detected counts to the number of emitted photons).

- On the other hand, the reduction of the background radiation is an important issue so as to reduce this contribution in the final measured gamma-ray spectrum. As background radiation originates from different sources, different measures for the background radiation reduction are taken into account in the laboratory (see Table 2.2).

While the current detection system provides good performance in the task of low-level gamma-ray spectrum analysis, this thesis aims to develop spectrum analysis tools to improve the accuracy and the sensitivity of the activity determination.

Origin	Solution
Detector	low-background material
Telluric radiation	Shielded room, Individual lead shield
Cosmic radiation	Underground facilities, Anti-cosmic device
Radon	Ventilation system, Gaseous nitrogen flushing

Table 2.2 – Different aspects for background radiation reduction used in LMRE/IRSN.

2.4 State of the art of gamma-ray spectrum analysis

In the previous sections, we introduced the context of gamma-ray spectrum measurements. Thanks to the spectral features of radionuclides characterized by their decay schemes, a measured gamma-ray spectrum allows identifying and quantifying radionuclides. In this section, we review the state of the art of the gamma-ray spectrum analysis methods.

2.4.1 Peak-based gamma-ray spectrum analysis

The peak-based method (*e.g.*, Genie 2000 software from Canberra [1]) is conventionally used in the gamma-ray spectrum analysis, where radionuclides are identified thanks to their characteristic photon energy peaks and quantified from the observed counts in the peaks, which are proportional to the radionuclides' activities. This approach is usually based on Region of Interest (ROI) (see simplified illustration in 2.8 and [Gilmore, 2008] for more details).

In brief, a radionuclide is firstly identified from its characteristic photon energy peaks. Then the method estimates the background counts n_b (*i.e.*, Continua of radionuclides) from the average of two regions (see Figure 2.8) nearby with:

$$n_b = \frac{p}{2b}\left(n_{b1} + n_{b2}\right) \tag{2.7}$$

The net counts n_N can be then calculated from:

$$n_N = n_g - n_b - n_{N0} \tag{2.8}$$

where the gross number in the ROI noted n_g (*i.e.*, the total counts in the ROI), and n_{N0} is the net counts of the background radiation spectrum to be subtracted if the peak is also detected in the background radiation spectrum.

[1] `https://www.mirion.com/products/genie-2000-gamma-analysis-software`

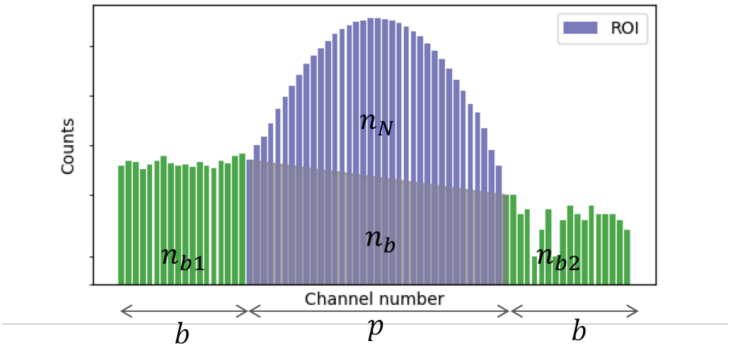

Figure 2.8 – A simple model of the ROI analysis to calculate the net counts n_N in the peak region (purple).

The number of net counts in the peak can be related to the radionuclide's activity with:

$$\text{Activity (Bq)} = \frac{n_N}{\epsilon \times I \times t} \tag{2.9}$$

where ϵ is the detector efficiency (*i.e.*, ratio of the number of detected counts to the number of emitted photons), I is the emission intensity of this photon, and t is the counting time of the measurement.

The peak-based analysis has limited performance. Firstly, the calculation of net counts implicitly assumes that the counting distribution is approximately Gaussian. However, this is not valid at low statistics since radioactive sources emit photons randomly according to a Poisson process. Secondly, a gamma-ray spectrum contains several radionuclides. The interference between individual spectra is difficult to handle with peak-based analysis (*i.e.*, the overlapping of spectra), which can be caused by the following reasons:

- A gamma-ray spectra usually contains several radionuclides that can emit photons of similar energies, which leads to very close peaks or indistinguishable peak sum due to the detector resolution. In this case, the quantification of radionuclides only based on the peak region is not optimal.

- When the peak of a low-level radionuclide is located under the continua of other radionuclides, the noise in the peak region would hamper the estimation accuracy.

- For detectors with poor resolution (*e.g.*, NaI detectors), the limitations in the aforementioned two points are more significant.

The peak-based analysis has been further extended to account for the exact Poisson statistics of the measurements in [Kirkpatrick and Young, 2009]. In this paper, the authors show that the ROI analysis taking into account the Poisson statistics provides improved accuracy comparing to traditional Gaussian methods. However, the analysis only relies on the photon peaks. It is of interest to further account for the entire spectrum that provides more information.

2.4.2 Full spectrum analysis

To overcome the limitation of the gamma-ray spectrum analysis due to the overlapping of individual spectra of radionuclides, the problem can be addressed by the full spectrum analysis. This approach aims at determining the radionuclides' activities by using the observed data in all the energy range of the measured spectrum, including the full energy peaks and the Compton continuum of each radionuclide.

Full spectrum analysis (FSA) has been studied in [Hendriks et al., 2001], [Caciolli et al., 2012], [Jeong et al., 2014] and their references. In these papers, the FSA is applied to analyze different gamma-ray spectra measurements, it addresses the analysis of a spectrum of M channels, $\forall i \in [1, ...M]$, while the linear mixing of individual spectra can be modeled with:

$$y_i = \sum_{j=1}^{N} a_j \phi_j(i) + b_i \tag{2.10}$$

where y_i is the sum of the standard spectra $(\phi_1, ..., \phi_j)$ of radionuclides multiplied by their activity concentrations a_j and the background spectrum b_j in the i^{th} channel, and N is the number of radionuclides.

The gamma-ray spectra detection follows the Poisson distribution:

$$x_i \sim \mathcal{P}oisson\,(y_i) \tag{2.11}$$

where x_i is the counts observed in the i^{th} channel.

The solution of this Poisson regression problem is the least squares weighted by the variance:

$$\min \sum_{i=1}^{M} \frac{(x_i - y_i)^2}{\sigma_i^2} \tag{2.12}$$

while the variance of the Poisson distribution is given by $\sigma_i^2 = y_i$, which is the unknown linear mixing model.

The investigations of FSA make use of the weighted least squares method that determines the activities of radionuclides by minimizing the least squares errors weighted by the observed data (*i.e.*, measured spectrum).

$$\min \sum_{i=1}^{M} \frac{(x_i - y_i)^2}{x_i} \tag{2.13}$$

These studies show that using the full spectrum information provides better counting statistics thus a better estimation accuracy. However, this approach uses the least squares weighted by the measured spectrum is not fully adapted to account for the Poisson statistics of the data, particularly when the mean/ variance value y_i is small.

2.4.3 Machine learning algorithm in gamma-ray spectrum analysis

Other contributions of the activity estimation in the field of machine learning algorithms were also applied to gamma-ray spectral analysis.

In [Yoshida et al., 2002], an artificial neural network (ANN) algorithm is applied to identify radionuclides from gamma-ray spectra by using peak energy data. The performance is however limited when the peaks are overlapped to the Compton continua of other radionuclides.

In [Sharma et al., 2012], authors have presented the application of machine learning to the anomaly detection in gamma-ray spectra. The purpose in this paper is to apply a supervised classification framework to measured gamma-ray spectra by labeling them with normal or certain class of anomaly events.

However, the stated approaches based on neural networks addresses the gamma-ray spectrum analysis problem with measured spectra, which do not allow to precisely account the physical model underlying the detection.

2.4.4 Conclusion

The stated gamma-ray spectrum analysis methods and their limitation can be summarized in Table 2.3.

Method	Limitations
Standard peak-based analysis	inexact Gaussian statistics approximation & interference between individual spectra
Full spectrum analysis based on least squares method	not fully adapted for the Poisson statistics
Machine learning algorithms	Not accounting for the physical model

Table 2.3 – Gamma-ray spectrum analysis methods and their limitations.

These studies reveal that the standard peak-based gamma-ray spectrum analysis can be improved by accounting for the Poisson statistics or the full spectrum analysis. This thesis addresses a more systematic study on the development of alternative spectrum analysis tools, from the mathematical modeling of the gamma-ray detection physics to the metrological aspects for the activity determination in the real data analysis.

CHAPTER 3

Spectral unmixing

Contents

3.1 From statistical modeling to an optimization problem 25

3.2 Spectral unmixing algorithms 27

3.2.1 Least squares unmixing algorithm 27

3.2.2 Poisson statistics-based unmixing algorithms . . . 30

3.3 Experiments on the combination of two radioactive sources 32

3.3.1 Experiments on simulations of HPGe detector . . . 32

3.3.2 Experiments on simulations of NaI detector 33

3.3.3 Results on two radioactive sources mixture 34

3.4 Realistic simulations of routine aerosol samples 35

3.4.1 Convergence rate of algorithms 38

3.4.2 Comparisons of the unmixing algorithms in different counting regimes 41

3.4.3 Evaluation of unmixing algorithms for low-level artificial radionuclide 41

3.5 Experimental results with real spectra from aerosol samples' measurements 44

3.5.1 Dimension of the spectral dictionary 45

3.5.2 Comparisons with peak-based analysis 50

3.6 Discussion 54

From a general perspective, the problem of identifying and estimating the activity of radionuclides from gamma-ray spectra can be tackled as a traditional inverse problem in signal processing. While spectral unmixing is now standard in other fields of research, such as remote sensing [Bioucas-Dias et al., 2012], [Keshava and Mustard, 2002], it has seldom been investigated in gamma-ray data analysis. This chapter first reports on the development of algorithms for spectral unmixing, allowing to carefully account for the underlying mixing model and the statistics of the measure. Next, we apply the spectral unmixing algorithms to gamma-ray spectra and assess their performances to analyze both simulated and experimental data. The contribution of this chapter is as follows:

- The problem of estimating radionuclides' activities with spectral unmixing is formulated in section 3.1. The proposed approach tackles the unmixing problem as a regularized linear inverse problem involving Poisson-distributed measurements.

- Section 3.2 explores the use of unmixing algorithms for activity estimation. To that end, we propose a novel regularized maximum Poisson likelihood estimator. Meanwhile, algorithms based on least squares estimators are also presented for a comparison purpose.

- To evaluate the proposed spectral unmixing approaches, we first investigate the application of spectral unmixing to synthetic data (*i.e.*, simulated gamma-ray spectra).

  - In contrast to standard unmixing problems that involve additive Gaussian noise, the Poisson nature of the measurements' statistics makes the noise highly dependent on the actual mixing. Therefore, the ability to precisely estimate the mixing weight of a given radionuclide will strongly depend on the others' contributions. We evaluate this impact in Section 3.3 with simulated gamma-ray spectra that contain two radioactive sources in both the HPGe detector and NaI detector settings.
  - Next, we focus on realistic data of HPGe gamma-ray measurements in Section 3.4, where simulations with realistic activities of radionuclides are analyzed with the proposed algorithms to assess the ability to analyze real data.

- Experimental results on real spectra are presented in Section 3.5, where the implementation of spectral unmixing algorithms is assessed with sequential data of an aerosol sample measured with HPGe detector.

- Section 3.6 provides conclusions and open problems of this work.

3.1 From statistical modeling to an optimization problem

As we have seen in Chapter 2, a measured gamma-ray spectrum is the sum of individual spectra of radionuclides and the background spectrum. To take into account the full spectral information, we propose to make use of the spectral unmixing, which can be regarded as an inverse problem, where the measured spectrum is composed of M channels:

$$\boldsymbol{x} = [x_1, ...x_M]$$

For $\forall i \in [1, ..., M]$, the Poisson process of radioactive decay leads to model the problem as:

$$x_i \sim \mathcal{P}oisson([\boldsymbol{\Phi a}]_i + b_i) \tag{3.1}$$

The spectral signatures of each radionuclide are denoted by $\boldsymbol{\Phi} = [\boldsymbol{\phi}_1, ...\boldsymbol{\phi}_N]$ and their mixing weights by $\boldsymbol{a} = [a_1, ...a_N]$. The scalar N is the number of radionuclides. $[\boldsymbol{\Phi a}]_i$ is the total number of counts in the i^{th} channel. Similarly, b_i stands for the counts number of background spectrum in the i^{th} channel. The problem is graphically represented in Figure 3.1 in its matrix formulation.

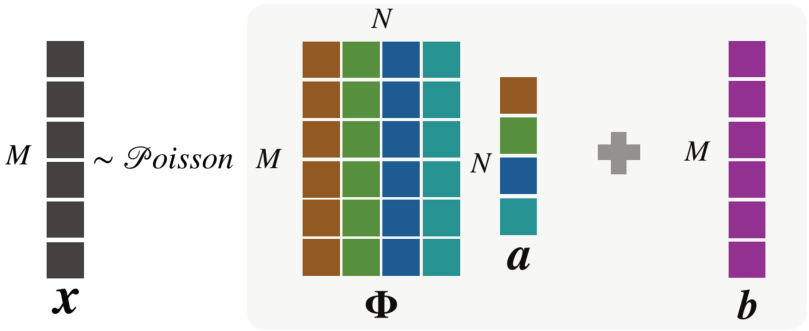

Figure 3.1 – Illustration of spectral unmixing model in matrix form.

Spectral unmixing therefore requires finding the mixing weights $\boldsymbol{a}$. These mixing weights are directly proportional to the activities of radionuclides.

The observed data can be generally written in the form of:

$$\boldsymbol{x} = \boldsymbol{\Phi a} + \boldsymbol{b} + \boldsymbol{n} \tag{3.2}$$

In this chapter, we consider that the spectral signatures $\boldsymbol{\Phi}$ and the background $\boldsymbol{b}$ are known in beforehand. The estimation of the mixing weights $\boldsymbol{a}$ from the measured spectrum $\boldsymbol{x}$ can be addressed by minimizing some distance (*i.e.*, data error associated to noise, noted $\boldsymbol{n}$) between the data $\boldsymbol{x}$ and the model $\boldsymbol{\Phi a} + \boldsymbol{b}$.

The activity estimation can be therefore viewed as an inverse problem that minimizes an objective function, in which the error term $\boldsymbol{n}$ is data dependent in the Poisson statistics model. In such context, to account for the precise Poisson statistics of the spectroscopic measurement, we make use of an estimator that maximizes the likelihood related to the Poisson statistics. In this setting, the probability to observe a given number of counts x_i in the i^{th} channel is given by:

$$\mathcal{P}\left(X_i = x_i \middle| [\boldsymbol{\Phi a}]_i + b_i\right) = \frac{\lambda_i^{x_i} e^{-\lambda_i}}{x_i!} \tag{3.3}$$

where $\lambda_i = [\boldsymbol{\Phi a}]_i + b_i$. Thanks to the statistical independence of the channels, the joint probability or likelihood for the different channels is then given by:

$$\mathcal{P}\left(\boldsymbol{X} = \boldsymbol{x} \middle| \boldsymbol{\Phi a} + \boldsymbol{b}\right) = \prod_i \frac{\lambda_i^{x_i} e^{-\lambda_i}}{x_i!} \tag{3.4}$$

Maximizing the likelihood is then equivalent to minimizing the neg-log-likelihood, which leads to the following Poisson statistics-based activity estimator:

$$\hat{\boldsymbol{a}}_{Poisson} \in \underset{\boldsymbol{a}}{\operatorname{argmin}}\, \boldsymbol{\Phi a} + \boldsymbol{b} - \boldsymbol{x} \odot \log\left(\boldsymbol{\Phi a} + \boldsymbol{b}\right) \tag{3.5}$$

where $\odot$ is the Hadamard product. This optimization problem can be addressed as a generic inverse problem ([Bertero and Bocacci, 1998]) of the form:

$$\hat{\boldsymbol{a}} \in \underset{\boldsymbol{a}}{\operatorname{argmin}}\, f(\boldsymbol{a}) + g(\boldsymbol{a}) \tag{3.6}$$

where the objective function consists of two terms:

- $f(\boldsymbol{a})$: data fidelity term related to the minimization of data error (*e.g.*, $f(\boldsymbol{a}) = \boldsymbol{\Phi a} + \boldsymbol{b} - \boldsymbol{x} \odot (\boldsymbol{\Phi a} + \boldsymbol{b})$ for described Poisson-estimator).
- $g(\boldsymbol{a})$: regularization term, which penalizes the solution of $\boldsymbol{a}$ with some prior information.

More generally, the problem can be formulated as a convex optimization problem of the form:

$$\hat{\boldsymbol{a}} \in \underset{\boldsymbol{a}}{\operatorname{argmin}}\, f(\boldsymbol{a}) + g_1(\boldsymbol{a}) + ... + g_n(\boldsymbol{a}) \tag{3.7}$$

where $g_i(\boldsymbol{a}), \forall i \in [1, ...n]$ for different regularization terms. In the gamma-ray spectrum analysis, we can impose physical constraints in the minimization problem, such as the non-negativity of activities and the number of active radionuclides present in the measurement. The solution of $\boldsymbol{a}$ can also be penalized by data-driven constraints extracted from an archive of measurements, for instance, the interval of radionuclides activities that are commonly present.

3.2 Spectral unmixing algorithms

In the gamma-ray spectrum problem formulation, the mixing weights $\boldsymbol{a}$ is an array with non-negative entries. We firstly focus on overcoming the optimization problem by adding the non-negativity constraint.

$$\hat{\boldsymbol{a}} \in \underset{\boldsymbol{a}}{\operatorname{argmin}}\, f(\boldsymbol{a}) + i_{\cdot \boldsymbol{a} \geq 0} \tag{3.8}$$

where $i_{\cdot \boldsymbol{a} \geq 0}$ is the characteristic function of the convex set (*i.e.* non-negative orthant) $\{\boldsymbol{a} \geq 0\}$. It is precisely defined as follows:

$$i_{\cdot \boldsymbol{a} \geq 0} = \begin{cases} 0, \text{if } \boldsymbol{a} \geq 0 \\ \infty, \text{otherwise} \end{cases} \tag{3.9}$$

3.2.1 Least squares unmixing algorithm

A classical least squares (LS) approach consists in finding the solution $\boldsymbol{a}$ that minimizes the least squares error. In the current unmixing problem, this can be recast as:

$$\hat{\boldsymbol{a}}_{LS} \in \underset{\boldsymbol{a}}{\operatorname{argmin}}\, \frac{1}{2} \|\boldsymbol{\Phi a} + \boldsymbol{b} - \boldsymbol{x}\|^2 + i_{\cdot \boldsymbol{a} \geq 0} \tag{3.10}$$

We tackle this optimization problem with Forward-Backward Splitting (FBS) algorithm ([Combettes and Wajs, 2006]). An accelerated version of the FBS algorithm coined FISTA [Beck and Teboulle, 2009] is used and summarized in Algorithm 1. (Details can be found in Appendix B). In the algorithm:

- the gradient of the data fidelity term $f(\boldsymbol{a}) = \frac{1}{2} \|\boldsymbol{\Phi a} + \boldsymbol{b} - \boldsymbol{x}\|^2$ is:

$$\nabla f(\boldsymbol{a}) = \boldsymbol{\Phi}^T (\boldsymbol{\Phi a} + \boldsymbol{b} - \boldsymbol{x}) \tag{3.11}$$

- the proximal operator of the non-negativity constraint Eq.(3.9) is defined as the orthogonal projection onto the non-negative orthant:

$$\text{prox}_{i._{\boldsymbol{a}\geq 0}} = \begin{cases} 0, \text{if } \boldsymbol{a} < 0 \\ \boldsymbol{a}, \text{otherwise} \end{cases} \tag{3.12}$$

The algorithm is guaranteed to converge when the gradient step $\gamma \leq 1/\|\boldsymbol{\Phi^T\Phi}\|_2$. In practice, the algorithm stops when the relative variation of $\boldsymbol{a}$ between two consecutive iterations is lower than 10^{-12}.

Algorithm 1 Pseudocode of FISTA with constant stepsize

Input:
Fix the step size $0 < \gamma < 1/\|\boldsymbol{\Phi^T\Phi}\|_2$

Initialization:
$\boldsymbol{y}_{(1)} = \boldsymbol{a}_{(0)}$, $t_{(1)} = 1$

while $\frac{\|\boldsymbol{a}_{(k)} - \boldsymbol{a}_{(k-1)}\|}{\|\boldsymbol{a}_{(k-1)}\|} > 10^{-12}$ **do**

$\boldsymbol{a}_{(k)} = \text{prox}_{\ i._{\boldsymbol{a}\geq 0}} \left(\boldsymbol{y}_{(k)} - \gamma \boldsymbol{\Phi}^T(\boldsymbol{\Phi y}_{(k)} + \boldsymbol{b} - \boldsymbol{x})\right)$

$t_{(k+1)} = \frac{1+\sqrt{1+4{t_{(k)}}^2}}{2}$

$\boldsymbol{y}_{(k+1)} = \boldsymbol{a}_{(k)} + \left(\frac{t_{(k)}-1}{t_{(k+1)}}\right)(\boldsymbol{a}_{(k)} - \boldsymbol{a}_{(k-1)})$

end while

From a statistical perspective, the least squares approach is equivalent to a maximum likelihood estimate assuming that the underlying noise is additive, white and Gaussian: $\boldsymbol{n} \sim \mathcal{N}(0, \boldsymbol{\sigma}^2)$. However, because of the Poisson statistics of the spectroscopic measurement, the noise variance is data dependent. It is well known that the variance of the Poisson distribution is equal to the expected value, which leads to $\sigma_i^2 = [\boldsymbol{\Phi a}]_i + b_i$, for $\forall i \in [1, ..., M]$. The weighted least squares (WLS) is indeed the generic form of the least squares, which leads to model the minimization of the WLS error related to the Poisson statistics model with:

$$\hat{\boldsymbol{a}}_{WLS} \in \underset{\boldsymbol{a}}{\text{argmin}} \left(\boldsymbol{\Phi a} + \boldsymbol{b} - \boldsymbol{x}\right)^T \boldsymbol{W}^{-1} \left(\boldsymbol{\Phi a} + \boldsymbol{b} - \boldsymbol{x}\right) + i._{\boldsymbol{a}\geq 0} \tag{3.13}$$

where $\boldsymbol{W}$ is a diagonal matrix with diagonal elements specified by $\boldsymbol{\Phi a}+\boldsymbol{b}$:

$$\boldsymbol{W} = \begin{pmatrix} [\boldsymbol{\Phi a}]_1 + b_1 & & & & \\ & [\boldsymbol{\Phi a}]_2 + b_2 & & & \\ & & . & & \\ & & & . & \\ & & & & [\boldsymbol{\Phi a}]_M + b_M \end{pmatrix}$$

However, the linear mixing model $\boldsymbol{\Phi a} + \boldsymbol{b}$ can not be known in advance. Previous studies (*e.g.*, Full spectrum analysis (FSA) reviewed in Chapter 2) considers $\boldsymbol{W} = \text{diag}\,(\boldsymbol{x})$ (*i.e.*, the measured spectrum), which is not fully adapted to account for the Poisson statistics.

We further propose to tackle this optimization problem with iterative estimation of the true model with an iterative re-weighted least squares algorithm. More precisely, as described in Algorithm 2, the main step of the algorithm consists in estimating the mixing weights, noted $\hat{\boldsymbol{a}}$ and updating the weights with the estimated model: $\boldsymbol{\Phi}\hat{\boldsymbol{a}} + \boldsymbol{b}$.

Each estimation step makes application of the aforementioned FISTA algorithm by considering the gradient of the data fidelity term:

$$\nabla f(\boldsymbol{a}) = \boldsymbol{\Phi}^T \boldsymbol{W}^{-1}(\boldsymbol{\Phi a} + \boldsymbol{b} - \boldsymbol{x}) \tag{3.14}$$

Algorithm 2 Pseudo code of iterative re-weighted squares algorithm

Initialization:
$\boldsymbol{W}_{(0)} = \boldsymbol{\Phi}\hat{\boldsymbol{a}}_{ls} + \boldsymbol{b}$, where $\hat{\boldsymbol{a}}_{ls}$ is the least squares solution.

Estimate the mixing weights $\rightarrow \hat{\boldsymbol{a}}_{(0)}$

for $k < k_{max}$ **do**

Update: $\boldsymbol{W}_{(k+1)} = \boldsymbol{\Phi}\hat{\boldsymbol{a}}_{(k)} + \boldsymbol{b}$
Re-estimation with $\boldsymbol{W}_{(k+1)} \rightarrow \hat{\boldsymbol{a}}_{(k+1)}$
end for

While the iterative re-weighted least squares algorithm allows better accounting for the Poisson statistics, the algorithm still leads to estimation bias of the true model. An approach that takes into account the actual Poisson maximum likelihood estimation is therefore further required.

3.2.2 Poisson statistics-based unmixing algorithms

Along with the non-negativity penalization, the Poisson statistics-based estimator can be formulated as follows:

$$\hat{\boldsymbol{a}}_{Poisson} \in \underset{\boldsymbol{a}}{\operatorname{argmin}}\, \boldsymbol{\Phi a} + \boldsymbol{b} - \boldsymbol{x} \odot \log\left(\boldsymbol{\Phi a} + \boldsymbol{b}\right) + i_{\cdot \boldsymbol{a} \geq 0} \tag{3.15}$$

We now present two algorithms to solve this optimization problem, Multiplicative update algorithm [Lee and Seung, 2001] and the Chambolle-Pock algorithm [Chambolle and Pock, 2011].

Multiplicative update algorithm

The multiplicative update rule with respect to the KL (Kullback-Leibler) divergence loss enables solving the non-negativity regularized Poisson based optimization problem. The multiplicative update algorithm introduced in [Lee and Seung, 2001] is applied to gamma-ray spectral unmixing in [Paradis et al., 2020], which is summarized in Algorithm 3.

Algorithm 3 Pseudo code of spectral unmixing with multiplicative update algorithm

Input:
Measured spectrum: $\boldsymbol{x}$

Spectral signatures: $\boldsymbol{\Phi}$ and Background: $\boldsymbol{b}$

while stopping condition not achieved **do**

Update $\forall j = [1, ..., N]$:

$$a_j^{(k+1)} = a_j^{(k)} \frac{\sum_{i=1}^{M} \Phi_{ij} x_i / M_i^k}{\sum_{i=1}^{M} \Phi_{ij}}$$

with: $\boldsymbol{M}^k = \boldsymbol{\Phi a}^k + \boldsymbol{b}$

end while

This algorithm addresses the non-negativity regularized Poisson estimator. However, the convergence can be slow for low statistic regimes. Moreover, it is less generic due to the difficulty of adding other regularization terms, whereas the proximal algorithms can provide solutions with simplicity. Therefore, we investigate the Primal-dual proximal algorithm for solving the minimization problem in Eq.(3.15).

Primal-dual proximal algorithm

We propose to solve the optimization problem in Eq.(3.15) with primal-dual proximal algorithms such as the one introduced by Chambolle and Pock in [Chambolle and Pock, 2011] (Details can be found in Appendix B). The pseudo-code of the Chambolle-Pock algorithm is given in Algorithm 4, in which the proximal operator of the joint Poisson distribution of the measurement is:

$$\text{prox}_{\rho f}(\boldsymbol{y}) = \frac{\boldsymbol{y} + \boldsymbol{b} - \rho + \sqrt{(\rho - \boldsymbol{y} - \boldsymbol{b})^2 + 4\rho\boldsymbol{x}}}{2} - \boldsymbol{b} \tag{3.16}$$

where $\boldsymbol{x}$ and $\boldsymbol{b}$ stand for the measured spectrum and the background spectrum.

The convergence of the algorithm is ensured with $\sigma\tau < 1/\|\boldsymbol{\Phi}^T\boldsymbol{\Phi}\|_2$ and $\theta = 1$. The step parameters σ and τ are chosen with σ with respect to the total number of counts in the measured spectrum and $\tau = 0.9/(\sigma * \|\boldsymbol{\Phi}^T\boldsymbol{\Phi}\|_2)$ for a better convergence rate. Similarly to the FISTA algorithm, the algorithm stops when the relative variation of $\boldsymbol{a}$ between two consecutive iterations is lower than 10^{-12}.

Algorithm 4 Pseudocode of Chambolle-Pock algorithm

Input:
Fix the parameters: $\sigma, \tau > 0$ and $\sigma\tau < 1/\|\boldsymbol{\Phi}^T\boldsymbol{\Phi}\|_2$.

Initialization:
$\bar{\boldsymbol{a}}_{(0)} = \boldsymbol{a}_{(0)}$, $\boldsymbol{u}_{(0)} = \boldsymbol{\Phi}\boldsymbol{a}_{(0)}$

while $\frac{\|\boldsymbol{a}_{(k)} - \boldsymbol{a}_{(k-1)}\|}{\|\boldsymbol{a}_{(k-1)}\|} > 10^{-12}$ **do**

$\boldsymbol{v} = \boldsymbol{u}_{(k)} + \sigma\boldsymbol{\Phi}\bar{\boldsymbol{a}}_{(k)}$

$\boldsymbol{u}_{(k+1)} = \boldsymbol{v} - \sigma \text{ prox }_{(1/\sigma)f}\left(\frac{\boldsymbol{v}}{\sigma}\right)$

$\boldsymbol{a}_{(k+1)} = \text{prox }_{i_{\boldsymbol{a}\geq 0}}\left(\boldsymbol{a}_{(k)} - \tau\boldsymbol{\Phi}^T\boldsymbol{u}_{(k+1)}\right)$

$\bar{\boldsymbol{a}}_{(k+1)} = \boldsymbol{a}_{(k+1)} + \theta(\boldsymbol{a}_{(k+1)} - \boldsymbol{a}_{(k)})$

end while

3.3 Experiments on the combination of two radioactive sources

To assess the impact of the Compton contribution of a given radionuclide on the determination of another radionuclide, we focus on simulations of simple mixing scenarios that are composed of two sources. The experiments are performed for simulated spectra of HPGe detector and NaI detector, where the spectral signatures used in the simulation process are:

- For HPGe detector, simulations performed with the Monte Carlo N-particle (MCNP) Transport Code, a software package for simulating radiation transport developed by the Los Alamos National Laboratory [Briesmeister, 2000]. We make use of the MCNPX (MCNP eXtended), which simulates the gamma-ray spectrum of sources that emits photons at one or more specific energies with given weights. It provides simulated spectra consisting of given energy peaks and the associated Compton continua.

- For NaI detector, measured spectra with a 3"x3" NaI(Tl) detector without shielding using point sources placed at a distance of 1 m (see details in [Paradis et al., 2020]).

3.3.1 Experiments on simulations of HPGe detector

We consider the mixture of two radioactive sources at 500 keV, noted $\boldsymbol{\phi}_1$, and 200 keV, noted $\boldsymbol{\phi}_2$. The measured spectra are defined as follows:

$$\boldsymbol{x} \sim \mathcal{P}oisson\left(\boldsymbol{\phi}_1 a_1 + \boldsymbol{\phi}_2 a_2 + \boldsymbol{b}\right) \tag{3.17}$$

where $\boldsymbol{\phi_1}$ and $\boldsymbol{\phi_2}$ are simulated with MCNPX, a_1 and a_2 stand for the mixing weights of the sources. $\boldsymbol{b}$ is the spectrum of the background radiation.

As shown in Figure 3.2, we generate simulations as follows: a_1 for the source with energy peak at 500 keV kept fixed and we change a_2 for the one at 200 keV. For each linear combination level, we simulate 100 gamma-ray spectra by random Poisson process as described in Eq.(3.17). Experiments are carried out for these simulated spectra with:

- Poisson unmixing using Chambolle-Pock algorithm. To further highlight how much full spectrum knowledge can help improving unmixing, we further consider two distinct implementations:

  – a full spectrum based version

  - an alternative that only considers region-of-interest (*i.e.*, peak region of the two sources)

- Least squares (LS) spectral unmixing using FISTA algorithm.
- Weighted least squares (WLS) spectral unmixing using Iterative reweighted least squares (the main estimation step uses the FISTA algorithm).

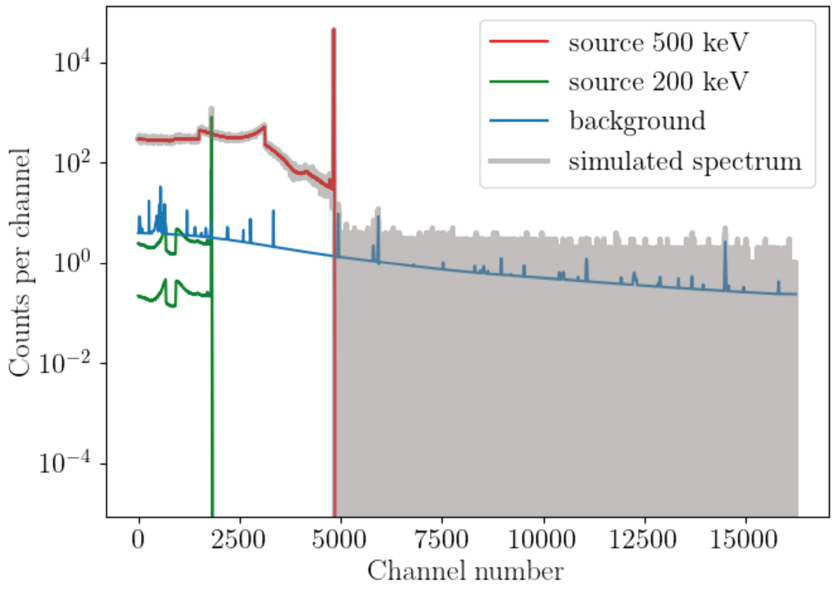

Figure 3.2 – Illustration of HPGe gamma-ray spectra simulation with two energetic radioactive sources. Level of source 500 keV and the background is fixed. Level of source 200 keV changes (green).

3.3.2 Experiments on simulations of NaI detector

As illustrated in Figure 3.2, HPGe detectors provide gamma-ray spectrum measurements with high energy resolution (*i.e.*, peak width). The energy resolution of NaI detectors is much lower than HPGe detectors (spectra illustration can be found in Figure 3.3). The low energy resolution of NaI detector leads to overlapped individual spectra of radionuclides that make the analysis from peaks more difficult. When the spectrum contains very close peaks, the quantification of radionuclides only from the peak is impossible.

Therefore, the full spectrum analysis is extremely demanded for accurate NaI spectra analysis.

Similar experiences of two sources mixing are carried out with NaI detector, where we simulate NaI gamma-ray spectra with the radionuclides ^{57}Co and ^{152}Eu as shown in Figure 3.3. In practice, the analysis of such a spectrum is difficult to handle due to the overlapping of the main energy peak of ^{57}Co and a dominant peak of ^{152}Eu at 122 keV. The spectral signatures are normalized by the total number of counts in the spectrum. Full spectrum unmixing algorithms directly estimate the activities.

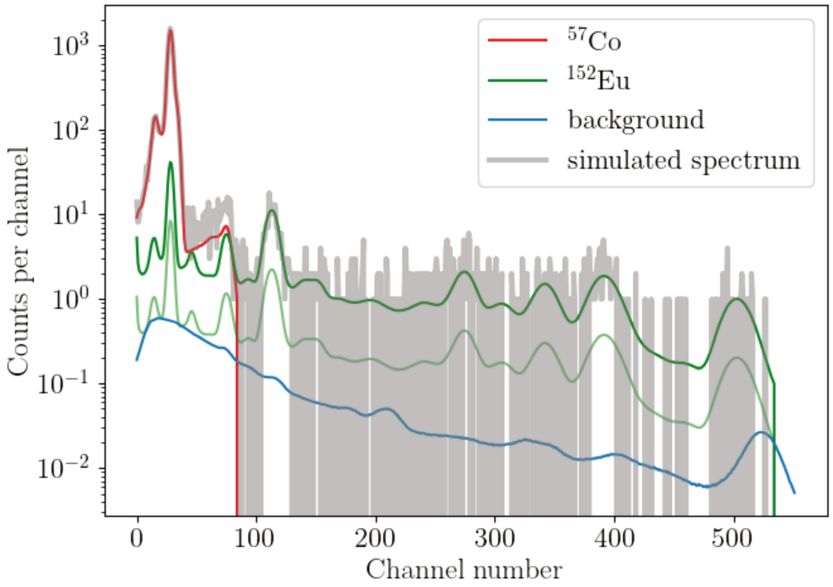

Figure 3.3 – Illustration of NaI gamma-ray spectra simulation with two radionuclides. Level of ^{57}Co and the background is fixed. Level of ^{152}Eu changes (green).

3.3.3 Results on two radioactive sources mixture

From 100 Monte-Carlo simulations, we record the relative error, which is defined as:

$$\frac{\|a - \hat{a}\|}{a} \tag{3.18}$$

where a and $\hat{a}$ stand for the simulated value and the estimated value.

The performances of estimators are compared in Figure 3.4 for experiments of HPGe detector, the first for 200 keV and the second for 500 keV.

The median values and confidence intervals between percentile 25 and percentile 75 are displayed. Similarly, the relative errors obtained with different estimators for experiments of NaI detector are compared in Figure 3.5 for both ^{57}Co and ^{152}Eu.

From these results, we can draw the following conclusions:

- **Advantage of using full spectrum analysis.** As we can see in Figure 3.2, the spectrum of 200 keV is below the Compton continuum of the spectrum of the source of energy 500 keV. The precision of the estimated mixing weight of the 200 keV source is limited, especially when the number of counts is low (see Figure 3.4-a). Nevertheless, the full spectrum analysis using Poisson, LS, WLS estimators provide lower estimation bias than the peak-based analysis.

- **Advantage of Poisson statistics based estimation.** In experiments from both HPGe detector and NaI detector, the Poisson estimator and the WLS estimator provide lower estimation bias and uncertainties, which is shown in Figure 3.4 and Figure 3.5. It should be noted that, in case of mixtures of ^{57}Co and ^{152}Eu, the relative estimation errors for ^{152}Eu is significantly lower for the Poisson estimator and the WLS estimator, as well as the estimation uncertainties. In conclusion, accounting for the Poisson statistics has significant advantages to tackle overlapped spectra of NaI measurements.

- **Poisson estimator and WLS estimator.** The WLS estimator is shown to yield similar estimation bias and error bars than the Poisson estimator. However, the WLS estimator requires iterative estimation of the mixing weights to update the weight matrix. Moreover, the matrix $\boldsymbol{W}^{-1} = \text{diag}\left(\frac{1}{\boldsymbol{\Phi a}+\boldsymbol{b}}\right)$ is usually ill-conditioned, which leads to slow convergence rate. The speeds of convergence will be compared in the next section.

3.4 Realistic simulations of routine aerosol samples

In this work, the spectral signatures are simulated with the MCNP-CP code (A Correlated Particle Radiation Source Extension of a General Purpose Monte Carlo N-Particle Transport) [Berlizov, 2006], which allows simulating physics of nuclear decay and the subsequent emissions.

An example of MCNP-CP simulation for ^{60}Co is shown in Figure 3.6. The MCNP-CP code simulates spectral components due to photon interactions refer to Chapter 2, including two absorption peaks $E_1 = 1173$ keV, $E_2 =$

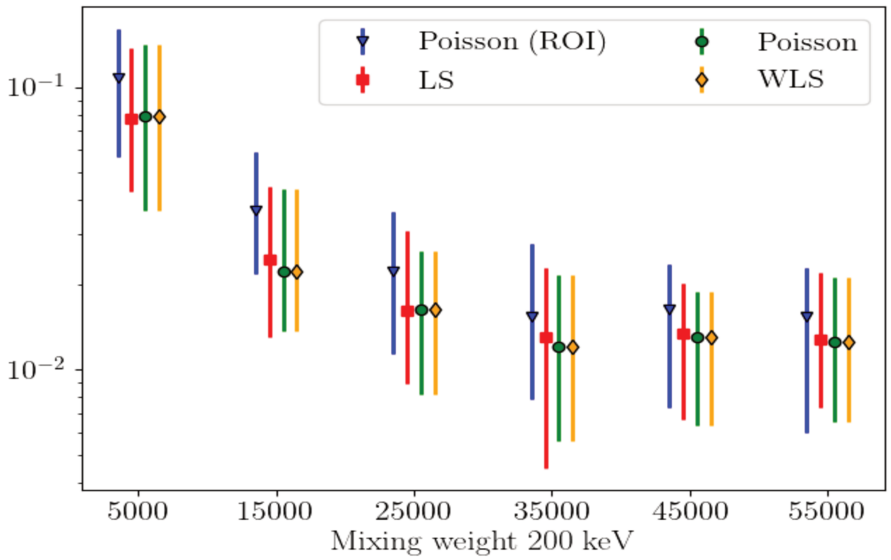

(a) Estimation of source 200 keV

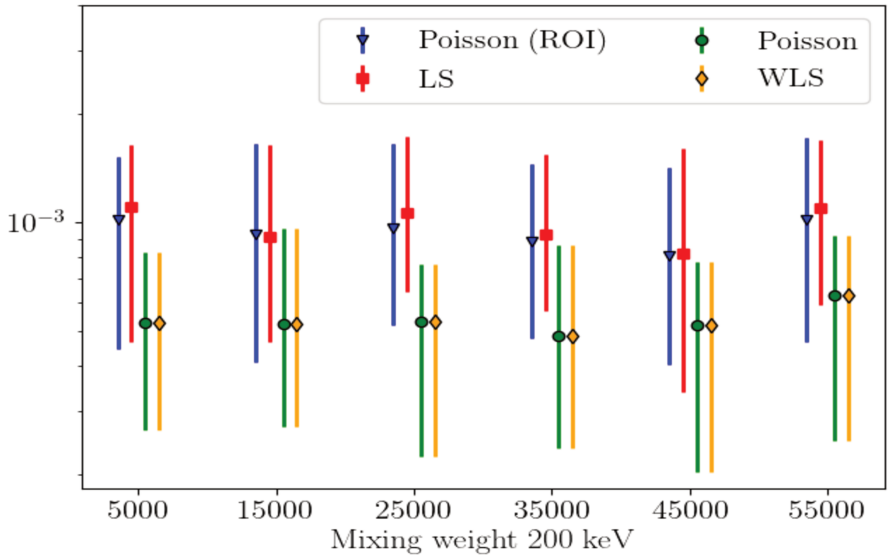

(b) Estimation of source 500 keV

Figure 3.4 – Relative errors comparison for simulated spectra of sources of energy peak of 200 keV and 500 keV (simulations of HPGe detector). The results are display as a function of the mixing weight of source 200 keV.

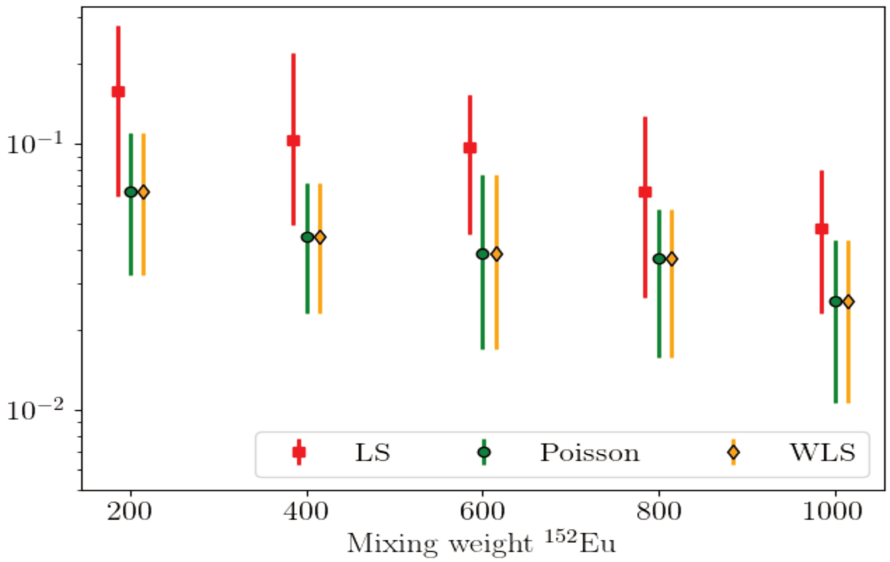

(a) Estimation of ^{152}Eu

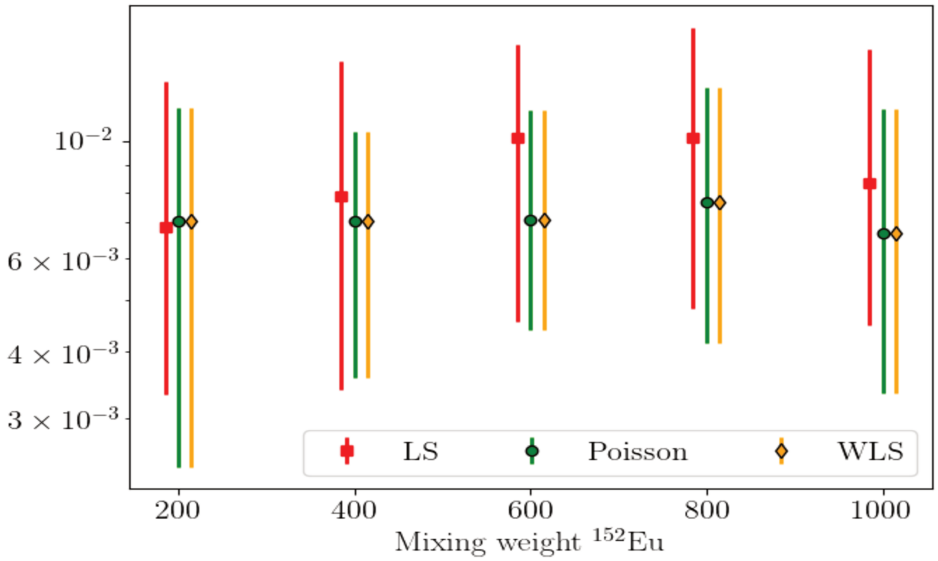

(b) Estimation of ^{57}Co

Figure 3.5 – Relative errors comparison for simulated spectra of ^{57}Co and ^{152}Eu (simulations of NaI detector). The relative errors are presented as a function of the mixing weight of ^{152}Eu.

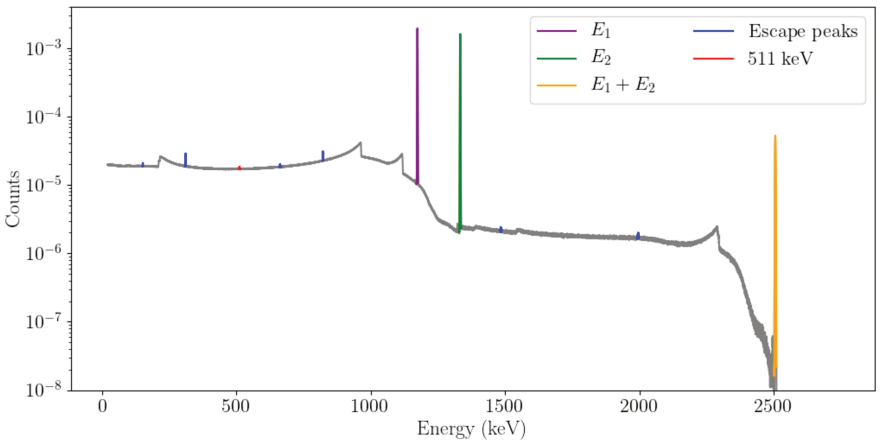

Figure 3.6 – Spectrum of ^{60}Co simulated with MCNP-CP code.

1332 keV, the peak sum at $E1 + E2$. These energies are higher than 1022 keV, escape peaks associated with these energies and the annihilation peak at 511 keV are also simulated. Therefore, the MCNP-CP can be used to simulate spectral signatures of radionuclides when the configurations produce the response of the detection system, while the details about the simulation code can be found in Appendix C.

In the context of gamma-ray measurements with HPGe detector, we investigate a typical routine measurement of aerosol filter samples with 5 radionuclides: ^{7}Be, ^{22}Na, ^{40}K, ^{137}Cs, ^{210}Pb, which are the most commonly found in standard aerosol samples (see Figure 3.7).

3.4.1 Convergence rate of algorithms

The comparisons carried out in Section 3.3 show that, in the counting regimes that we explored, the non-negativity regularized WLS estimator is as efficient as the Poisson-based unmixing algorithm. In this paragraph, we further compare the speed of convergence of the Chambolle-Pock algorithm based on the Poisson estimator and the FISTA algorithm we implemented to compute the WLS estimator. A gamma-ray spectrum is simulated with customarily observed activity for ^{7}Be, ^{22}Na, ^{40}K, ^{137}Cs, ^{210}Pb.

From the simulated spectral signatures denoted by matrix $\mathbf{\Phi}$, and the background spectrum $\boldsymbol{b}$, the spectrum is simulated with random Poisson process:

$$\boldsymbol{x} \sim \mathcal{P}oisson\left(\mathbf{\Phi}\boldsymbol{a}_0 + \boldsymbol{b}\right) \tag{3.19}$$

where the simulated mixing weights can be found in Table 3.1.

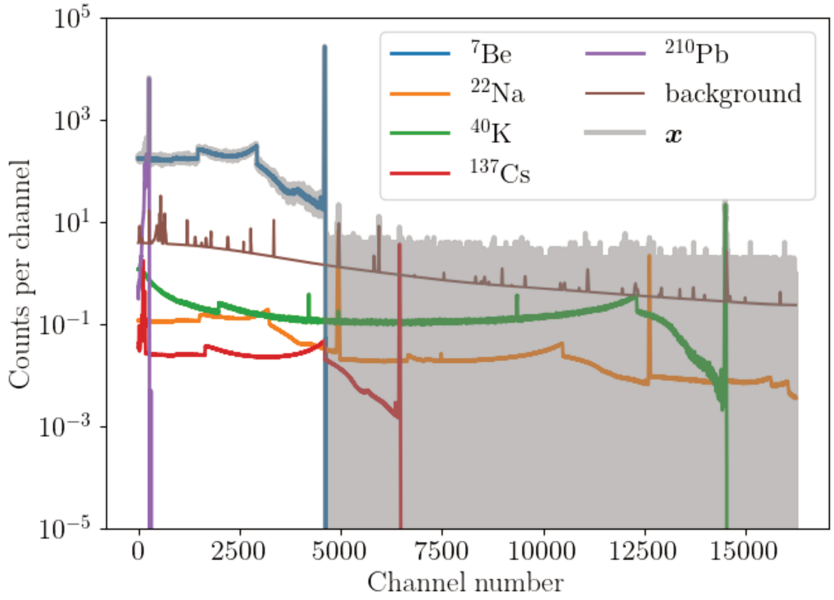

Figure 3.7 – Simulation of gamma-ray spectrum measurements with realistic radionuclides' activities.

Radionuclide	^{7}Be	^{22}Na	^{40}K	^{137}Cs	^{210}Pb
$\boldsymbol{a}_0$	54822748	2332	173715	1370	4999833
$\frac{\boldsymbol{a}_0}{t}$ (*i.e.*, per second)	342	0.014	1.085	0.008	31

Table 3.1 – Simulated mixing weights with $t = 160000s$.

We would like to recall that the WLS estimator derives from a Gaussian approximation of the Poisson likelihood. In this setting, the actual noise covariance matrix is precisely defined as the diagonal of the true mixture model: $\boldsymbol{\Phi a}_0 + \boldsymbol{b}$. For comparison purposes, we make use of the experiments with:

- Poisson-based spectral unmixing.
- weighted least squares with the measured spectrum: $\boldsymbol{x}$ (used in the state-of-the art FSA study).
- weighted least squares with the true, but practically unknown model $\boldsymbol{\Phi a}_0 + \boldsymbol{b}$.

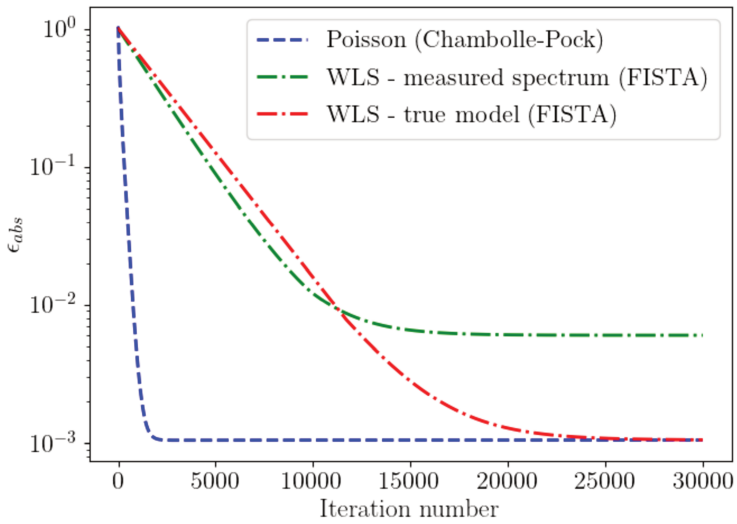

Figure 3.8 – Convergence rate comparison of Chambolle-Pock algorithm (Poisson estimator) and FISTA algorithm (WLS estimator), the absolute errors are displayed versus the iteration number.

Figure 3.8 shows the estimation absolute errors calculated at each iterations of the two algorithms, defined as:

$$\epsilon_{abs} = \frac{\|\hat{\boldsymbol{a}} - \boldsymbol{a}_0\|}{\|\boldsymbol{a}_0\|} \tag{3.20}$$

where $\hat{\boldsymbol{a}}$ is the estimated mixing weights at each iteration.
The comparison confirms that:

- the weighted least squares using measured spectrum is not fully adapted to the Poisson noise, which converges with higher estimation error.
- the convergence to solve such a non-negativity regularized WLS problem by using the true model is slower than that of the Poisson-based estimator (25000 iterations compare to 3000 iterations). It should further be noted that, here we use the actual Poisson variance: $\boldsymbol{\Phi a}_0 + \boldsymbol{b}$. In case that we iteratively estimate $\boldsymbol{\Phi a} + \boldsymbol{b}$ and update the Poisson Poisson variance makes the algorithm slower than the actual version. Moreover, it provides estimation error of $\boldsymbol{a}$ particularly when $\boldsymbol{a}$ is small.

Therefore, we rather use the Poisson-based Chambolle-Pock algorithm in the following experiences.

3.4.2 Comparisons of the unmixing algorithms in different counting regimes

Different statistical regimes are considered so as to simulate different measurement counting times. This is done by introducing a multiplicative factor β by:

$$\boldsymbol{x} \sim \mathcal{P}oisson\left([\boldsymbol{\Phi a}_0 + \boldsymbol{b}] \times \beta\right) \tag{3.21}$$

Experiments are carried out with $\beta = 0.1, 0.16, 0.3, 0.6, 1$, where $\beta = 1$ according to realistic number of counts for which the simulated spectrum is shown in Figure 3.7. We generate 100 simulations for each mixture using the random Poisson process in Eq.(3.21).

The Poisson unmixing is compared to LS unmixing by using the relative estimation error in Figure 3.9. The median values of Monte-Carlo simulations are given. The confidence intervals are defined by the first quartile (25% percentile) and last quartile (75% percentile).

Results

- **Practical advantage for realistic data analysis.** In practice, the role of β is similar to changing the counting time of a measurement. The relative error bars of Figure 3.9 shows that the estimation performances of each algorithm improve when β increases, which confirms the limitation in the low statistics regime. The realistic levels in experimental measurements correspond to mixtures between $\beta = 0.6$ and $\beta = 1$, where the Poisson unmixing algorithm provides more accurate estimation with lower relative errors and lower uncertainties. The method is therefore of special interest to reduce the counting time of the measurements.

- **Impact of Compton continua.** Referring to the spectral contribution shown in Figure 3.7, the results obtained for ^{210}Pb indicate that both estimators have similar performances for estimating a spectrum which consists of dominant peak when the count number is large. The Poisson unmixing has significant advantage for the estimation of ^{22}Na, ^{40}K, ^{137}Cs at low statistics and composed of peaks and significant continuum contributions.

3.4.3 Evaluation of unmixing algorithms for low-level artificial radionuclide

The ability to estimate the low-activity artificial radionuclide plays a central role in the field of rapid detection. In such a context, we focus on

the rapid detection and accurate quantification of ^{137}Cs from aerosol filter

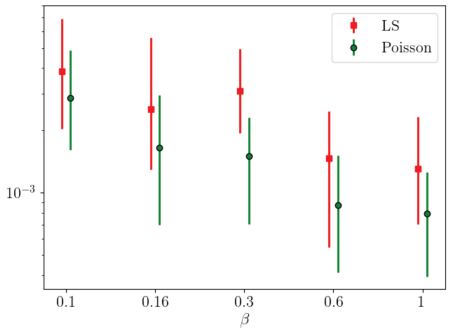

(a) Estimation of ^{7}Be

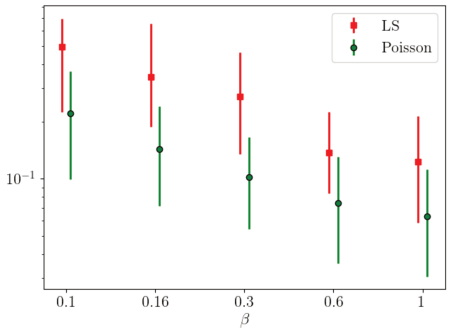

(b) Estimation of ^{22}Na

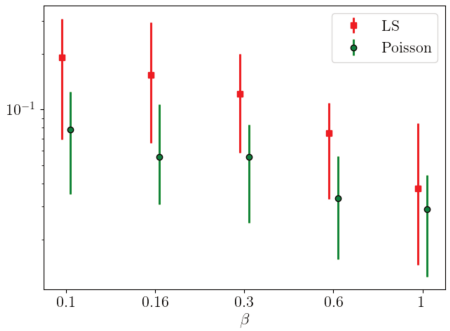

(c) Estimation of ^{40}K

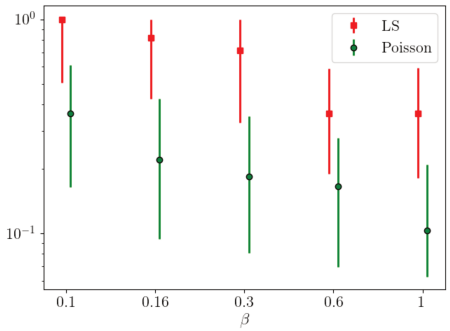

(d) Estimation of ^{137}Cs

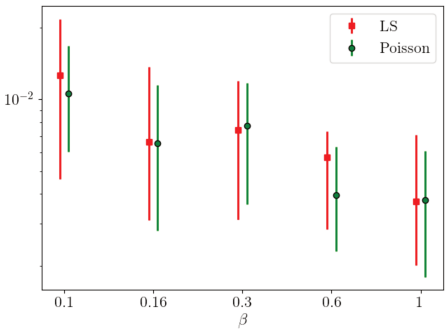

(e) Estimation of ^{210}Pb

Figure 3.9 – Comparison of LS unmixing and Poisson unmixing of realistic simulations. Relative errors for the activity estimates are displayed versus different statistical regimes, where β represents the counting time evolution.

measurements, which is an artificial radionuclide present in the environment in France.

In this experiment, the mixing weights of other radionuclides are fixed relatively to their realistic activities, with respect to $\beta = 1$ in the previous paragraph. Simulations are performed for increasing level of ^{137}Cs. Figure 3.10 compares the estimated mixing weights of ^{137}Cs to their true values.

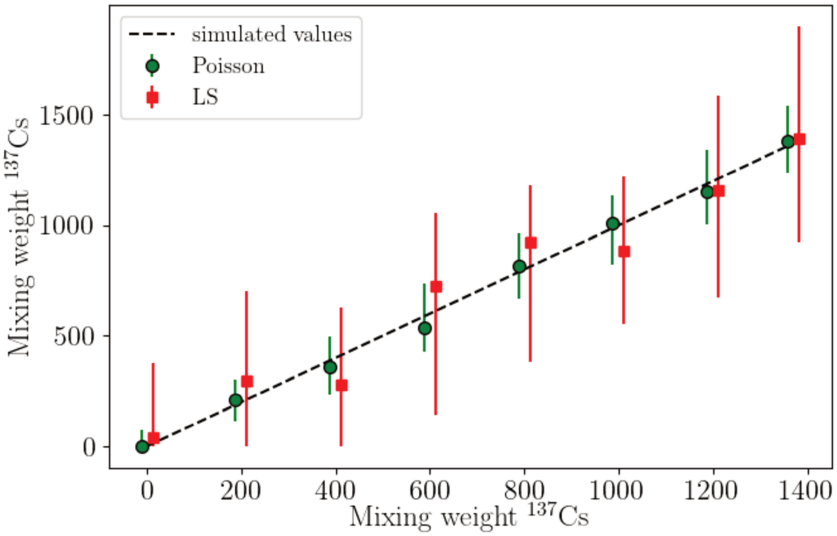

Figure 3.10 – Estimation of ^{137}Cs for the last simulation scenario shown in Figure 3.9 ($\beta = 1$). The simulated mixing weight ranges from 0 to the realistic level.

The results obtained in the realistic setting of routine aerosol measurements demonstrate that the Poisson unmixing improves the estimation quality for ^{137}Cs at low statistics. More precisely, and in comparison with the simulated mixing weight, Poisson unmixing yields closer median values to simulated values with significantly smaller error bars. The results shown in this section with simulated data shows the advantage of Poisson unmixing for low-activity source estimation in environmental samples, which is a difficult problem. Further experiments on real spectra will be performed in the next section.

3.5 Experimental results with real spectra from aerosol samples' measurements

In this section, the proposed approaches are applied to real aerosol samples, which are routinely collected as a part of the surveillance mission of the laboratory. To better focus on the rapid detection of radionuclides, the different unmixing methods are applied to short-time counting statistics. To this end, a dedicated scenario of measurements has been set up for an aerosol sample. These measurements are performed half an hour after the collection, in a continuous manner, with pre-defined counting times for 8 days (see Table 3.2). Figure 3.11 displays the counting rate of these measured spectra as a function of the time after sampling.

		start time	ending time	counting time(s)
s1	19/04 09:10:53	0.5h	1h	1800
s2	19/04 09:41:42	1h	1.5h	1800
s3	19/04 10:12:30	1.5h	2h	1800
s4	19/04 10:44:11	2h	3h	3600
s5	19/04 11:45:03	3h	4h	3600
s6	19/04 12:46:59	4h	5.5h	5400
s7	19/04 14:20:23	5.5h	8.5h	10800
s8	19/04 17:22:17	8.5h	23.5h	54000
s9	20/04 08:41:41	23.5h	1day and 7h	28000
s10	20/04 16:29:59	1day and 7h	4day and 2 h	240000
s11	23/04 11:44:44	4day and 2 h	7day and 19h	320000

Table 3.2 – Measurements of an aerosol filter sampled on 19/04/2018 8:46:00, Orsay, France. The start time and ending time of each measurement are considered from the sampling.

The experiment was carried out with an 10 mL cylindrical counting geometry ($h = 5$mm, $\emptyset = 50$mm) measured with an HPGe detector (60% relative efficiency). The measured spectra are subsequently analyzed with the proposed spectral unmixing algorithms and Genie 2000, which is traditionally used in the laboratory.

In this section, we first investigate how the choice of the spectral signatures impacts the activity estimation quality. This is particularly important as the subset of active radionuclides is generally unknown in practice. Next, the results are compared with the standard peak-based Genie 2000 algorithm.

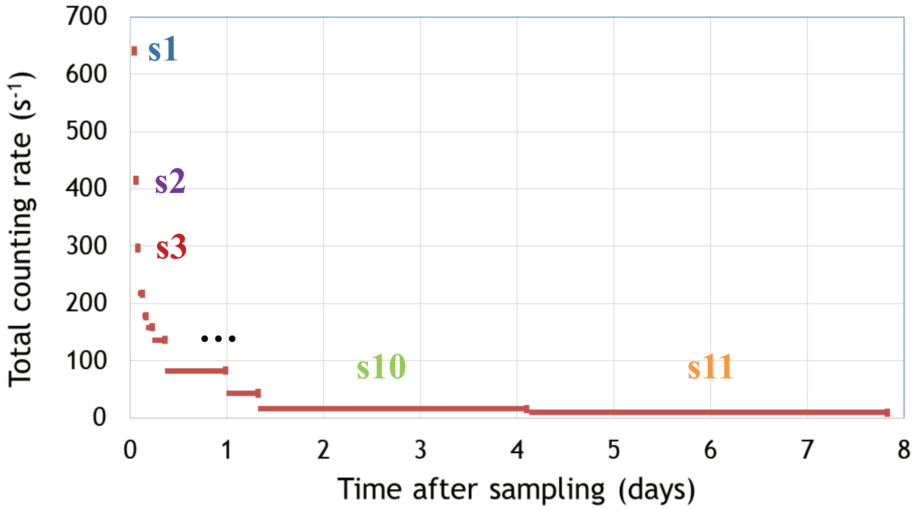

Figure 3.11 – Total counting rate of the successive measurements.

3.5.1 Dimension of the spectral dictionary

The particular choice of the dictionary of spectral signatures is expected to impact the estimation of the mixing weights. In practice, it is well known that several short-lived radionuclides can be detected right after the sampling. These short-lived radionuclides are: ^{208}Tl, ^{212}Bi, ^{212}Pb, ^{214}Bi, ^{214}Pb. They however decay very quickly as time goes on and can be neglected for long enough counting times.

Accordingly, the first measurements are likely to contain significant contributions from short-lived radionuclides than in the last measurements as shown in Figure 3.12. In contrast, the last measurement corresponds to the standard routine aerosol measurement, where most short-lived radionuclides are not detectable. In that case, the predominant peak at 477 keV is characteristic of ^{7}Be, a cosmic-ray induced radionuclide. It gives also rise to the Compton continuum from 165 to 313 keV. Other peaks enable to identify and quantify other natural radionuclides: ^{40}K at 1460 keV or ^{210}Pb at 46 keV. ^{137}Cs and ^{22}Na can also be determined at trace level thanks to their respective peak at 662 keV and 1274 keV. For this kind of measurements, it is therefore customary to only focus on these five radionuclides.

In order to study the impact of the spectral dictionary, we apply the two algorithms with two distinct libraries $\mathbf{\Phi^5}$ and $\mathbf{\Phi^{10}}$, so that the measured spectra are supposed to be decomposed into:

- ^{7}Be, ^{22}Na, ^{40}K, ^{137}Cs, ^{210}Pb, with respect to $\mathbf{\Phi^5} = [\phi_1, ...\phi_5]$.

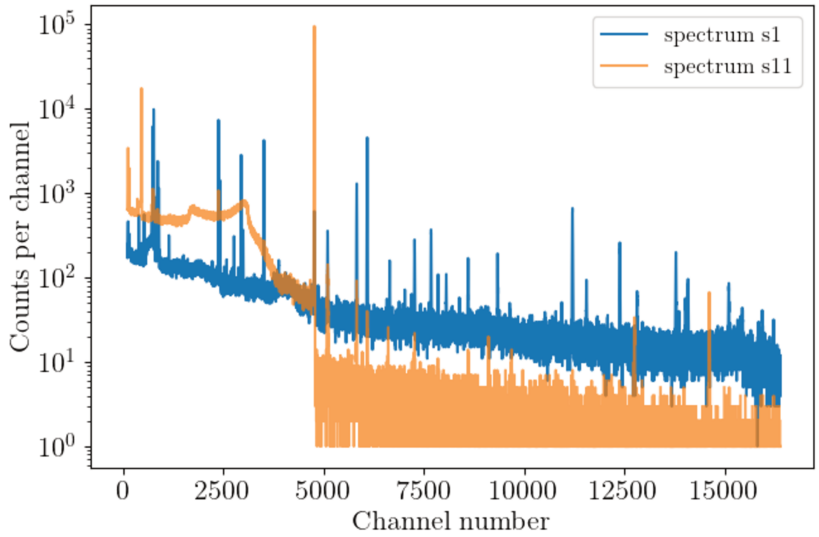

Figure 3.12 – Measured spectra for s1 (measured 30 min after the sampling with counting time = 30 min) and s11 (measured from day 4 with counting time = 4 days). The counting rates in the spectra are : $\approx 640/s$ for s1 and $\approx 9/s$ for s11.

- ^{7}Be, ^{22}Na, ^{40}K, ^{137}Cs, ^{210}Pb, ^{208}Tl, ^{212}Bi, ^{212}Pb, ^{214}Bi, ^{214}Pb, with respect to $\mathbf{\Phi^{10}} = [\phi_1, ...\phi_{10}]$.

Figure 3.13 displays the estimated mixing weights for the 11 measured spectra with both kinds of spectral signatures dictionaries. Comparing both experiments, we get more stable estimated values with the larger dictionary $\mathbf{\Phi^{10}}$. For the last measurement, the results are similar for both $\mathbf{\Phi^{5}}$ and $\mathbf{\Phi^{10}}$, which is expected as only the radionuclides of $\mathbf{\Phi^{5}}$ are likely to be detected.

More specifically, it is well-established for general regression problems in statistics that a badly chosen dictionary of spectral signatures can lead to significantly biased estimation. On the one hand, if the dictionary is too small to precisely describe the content of the data, the results will be biased by the presence of the radionuclides whose spectral signatures are not part of the dictionary. On the other hand, a very large dictionary may be prone to over-fitting, detecting radionuclides that are not present in the data.

To confirm this assumption, a quantitative analysis from simulations is carried out with mixing weights that are similar to those estimated from the 11 measurements. If one assumes that the mixing weights of ^{7}Be, ^{22}Na, ^{40}K, ^{137}Cs, ^{210}Pb are constant, the other natural radionuclides are simulated with realistic decreasing levels.

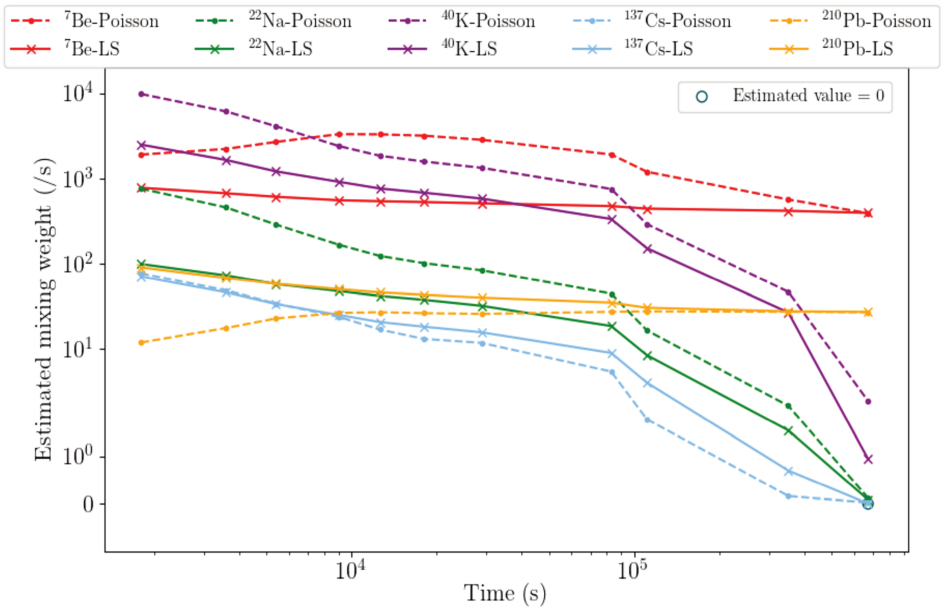

(a) Estimation with $\mathbf{\Phi^5}$

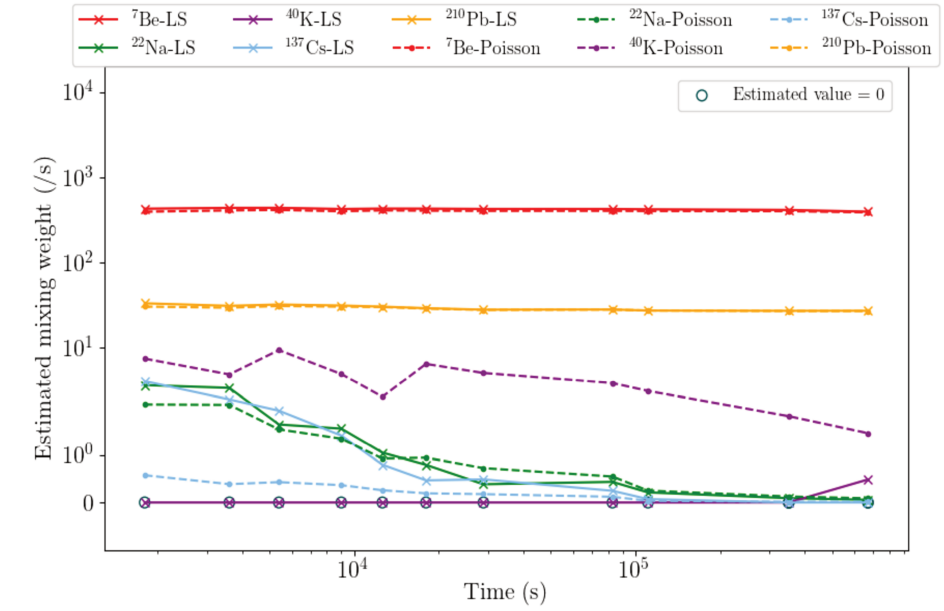

(b) Estimation with $\mathbf{\Phi^{10}}$

Figure 3.13 – The estimated mixing weights versus ending time of the measurements for Poisson unmixing and LS unmixing.

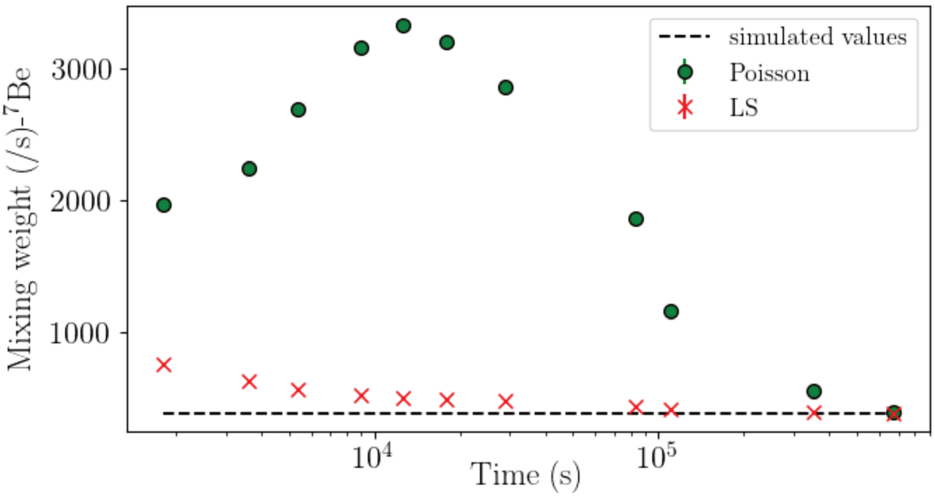

(a) Estimation of ^{7}Be with $\mathbf{\Phi^5}$

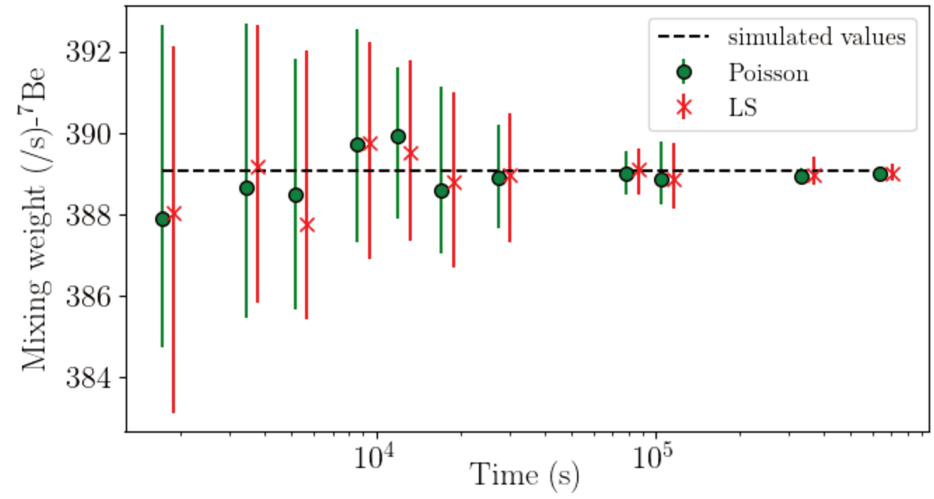

(b) Estimation of ^{7}Be with $\mathbf{\Phi^{10}}$

Figure 3.14 – Results (^{7}Be) on simulations with similar activity levels of the real spectra for $s1 \rightarrow s11$. The first column according to the unmixing with $\mathbf{\Phi^5} = [\phi_1, ...\phi_5]$, the second column according to the unmixing with $\mathbf{\Phi^{10}} = [\phi_1, ...\phi_{10}]$. The estimated mixing weights are compared to simulated values for the 11 spectra.

The results are based on 100 Monte Carlo simulations for s1 $\rightarrow$ s11. Figure 3.14 and Figure 3.15 feature the results for ^{7}Be and ^{137}Cs when either

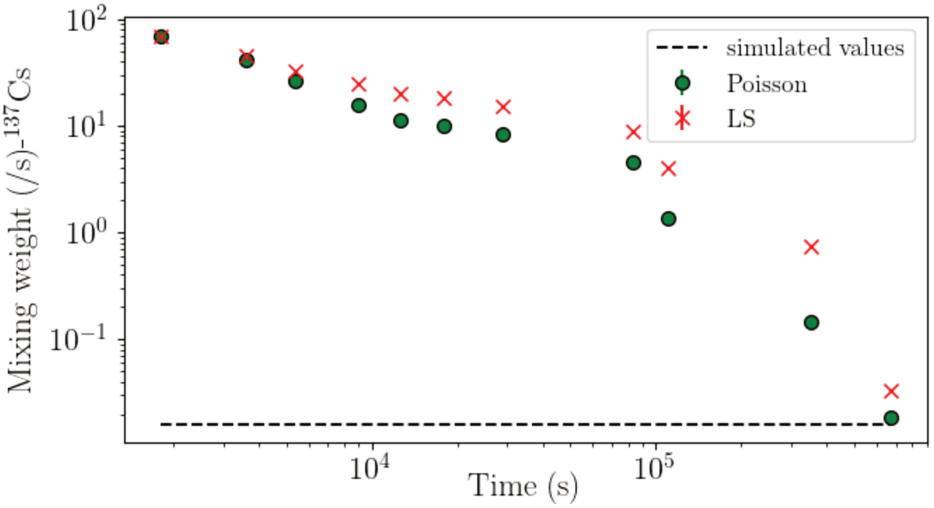

(a) Estimation of ^{137}Cs with $\mathbf{\Phi^5}$

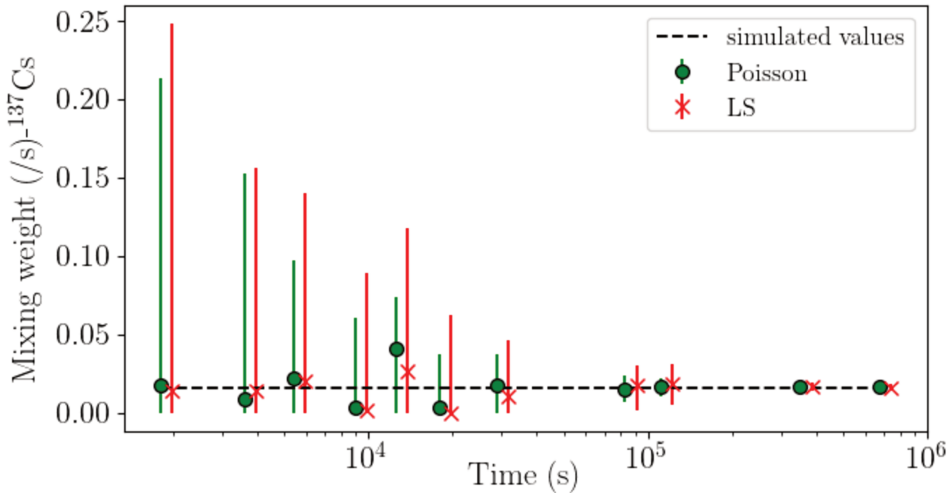

(b) Estimation of ^{137}Cs with $\mathbf{\Phi^{10}}$

Figure 3.15 – Results (^{137}Cs) on simulations with similar activity levels of the real spectra for $s1 \rightarrow s11$. The first column according to the unmixing with $\mathbf{\Phi^5} = [\phi_1, ...\phi_5]$, the second column according to the unmixing with $\mathbf{\Phi^{10}} = [\phi_1, ...\phi_{10}]$. The estimated mixing weights are compared to simulated values for the 11 spectra.

the dictionary $\mathbf{\Phi^5}$ or $\mathbf{\Phi^{10}}$ is used. The error bars display the first and last quartiles.

Moreover, the statistical deviance ([DasGupta, 2008]) is displayed in Figure 3.16, which provides a measure of the goodness-of-fit for both estimators, for either simulated or measured spectra.

More precisely, the statistical deviance for the Poisson distribution is defined by:

$$\mathcal{D} = 2\Big(\boldsymbol{x}\log(\frac{\boldsymbol{x}}{\boldsymbol{\Phi}\hat{\boldsymbol{a}}+\boldsymbol{b}}) - \boldsymbol{x} + \boldsymbol{\Phi}\hat{\boldsymbol{a}} + \boldsymbol{b}\Big)$$

where $\hat{\boldsymbol{a}}$ stands for the estimated mixing weights.

Results

As shown in Figure 3.14-a and Figure 3.15-a, making use of the small dictionary $\boldsymbol{\Phi^5}$ leads to significant biases in the first measurements, where short-lived radionuclides can hardly be neglected. The results obtained with a larger spectral dictionary $\boldsymbol{\Phi^{10}}$ leads to much more accurate results as shown in Figure 3.14-b and Figure 3.15-b. These results are similar to the ones we obtained with real spectra (see Figure 3.13). Poisson unmixing tends to overestimate the activities comparing to the least squares unmixing. One can observe that Poisson unmixing tends to be more sensitive to the choice of the spectral dictionary. The origins of this phenomenon is the Poisson unmixing aims to precisely fit the measured spectrum with the full spectrum, which yields increased errors when the spectral dictionary cannot fit the actual set of radionuclides, since the logarithmic scaling in the likelihood term induces lower weights on channels in peak regions.

Figure 3.16 shows that, in the first measurements, the spectral unmixing with $\boldsymbol{\Phi}^{10}$ provides lower deviance than with $\boldsymbol{\Phi}^5$ for both simulated and measured spectra. In this case, the estimated models with $\boldsymbol{\Phi}^5$ tend to fit for the short-lived radionuclides that are not in the spectral signatures dictionary, with the ones contained in the dictionary. In the last measurement, short-lived radionuclides having significantly decayed, making use of $\boldsymbol{\Phi}^5$ leads to lower deviance since this dictionary already provides an accurate description of the measurements. Moreover, lower deviance is achieved with Poisson unmixing for each experiment, which confirms the advantage of Poisson unmixing to analyze these data, whether they are simulated or real measurements.

The results obtained using different choices of spectral dictionaries highlight that the accurate identification of spectral signatures is of key importance for the spectral unmixing to work efficiently.

3.5.2 Comparisons with peak-based analysis

We compare the results of the Poisson unmixing estimator with those of Genie 2000, which is the workhorse method in a large number of radioactivity

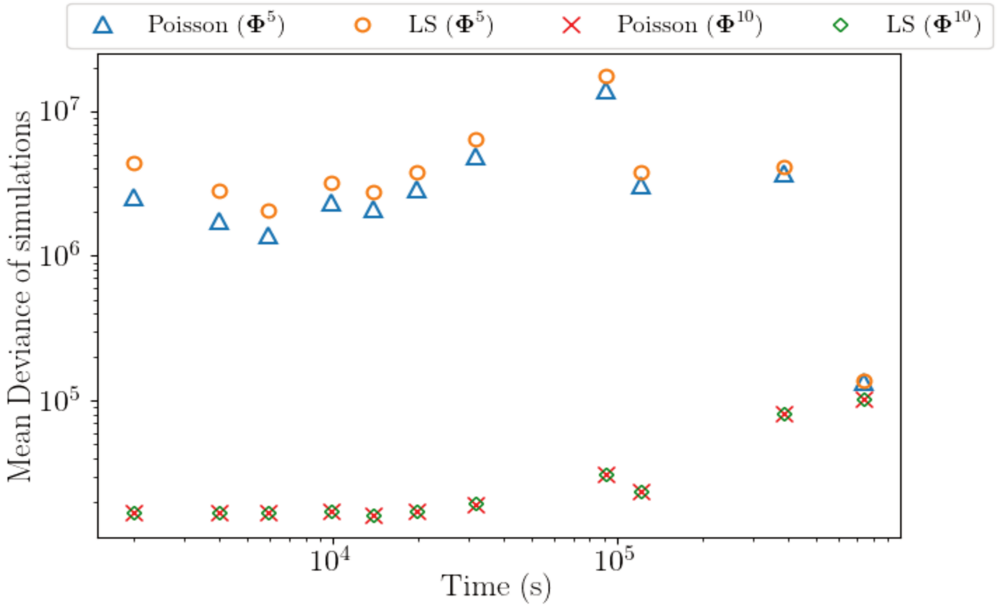

(a) Estimation of 100 Monte Carlo estimations

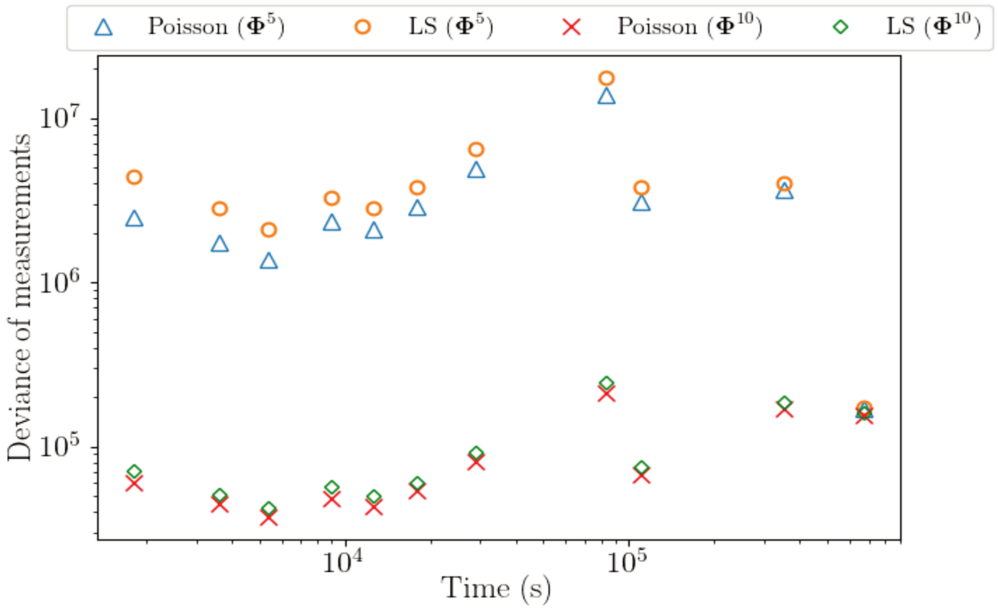

(b) Estimation of measured spectra

Figure 3.16 – Deviance of models estimated by Poisson unmixing and least squares unmixing are compared when $\mathbf{\Phi^5}$ and $\mathbf{\Phi^{10}}$ are chosen, (a), application to simulated spectra and (b), application to measured spectra.

measurement laboratories. As discussed previously, these comparisons have been carried out with the 10-radionuclides dictionary, which is suitable for the analysis of measured spectra. We first focus on the long-lived radionuclide ^{7}Be and the short-lived radionuclide ^{212}Bi. The estimated mixing weights are compared in Figure 3.17. Secondly, the results for ^{137}Cs are displayed in Figure 3.18.

Results

As shown in Figure 3.17, the Poisson unmixing and Genie 2000 algorithms provide similar results for the estimation of ^{7}Be and ^{212}Bi, while the estimated mixing weights are of the same order in the last two measurements. This is related to the larger counting rates obtained with long counting times (3 days for s10 and 4 days for s11).

Figure 3.18 shows that the Poisson unmixing algorithm detects ^{137}Cs with similar level to that obtained with Genie 2000 from the measurement s10, which is evaluated from day 2 to day 4. To validate this result, simulations are performed with the final estimated mixing weights obtained with the Poisson unmixing algorithm ($\hat{a} = 0.016/s$ for ^{137}Cs) to mimic the measurement s10. 1000 Monte Carlo simulations are generated to compute a confidence interval. 1000 extra Monte Carlo simulations are carried out with $^{137}\text{Cs} = 0$ to quantify the false positive rate. In Figure 3.19, the distribution of the estimated mixing weights is presented for both experiments.

These results allow to draw the following conclusions:

- The detection of ^{137}Cs is statistically significant for the significance level of $\alpha = 0.05$ in the null hypothesis.

- The confidence interval derived from the simulations also confirms that the activity level measured from the real measurement s10 is significant.

This confirms that the Poisson unmixing algorithm allows identifing ^{137}Cs four days before the usual method Genie 2000.

In this section, we can first conclude that when full spectrum unmixing is used, the lack of knowledge of the actual active radionuclides may lead to under-fitting or over-fitting effects, which eventually lead to biased activity estimation. Secondly, Poisson unmixing yields significant improvements for the estimation of low-activity radionuclides, which is a key advantage for the rapid detection of an anomaly in the air.

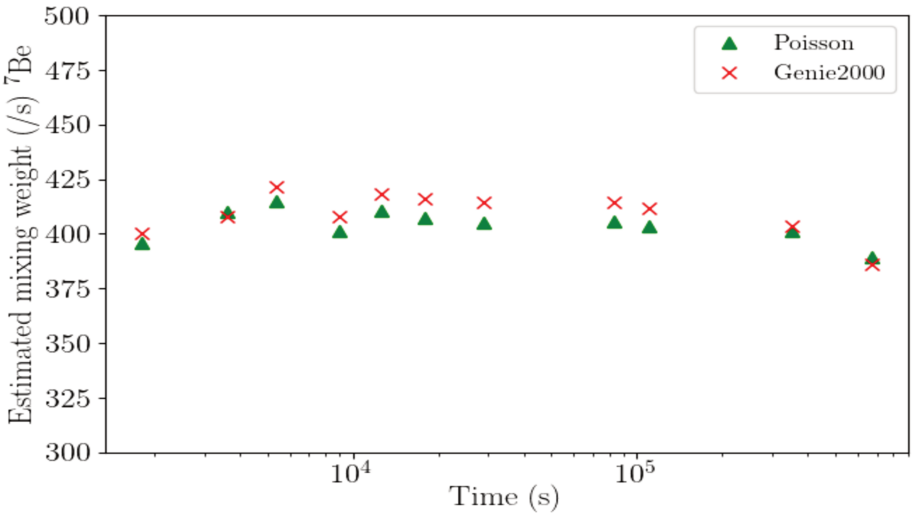

(a) Estimation of ^{7}Be

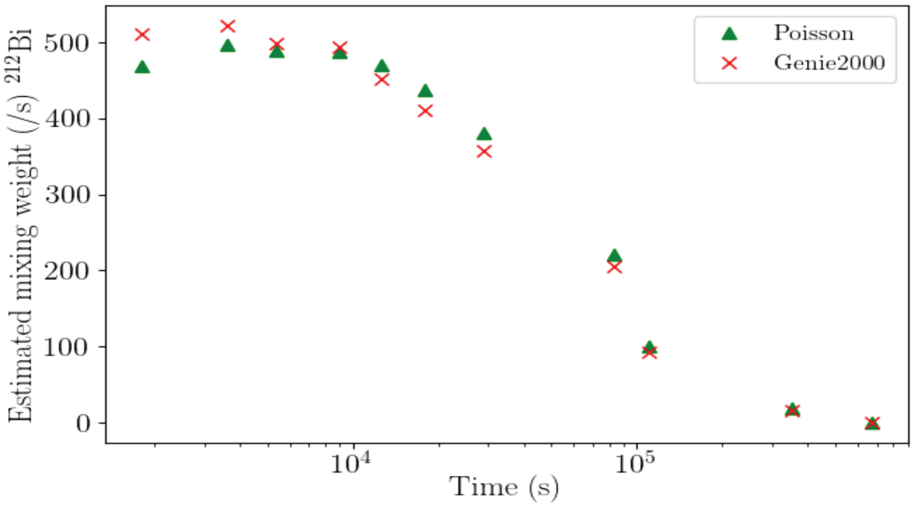

(b) Estimation of ^{212}Bi

Figure 3.17 – Mixing weights estimated with Poisson unmixing (green) and Genie 2000 (red) for ^{7}Be (a) and ^{212}Bi (b), respectively. The results obtained by net peak area analysis of Genie 2000 are converted to mixing weights by $\boldsymbol{a}_i = \frac{{S_{net}}^i}{{S_{net}}^{\phi_i}}$ (${S_{net}}^i$: the measured net area of the i^{th} radionuclide, ${S_{net}}^{\phi_i}$: the net area of the i^{th} spectral signature). The results are plotted as a function of the ending time of each measurement.

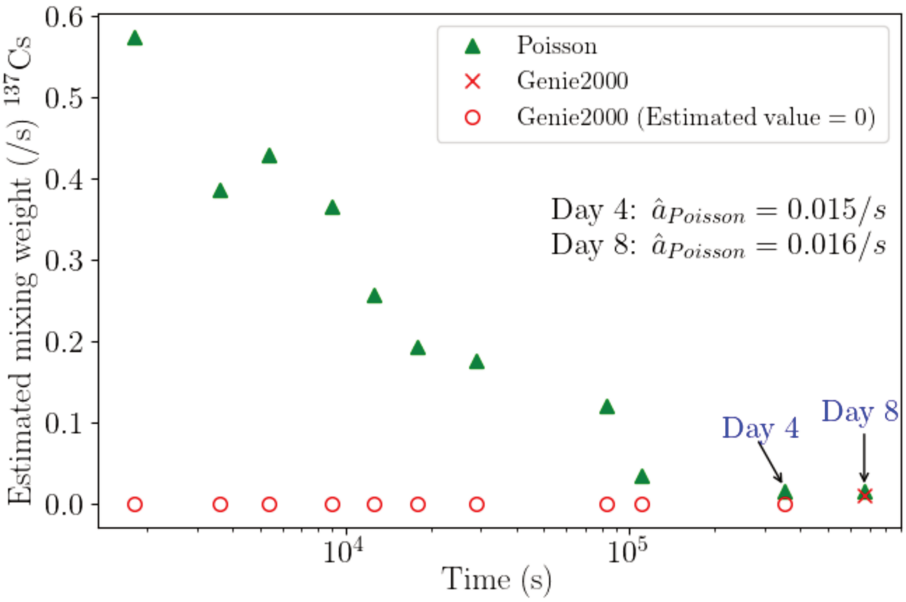

Figure 3.18 – Estimation of ^{137}Cs as presented in Figure 3.17. The results of the last two measurements provided by Poisson unmixing are presented with the ending time of the measurements.

3.6 Discussion

Activity estimation algorithms based on spectral unmixing are presented in this chapter, which exploit the full spectrum of radionuclides. In such a context, the least squares regression approaches and a Poisson unmixing algorithm based on Poisson statistics are proposed to estimate the mixing weights of each radionuclide from the measured spectrum.

Comparisons and quantitative evaluations have been carried out from both simulated and real measurements, which demonstrate that both these full spectrum estimators lead to very precise activity estimations. The Poisson unmixing algorithm, which precisely takes into account the Poisson statistics of the underlying physical process, provides significantly improved results. This is especially true when the counting rate is low.

For the rapid detection of radionuclides from gamma-ray spectra measurements, which requires analyzing environmental samples with low-level activities, the time for detection and identification can be dramatically reduced for artificial radionuclides. While having been thoroughly evaluated in the case of aerosol samples measured with HPGe detectors, the proposed

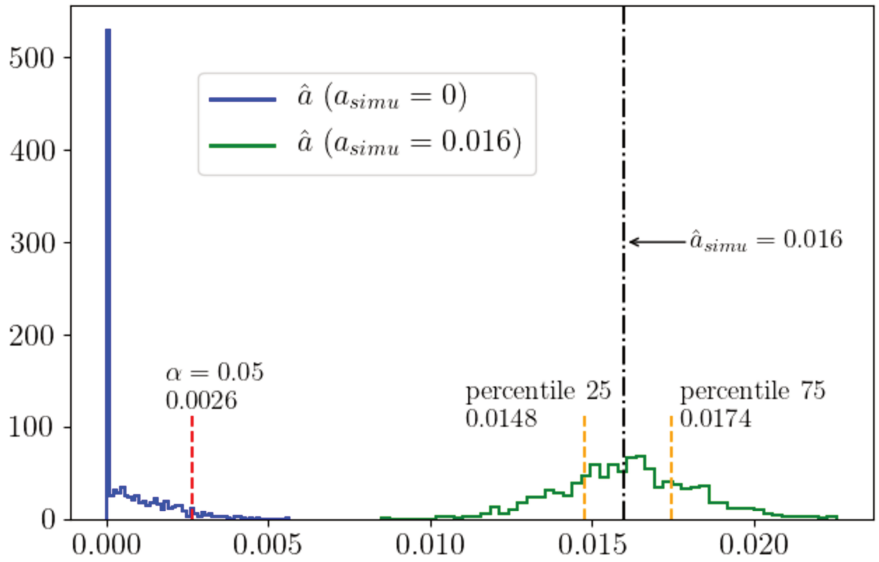

Figure 3.19 – Distribution of estimated mixing weights obtained with: i), $a_{simu} = 0$ (blue) with threshold according to $\alpha = 0.05$ (red); ii) $a_{simu} = 0.016$ (green) with confidence interval between 25% and 75% percentiles (orange).

methods are generic and can be applied virtually to any kind of samples measured with gamma-ray spectra, with any type of detectors. The limitations of the present studies include:

- Estimation bias due to the lack of knowledge of the spectral signatures.
  - It is shown that an inadequate choice of the spectral signatures dictionary can generate biases due to either over or under-fitting effects. To alleviate this problem, the joint estimation of the subset of active radionuclides will be investigated in Chapter 4.
  - For the quantitative analysis of real spectra, the simulated spectral signatures need to be calibrated for instruments used in the measurement, while the different aspects of quantitative calibrations will be carried out in Chapter 6.
- Another limitation of the current method is that we assume that the spectral signatures and the background spectrum are accurately known. It might increase the estimation error and false identification rates of radionuclides. The variability of spectral signatures and the background spectrum will be further discussed in Chapter 7.

CHAPTER 4

Sparse spectral unmixing

Contents

4.1 A model selection approach 58
4.2 Sparse solution 60
4.3 Greedy algorithm to identify active radionuclides 61
4.3.1 Greedy algorithms in least squares problem 61
4.3.2 The Poisson OMP Algorithm 61
4.3.3 Stopping criteria for radionuclides identification . . 62
4.4 Application of $\mathcal{P}$-OMP to HPGe measurements 65
4.4.1 Data description 65
4.4.2 Evaluation on simulated spectra 65
4.4.3 Evaluation on measured spectra 67
4.5 Application of $\mathcal{P}$-OMP to NaI measurements . . 68
4.5.1 Description of the data 68
4.5.2 Application to NaI measurements - scenario I . . . 69
4.5.3 Application to NaI measurements - scenario II . . 72
4.5.4 Application to NaI measurements - scenario III . . 74
4.5.5 Stopping rule, comparing the deviance-based test with information criteria 76
4.6 Summary of the sparse spectral unmixing . . . 77

In Chapter 3, we have seen that the Poisson-based spectral unmixing can provide more sensitive activity estimations in gamma-ray spectrometry.

Meanwhile, the experimental results on successively measured gamma-ray spectra carried out in Chapter 3 show that the spectral unmixing is sensitive to the choice of the spectral signatures dictionary. Using a larger/smaller dictionary can lead to under/over fitting effects that affect the estimation accuracy.

In this chapter, we further investigate how the set of spectral signatures of the actually active radionuclides in a measured gamma-ray spectrum can be identified. In such a context, the spectral unmixing problem is reformulated so as to jointly estimate the dictionary of the spectral signatures and the corresponding mixing weights. The contribution of this chapter is as follows: we start by recasting the spectral signatures identification task as a model selection problem in Section 4.1, where we reformulate the spectral unmixing along with an additional constraint on the model complexity. This brings us to consider a sparsity-based approach for spectral unmixing in Section 4.2. Next, to impose the sparsity constraint in the spectral unmixing problem, we explore the sparse spectral unmixing algorithms in Section 4.3, where a novel Poisson-based greedy algorithm is proposed. The evaluation of sparse spectral unmixing is then carried out in Section 4.4 and Section 4.5, where we focus respectively on experiments on both NaI and HPGe measurements. The Section 4.6 summaries the benefits of the sparse spectral unmixing and the perspectives of this work.

4.1 A model selection approach

The spectral unmixing addresses the problem of gamma-ray spectrum analysis by decomposing a measured spectrum into individual spectra of radionuclides. The problem has been tackled as a non-negativity regularized inverse problem to estimate the mixing weights of spectral signatures. In other words, the spectral unmixing aims at explaining the measured spectrum with the radionuclides in a given dictionary. Recall that we consider the following mixing model with N radionuclides:

$$\boldsymbol{x} \sim \mathcal{P}oisson\left(\sum_{j=1}^{N} \boldsymbol{\phi}_j a_j + \boldsymbol{b}\right) \tag{4.1}$$

Nevertheless, the set of active radionuclides that are actually present is not known in advance. A badly chosen dictionary of spectral signatures leads to increased activity estimation errors. To alleviate this problem, an alternative consists in using a large dictionary, which contains the radionuclides that are commonly present in certain type of of measurement (*e.g.*, the aerosol

sample measurement investigated in Chapter 3), as well as other radionuclides that may potentially be present in the measurement. However, as we highlighted in Chapter 3, making use of a large dictionary raises the problem of detection, with potential false positives or false negatives. This is critical for the analysis of gamma-ray spectra. Therefore, we propose jointly estimating the set of active radionuclides and their activities from a model selection perspective. In the proposed approach, one will seek the linear model of $\mathbf{\Phi}$ that best fits the observed data $\boldsymbol{x}$, with the lowest complexity as measured by the number of active radionuclides. This is graphically presented in Figure 4.1, where $\mathbf{\Phi}^c$ is the spectral dictionary of spectral signatures. Penalizing the model complexity in the selection process implies favoring solutions with few non-zero mixing weights.

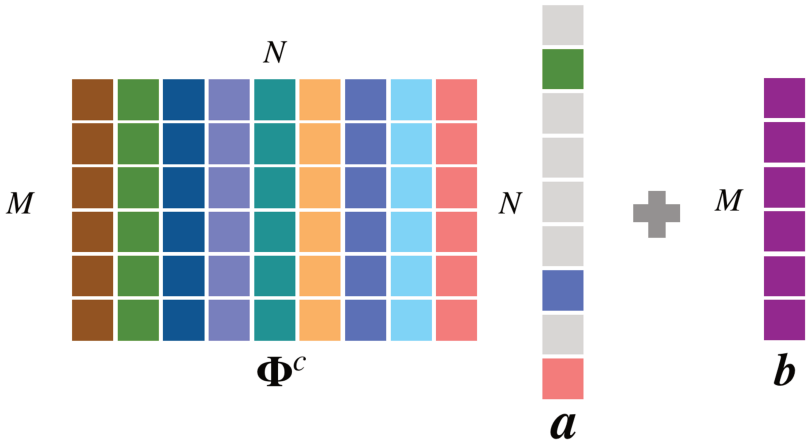

Figure 4.1 – Illustration of model selection in matrix form.

More formally, we extend the spectral unmixing to the joint estimation of the active radionuclides by adding a model complexity penalty term to the objective function:

$$\hat{\boldsymbol{a}} \in \underset{\boldsymbol{a}}{\operatorname{argmin}}\, f(\boldsymbol{a}) + i_{\cdot \boldsymbol{a} \geq 0} + \mathcal{J}(\boldsymbol{a}) \tag{4.2}$$

where the role played by this extra regularization $\mathcal{J}(\boldsymbol{a})$ is to penalize the complexity of the mixture model, by limiting the number of estimated "active" radionuclides.

As reviewed in [Stoica and Selen, 2004], very common model complexity penalizations traditionally include information criteria, such as the AIC (Akaike Information Criterion) and BIC (Bayesian Information Criterion) and their alternatives. They are well known as statistical criteria to compare

candidate models, which allows penalizing the number of parameters in the model to avoid the over-fitting.

It has to be noticed that other more recent information criteria such as the Deviance Information Criterion (DIC - [Spiegelhalter et al., 2002]) could be envisaged, but they would require resorting to MCMC-based solvers, which is computational difficult to be implemented. In the following, we will mainly focus on the sparsity as a model complexity penalization.

4.2 Sparse solution

The objective of the model selection in the spectral unmixing is to find the smallest subset of columns of $\mathbf{\Phi}^c$ that best explains the measured spectrum. It is commonly done by adding a sparsity regularization in the objective function that enforces the number of active radionuclides to be low while still explaining the data.

One can tackle the sparsity constraint with:

- ℓ_0 -"pseudo-norm", which is defined with:

  $\|\boldsymbol{a}\|_0$ = the number of non-zero elements in $\boldsymbol{a}$.

  The solution $\boldsymbol{a}$ is said to be k-sparse if $\|\boldsymbol{a}\|_0 \leq k$, which naturally induces the sparsity constraint.

- As a relaxation of ℓ_0-"norm", ℓ_1-"norm", noted $\|\boldsymbol{a}\|_1$, is the sum of absolute values of elements in $\boldsymbol{a}$. It is easier to solve due to the convexity of $\|\boldsymbol{a}\|_1$.

However, the ℓ_1 that imposes a threshold of the solution is not suitable in the Poisson noise case, it considers an additive noise independent to the data, that is not true in the Poisson model. The ℓ_0 sparsity regularization is therefore needed in the Poisson-based spectral unmixing. Fortunately, the dimension of spectral signatures dictionary is low in the gamma-ray spectrum analysis. The straightforward search of the subset of active radionuclides is feasible, which allows solving the ℓ_0 minimization with greedy sparse regression methods.

The sparse spectral unmixing can be formulated as follows:

$$\hat{\boldsymbol{a}} \in \underset{\boldsymbol{a}}{\operatorname{argmin}}\, f(\boldsymbol{a}) + i_{\cdot \boldsymbol{a} \geq 0} \quad s.t. \quad \|\boldsymbol{a}\|_0 \leq k \tag{4.3}$$

where the sparsity constraint enforces the mixing weights vector $\boldsymbol{a}$ to have exactly k non-zero elements.

4.3 Greedy algorithm to identify active radionuclides

4.3.1 Greedy algorithms in least squares problem

Greedy algorithms are involved in the ℓ_0 optimization problem. These algorithms have been proposed to find the sparse solution in least squares problem, in which the selection of columns of $\mathbf{\Phi}^c$ starts by an empty support, then the support is updated step by step with the element that optimally solve the problem. Algorithms in such category includes the Matching Pursuit (MP), [Mallat and Zhang, 1993] and Orthogonal Matching Pursuit (OMP), [Pati et al., 1993], which allows sequentially selecting the signatures in the dictionary $\mathbf{\Phi^c}$ that has the largest correlation with the current residual.

Let's now investigate the use of OMP algorithm to the spectral unmixing problem. Recall the gamma-ray spectrum model:

$$\boldsymbol{x} = \mathbf{\Phi}\boldsymbol{a} + \boldsymbol{b} + \boldsymbol{n} \tag{4.4}$$

In such OMP algorithm, we make use of the iterative re-weighted least squares mentioned in Chapter 3 to estimate the mixing weights with selected active radionuclides. The pseudo-code of the OMP algorithm for solving the sparse solution of Eq.(4.4) is stated in Algorithm 5.

However, such algorithm have been developed to find the sparse solution to an underdetermined system (*i.e.*, $\mathbf{\Phi} \in \mathbb{R}^{M\times N}$: $M < N$). This is not the case of the gamma-ray spectral unmixing problem. Furthermore, the main objective of the sparse spectral unmixing here is to select the active radionuclides, which requires that the capacity to accurately identify radionuclides when the noise is low. Therefore, a Poisson-based OMP algorithm is particularly needed.

4.3.2 The Poisson OMP Algorithm

Only a few studies have been carried out in Poisson-based greedy algorithms. An extension to the Poisson denoising case has been published in [Dupé and Anthoine, 2013]. The algorithm selects new variables based on the minimization of the gradient of the Poisson negative log-likelihood. This method requires the number of active radionuclides k to be known, which is however not true in gamma-ray spectrum analysis since the number of active radionuclides is unknown for a measured spectrum.

We rather extend the OMP algorithm to $\mathcal{P}$-OMP (Poisson-based OMP) described in Algorithm 6. It selects forward the radionuclides in $\mathbf{\Phi}^c$ by sequentially adding the radionuclide that maximizes the Poisson likelihood. More precisely, the model is initialized with the background spectrum $\boldsymbol{b}$, at

Algorithm 5 Pseudo-code of OMP algorithm

Input:
Measured spectrum: $\boldsymbol{x}$ and background radiation spectrum $\boldsymbol{b}$

The spectral signatures: $\boldsymbol{\Phi}^c = \phi_1 ... \phi_N$
($[1, ...N]$: each index for a radionuclide in $\boldsymbol{\Phi}^c$)

Initialization:
The selected indices: $I_0 = \emptyset$, the residual $r^0 = \boldsymbol{x} - \boldsymbol{b}$

while the stopping condition is not achieved **do**

$i = i + 1$

Find the column of $\boldsymbol{\Phi}^c$ that solves:

$$\underset{j}{\operatorname{argmax}} \|\boldsymbol{r}^{i-1}\boldsymbol{\Phi}^c\|$$

Add the j^{th} column to the selected radionuclides: $I_i = I_{i-1} \cup j$

Estimate $\hat{\boldsymbol{a}}_i$ with selected radionuclides ($\boldsymbol{\Phi}^c[I_i]$) and compute the new residual with:

$$r^i = \frac{\boldsymbol{x} - \boldsymbol{\Phi}^c[I_i]\hat{\boldsymbol{a}}_i - \boldsymbol{b}}{\boldsymbol{\Phi}^c[I_i]\hat{\boldsymbol{a}}_i + \boldsymbol{b}}$$

end while

each step, each of the non-selected radionuclides is added into the spectral signatures for activity estimation using the Poisson unmixing algorithm described in Chapter 3. At the end of the iteration, it selects the radionuclide that minimizes the Poisson-based cost function. The algorithm stops when certain stop condition is achieved.

4.3.3 Stopping criteria for radionuclides identification

The OMP and $\mathcal{P}$-OMP algorithms sequentially select the radionuclides at each step. Once a radionuclide has been added into the spectral signatures, a stopping condition needs to be applied to compare two candidate models:

- M_0: the model with selected radionuclides
- M_1: the model with an extra active radionuclide

As mentioned in Section 4.1, model selection methods such as AIC and BIC are commonly used to penalize the model complexity.

Algorithm 6 Pseudo-code of Poisson-based OMP algorithm

Input:
Measured spectrum: $\boldsymbol{x}$ and background radiation spectrum $\boldsymbol{b}$

The spectral signatures: $\boldsymbol{\Phi}^c = \phi_1 ... \phi_N$
($[1, ...N]$: each index for a radionuclide in $\boldsymbol{\Phi}^c$)

Initialization:
The selected indices: $I_0 = \emptyset$

The indices to check: $I^c = [1...N]$

The neg-log-likelihood (with background spectrum): $\mathcal{L}_0 = \boldsymbol{b} - \boldsymbol{x} \odot \log(\boldsymbol{b})$

while the stopping condition is not achieved **do**

$i = i + 1$

for $j \in I^c$ **do**

Add a radionuclide to the subset of spectral signatures:

$$I^{test} \leftarrow I_{i-1} \cup j$$

Estimate mixing weights $\boldsymbol{a}^{new}$ with $\boldsymbol{\Phi}^c[I^{test}]$

Compute the neg-log-likelihood:

$$\boldsymbol{\Phi}^c[I^{test}]\boldsymbol{a}^{new} + \boldsymbol{b} - \boldsymbol{x} \odot \log(\boldsymbol{\Phi}^c[I^{test}]\boldsymbol{a}^{new} + \boldsymbol{b})$$

end for

Find j^* that minimizes the neg-log-likelihood

Add the j^{*th} column to the selected radionuclides: $I_i = I_{i-1} \cup j^*$

Remove the selected radionuclide j^* from I^c.

end while

To use these information criteria as stopping rule, the

$$AIC = 2 * k - 2 \ln \mathcal{L}, \quad BIC = k * N - 2 \ln \mathcal{L}$$

need to be calculated at each straightforward selection step, where L is the likelihood function, k is the number of parameters to be estimated (*i.e.*, the number of selected radionuclides), and N is the sample size (*i.e.*, the number of channels in the spectrum). The algorithm stops when the information criteria increases.

However, these model selection methods can not provide an idea about the false positive rate. To consider the false positive rate of adding a new radionuclide to the model, we propose to apply a stopping criteria with a statistical test under the following hypotheses:

- H_0: the model M_0 is true
- H_1: the model with an extra active radionuclide M_1 is true

For this purpose, the statistical deviance test between M_0 and M_1 ([Das-Gupta, 2008]) is well-suited, which is defined by the difference of their neg-log-likelihood:

$$D = -2\left(\mathcal{L}_1 - \mathcal{L}_0\right) \tag{4.5}$$

where $\mathcal{L}_0$ and $\mathcal{L}_1$ stand for the neg-log-likelihood calculated with model M_0 (selected radionuclides) and M_1 (selected radionuclides + an extra radionuclide) respectively. More precisely, as we presented in Chapter 3, for the OMP algorithm with weighted least squares estimation, the neg-log-likelihood function takes the form of:

$$\mathcal{L}\left(\boldsymbol{x}|\boldsymbol{a}\right) = \left(\boldsymbol{\Phi a} + \boldsymbol{b} - \boldsymbol{x}\right)^T \boldsymbol{W}^{-1} \left(\boldsymbol{\Phi a} + \boldsymbol{b} - \boldsymbol{x}\right)$$

For the Poisson based OMP algorithm, the Poisson neg-log-likelihood takes the form of:

$$\mathcal{L}\left(\boldsymbol{x}|\boldsymbol{a}\right) = \boldsymbol{\Phi a} + \boldsymbol{b} - \boldsymbol{x} \odot \left(\boldsymbol{\Phi a} + \boldsymbol{b}\right)$$

When M_0 is nested within M_1 and M_1 is the true model, the statistical deviance asymptotically follows a χ^2 distribution with d degrees of freedom (d is the difference of the number of radionuclides in the two models). However, the models are not nested in the straightforward search of $\mathcal{P}$-OMP algorithm, since among the radionuclides to be tested, the true model may be a combination of radionuclides. In such a multiple hypothesis testing problem, the Bonferroni correction [Benjamini and Hochberg, 1995] is commonly used, which allows to control the number of false positives based on a p-value corrected by the number of hypotheses.

The selection of extra radionuclides stops whenever the deviance is consistent with a χ^2 distribution with the critical p-value:

$$\alpha = \frac{\alpha_0}{n} \tag{4.6}$$

where n is the number of radionuclides to be tested at this step and α_0 is the desired false positive rate, while $\alpha_0 = 0.01$ is used in the experiments of this chapter.

4.4 Application of $\mathcal{P}$-OMP to HPGe measurements

4.4.1 Data description

In this section, the sparse spectral unmixing is applied to analyze the progressive measurements of aerosol measurements described in Chapter 3, as well as the simulations that mimic these mixing scenarios with 10 radionuclides:

^{7}Be, ^{22}Na, ^{40}K, ^{137}Cs, ^{210}Pb, ^{208}Tl, ^{212}Bi, ^{212}Pb, ^{214}Bi, ^{214}Pb.

In the sparse spectral unmixing setting, the implementation of $\mathcal{P}$-OMP is based on a complex spectral dictionary, which consists of these 10 radionuclides and other 8 radionuclides:

^{110m}Ag, ^{234}Th, ^{228}Ac, ^{106}Rh, ^{131}I ,^{60}Co, ^{129}I, ^{54}Mn,

where we aim to identify the active radionuclides from these 18 radionuclides and estimate their mixing weights.

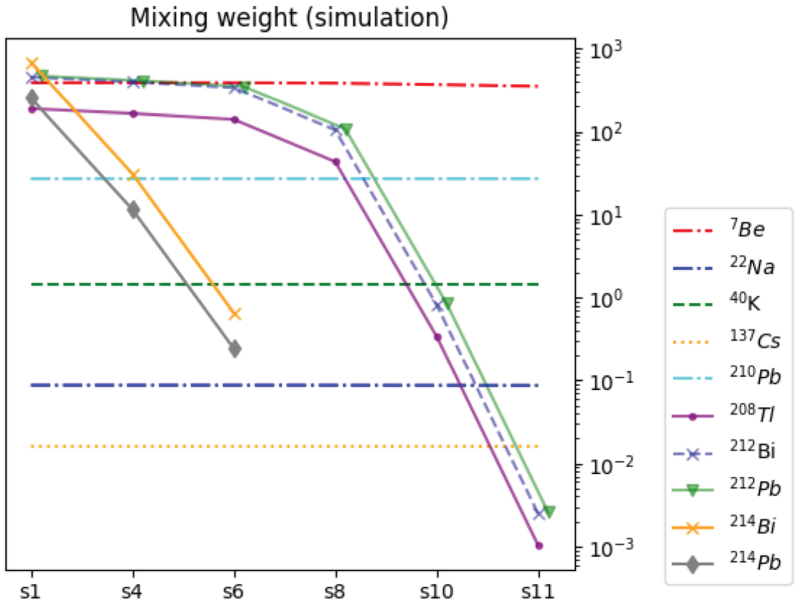

Figure 4.2 – The mixing weights of radionuclides used in the simulations.

4.4.2 Evaluation on simulated spectra

The $\mathcal{P}$-OMP algorithm is applied to Monte Carlo simulations performed for the measurements $s1$, $s4$, $s6$, $s8$, $s10$, $s11$ described in Table 3.2. For each mixing scenario, 100 simulations are generated.

In the simulation process, recall that the long-lived radionuclides remain their activity level during the measurement, whereas the short-lived radionuclides decay as time goes on (see evolution of their mixing weights in Figure 4.2). Figure 4.3 shows the detection rate of $\mathcal{P}$-OMP for each radionuclide, they are calculated with 100 simulations of each measurement.

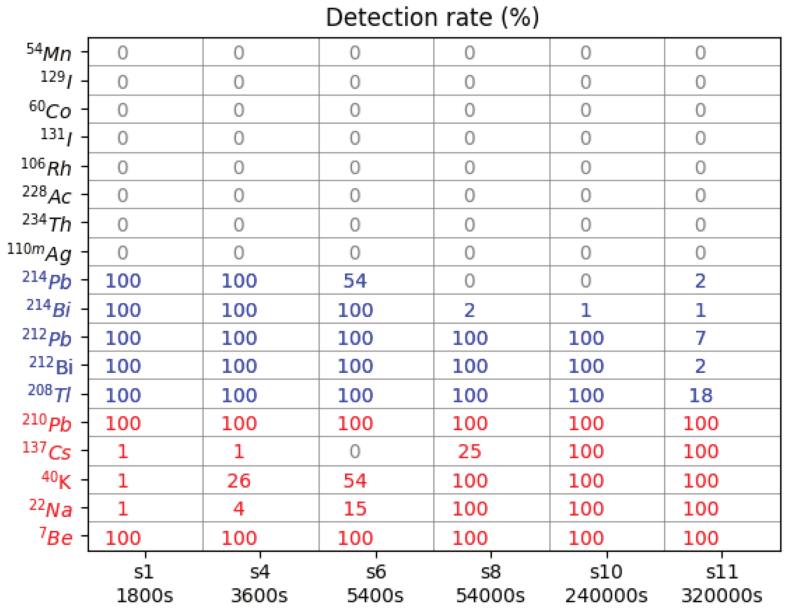

Figure 4.3 – Detection rate of radionuclides with $\mathcal{P}$-OMP for simulated spectra according to the measurements: s1, s4, s6, s8, s10 and s11 (counting time is indicated for each measurement). Long-lived radionuclides (red) and short-lived radionuclides (blue).

As result, the detection rates of radionuclides calculated from Monte Carlo simulations confirms a good identification of active radionuclides. The detection rates of 8 radionuclides that not participate in the simulations are 0. Meanwhile, the predominant spectral contributions, such as ^{7}Be and ^{210}Pb are detected with a detection rate of 100%. In contrast, short-lived radionuclides (presented in blue) are selected in the first measurements and less detected in the last measurements. It should be noted that, the low-level radionuclides ^{22}Na and ^{40}K are detected from s8, the ^{137}Cs is detected from s10 with increasing counting statistics (*i.e.*, counting time).

4.4.3 Evaluation on measured spectra

The $\mathcal{P}$-OMP algorithm is then applied to the measurements s1, s4, s6, s7, s10 and s11 described in Table 3.2. The results shown in Figure 4.4 consist of: i), the colorbars displayed in the first column for each measurement reports the update sequence of radionuclides, it presents the selection order of the radionuclides with colors from blue to red. The first rejection of each measurement is indicated with a red cross, which do not satisfies the statistical deviance test. ii), the activity in Bq resulting from Genie 2000 are presented in the second column for each measurement (NS for non-significant).

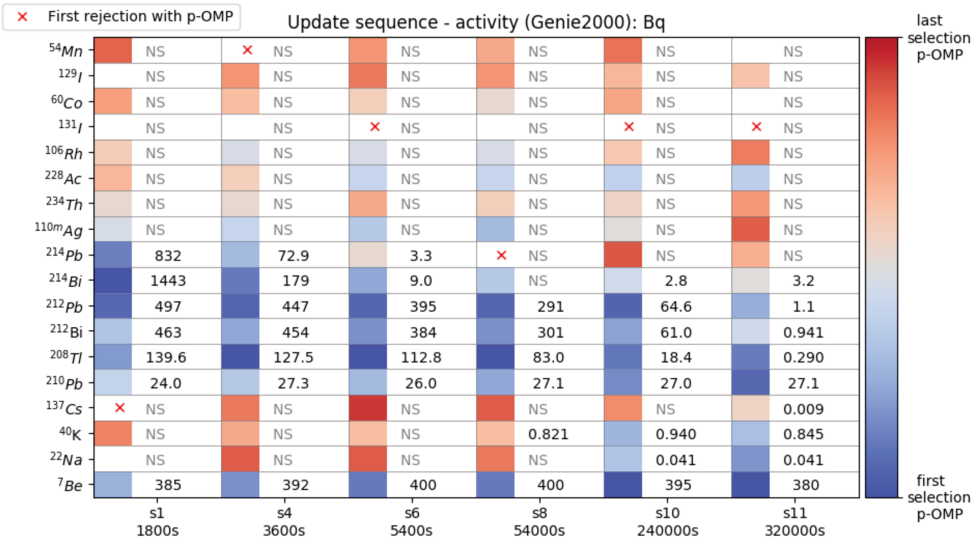

Figure 4.4 – Results of $\mathcal{P}$-OMP on real measurements, the selection order of radionuclides is presented with colors from blue to red. Activities of radionuclides obtained with Genie 2000 are presented for comparison purpose.

Overall these results are in agreement with results obtained with the simulations. In the first measurements, ^{208}Tl, ^{212}Bi, ^{212}Pb, ^{214}Bi, ^{214}Pb are firstly selected that implies their significance. The decay process of these short-lived radionuclides leads to lower activities as time goes on. Therefore, a better counting statistics is obtained by increased counting time for long-lived radionuclides and ^{7}Be, ^{22}Na, ^{40}K, ^{137}Cs, ^{210}Pb are detected with increased significance, this can be confirmed by the activities measured with Genie 2000.

For ^{110m}Ag, ^{234}Th, ^{228}Ac, ^{106}Rh, ^{131}I ,^{60}Co, ^{129}I, ^{54}Mn, the results given by Genie 2000 are more selective than the selection performed with $\mathcal{P}$-OMP.

Indeed, the results obtained with Genie 2000 is according to Genie 2000 + a post-analysis procedure, while some false identifications of radionuclides are rejected. Furthermore, the results of Genie 2000 are given based on certain decision threshold level which implies the significance of the radionuclides' presence (see details in Chapter 5).

However, one limitation for applying $\mathcal{P}$-OMP on real measurements of HPGe detectors is the bias of the Poisson spectral unmixing. Firstly, the spectral signatures of radionuclides are simulated with MCNP-CP, which provides bias on gamma-ray responses. Secondly, background spectra are measured every two months, $\boldsymbol{b}$ used in the spectral unmixing process is generated from a previous measurement of background spectrum, which is not the actual background at the time of the measurement. This bias on background spectrum leads to over/under estimations since the background consists of several radionuclides which also participate in the measured sample.

4.5 Application of $\mathcal{P}$-OMP to NaI measurements

4.5.1 Description of the data

The spectral unmixing applied to the activity estimation from NaI gamma-ray measurements have been studied in [Paradis et al., 2020] based on the multiplicative update algorithm described in Chapter 3. The investigations in this paper consider that the set of active radionuclides is known. To further overcome the radionuclides' identification, [André et al.,] makes use of the $\mathcal{P}$-OMP algorithm to impose the sparsity constraint into the spectral unmixing algorithm proposed in [Paradis et al., 2020]. In this section, we aim to further investigate how the $\mathcal{P}$-OMP algorithm behaves when the correlation of radionuclides' spectra between the spectra of the spectral dictionary increases, which is more challenging in NaI spectra analysis.

It is indeed expected that larger correlation will hamper the estimation bias of the activities, and more importantly the detection capabilities of the sparse spectral unmixing algorithm. For that purpose, we apply $\mathcal{P}$-OMP to simulated measurements of a 3"x3" NaI(Tl) detector without shielding using point sources placed at a distance of 1 m [Paradis et al., 2020]. The spectral dictionary is composed of ten spectral signatures, which are made of 1024 channels. These signatures correspond to the detector response of ten gamma-emitting radionuclides with photon emissions covering a range of energies between 40 keV and 2 MeV:

^{57}Co, ^{60}Co, ^{88}Y, ^{133}Ba, ^{134}Cs, ^{137}Cs, ^{152}Eu, ^{207}Bi, ^{241}Am, ^{237}Np.

Simulations of different mixing scenarios are performed with the following choice of radionuclides (*i.e.*, active radionuclides present in the spectrum).

The choice of ^{57}Co, ^{60}Co, ^{133}Ba, ^{137}Cs and ^{241}Am is particular relevant as they correspond to the main radionuclides that need to be identified for illicit radioactive material monitoring [IEC 62484:2010, 2010]. Furthermore, ^{152}Eu has been chosen as its signature covers a large range of energies, 120 keV to 1410 keV, which is largely correlating with other radionuclides. The following scenarios have been considered :

- **Scenario I**: following [André et al.,], the scenario considers measurements where only four radionuclides are present in the mixture: ^{57}Co, ^{133}Ba, ^{152}Eu, ^{241}Am. A natural background spectrum is further added. This scenario allows to compare the precision of the unmixing methods for both estimation quality and detection capability.

- **Scenario II**: in these experiments, ^{137}Cs is added to the mixture of Scenario I. This allows to evaluate the ability to detect low-activity radionuclides such as ^{137}Cs, as well as the impact of the estimation on other radionuclides. These experiments are reminiscent of the ^{137}Cs estimation experiment we performed in Chapter 3.

- **Scenario III**: ^{60}Co is added to the standard mixture Scenario I. This set-up allows to highlight how radionuclides' identification can be hampered when their spectral signatures have a significant overlap, which is the case of ^{57}Co, ^{60}Co and ^{152}Eu.

For a comparison purpose, the OMP algorithm based on the iterative re-weighted least squares estimation and the $\mathcal{P}$-OMP algorithm based on the Poisson estimation presented in Section 4.3 are applied to analyze the simulated spectra of the above three scenarios. At the end of the section, we compare the proposed deviance-based stopping criteria to those based on information criteria.

4.5.2 Application to NaI measurements - scenario I

This scenario has been investigated in [André et al.,] to simulate measurements similar to illicit radioactivity monitoring with NaI-based detectors. Four radionuclides and a background spectrum are considered in the measurements, their proportion can be found in Table 4.1). To better illustrate the correlations between individual spectra of the measurements, the spectral signatures of the above 4 active radionuclides are shown in Figure 4.5.

We quantify the estimation bias of the mixing weights (*i.e.*, the activities) of these radionuclides as well as the detection performances of the $\mathcal{P}$-OMP and OMP algorithms, with an empirical evaluation of the false positive and

false negative rates for each individual radionuclide. These experiments are composed of 250 Monte-Carlo simulations with different stochastic realizations.

radionuclide	proportion of the total counts number (%)
^{57}Co	14.2%
^{133}Ba	17.8%
^{152}Eu	14.2%
^{241}Am	8.9%
background	44.9%

Table 4.1 – Proportions of radionuclides in scenario I.

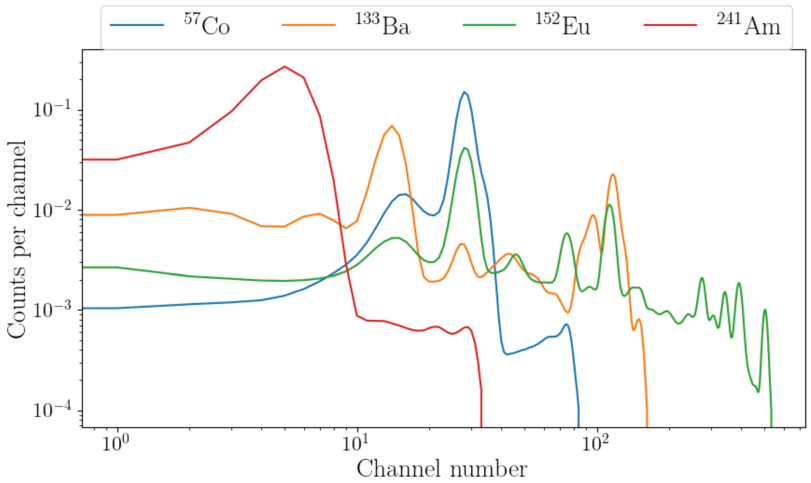

Figure 4.5 – Spectral signatures (NaI) of the radionuclides in scenario I.

Results - estimation bias

Figure 4.6 displays the evolution of the relative bias for the above four radionuclides as a function of the total number of counts from 1400 to 70000. Each point corresponds to the median relative bias from the 250 Monte-Carlo simulations and the error bars display the first and last quartiles. This figure first shows that the relative bias is significantly improved for all radionuclides by using the $\mathcal{P}$-OMP algorithm, and especially for ^{60}Co, ^{133}Ba and ^{152}Eu. Indeed, the spectrum of ^{241}Am is less overlapped with other radionuclides (see their spectral signatures shown in Figure 4.5). As well, the error bars of

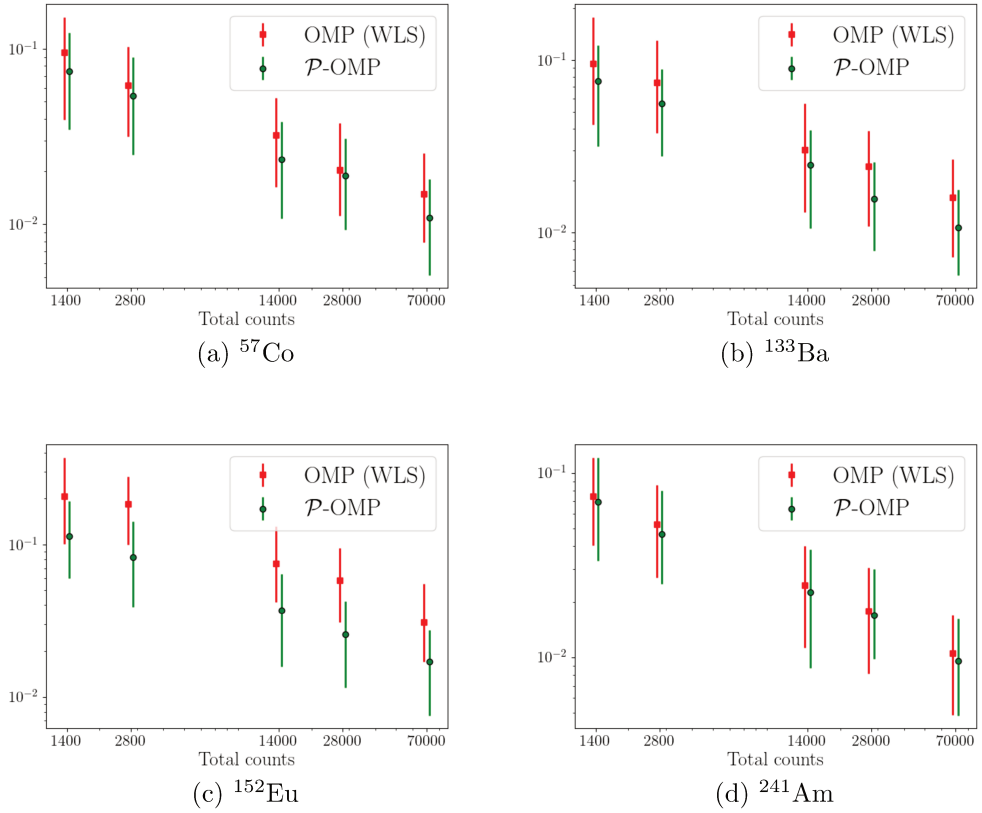

(a) ^{57}Co (b) ^{133}Ba

(c) ^{152}Eu (d) ^{241}Am

Figure 4.6 – Relative errors comparison of active radionuclides (Scenario I).

the solutions derived with $\mathcal{P}$-OMP are narrower than with the OMP equipped with a iterative re-weighted least squares minimization scheme.

Let us recall that we highlighted in Chapter 3 that a iterative re-weighted least-squares estimator generally leads to results that are close to Poisson unmixing, when the number of measured counts is large enough. However, these results holds when the dictionary of active radionuclides is known, which is not the case in the current experiments. The discrepancy between $\mathcal{P}$-OMP and OMP is more likely to be related to a difference in detection performances.

Results - radionuclides' identification

As results, both algorithms we compared perform similarly with no false negatives for 4 active radionuclides. More interestingly, table 4.2 features the false positive rate of non-active radionuclides for both methods. If both

methods exhibit no false positives for most radionuclides, OMP has significant false detection of ^{207}Bi with a rate between 16 and 22%, and ^{237}Np, with a rate between 27.6 and 36%. From Figure 4.7, we can see that the spectral signatures of these two radionuclides are overlapped with that of the active radionuclide ^{133}Ba, it leads to their false identification with OMP algorithm and further implies an increase of the estimation bias of the 4 radionuclides that actually compose the measurements.

Total counts		**1400**	**2800**	**14000**	**28000**	**70000**
^{207}Bi	OMP (WLS)	16.4	16.0	20.0	21.6	22
	$\mathcal{P}$-OMP	0	0	0	0	0
^{237}Np	OMP (WLS)	36.0	34.8	30.8	27.6	31.2
	$\mathcal{P}$-OMP	0	0	0	0	0

Table 4.2 – False positive rate of non-active radionuclides (%) (Scenario I).

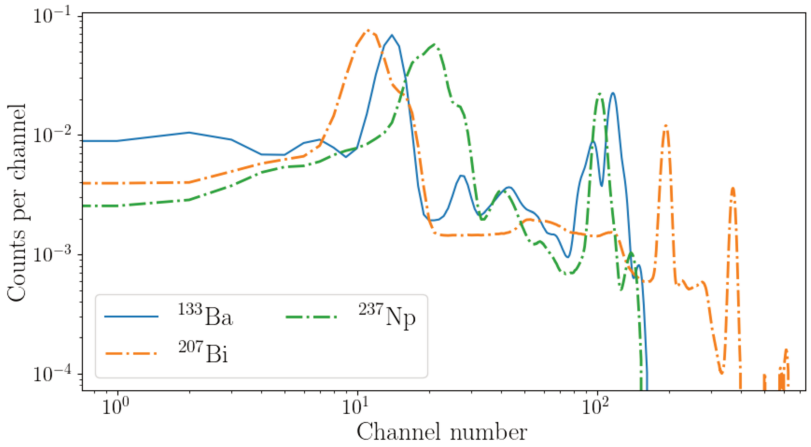

Figure 4.7 – Spectral signatures (NaI) of: ^{133}Ba (active), ^{207}Bi and ^{237}Np (non-active).

4.5.3 Application to NaI measurements - scenario II

The goal of the second scenario is to investigate the sensitivity of both $\mathcal{P}$-OMP and OMP for detecting low-level active radionuclides. In the same spirit as the experiment of Section 3.4, ^{137}Cs is added to the mixtures of scenario I (see spectral signatures in Figure 4.8). The average number of

counts for the background is 1250, ^{241}Am is 250, ^{133}Ba is 500, ^{57}Co is 400 and ^{152}Eu is 400.

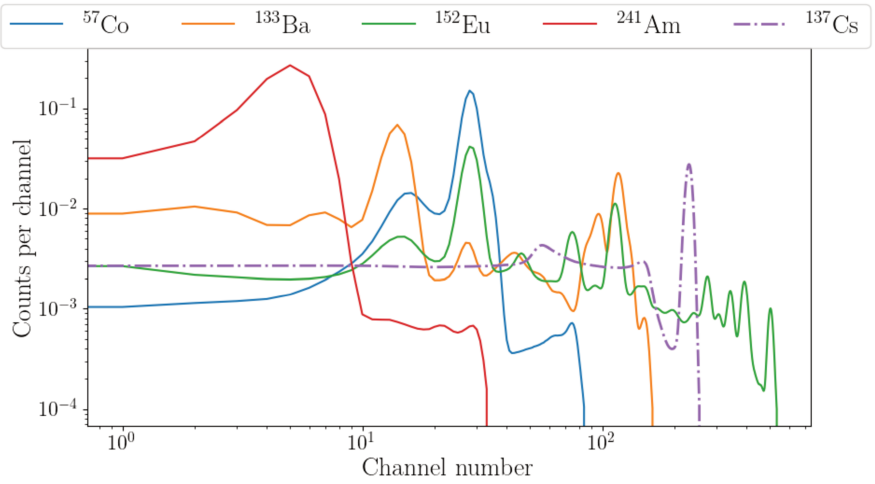

Figure 4.8 – Spectral signatures (NaI) of the radionuclides in scenario II.

The estimation and detection performances are then evaluated when the mean number of counts of ^{137}Cs evolves from 10 to 500, for a average total number of counts that varies from 2810 to 3300 (*i.e.* the contribution of ^{137}Cs varies from 0.3% to 15.1%).

Results

Figure 4.9 displays the evolution of the relative estimation bias of the ^{137}Cs estimation as a function of its average number of counts. As expected, the precision of both the $\mathcal{P}$-OMP and OMP algorithms are significantly hampered as the activity level decreases. For activity levels lower than 300, the OMP algorithm equipped with a iterative re-weighted least squares minimization procedure provides biases of the order or larger than 100% while $\mathcal{P}$-OMP yields a median relative bias lower than 10% when the activity of ^{137}Cs is larger than 50. This is related to a larger false negative rate of ^{137}Cs as testified by Table 4.3. The relative bias evolves similarly to the FNR, which is larger than 70% for OMP when the activity level is lower than 300, while it is not significant for $\mathcal{P}$-OMP when it is larger than 50 (up to the precision of the 250 Monte Carlo simulations used to derive these numbers).

The poor detection performances of OMP likely originates from the fact that it does not perfectly account for the Poisson statistics of the underlying physical process. It is further interesting to note that, due to the higher

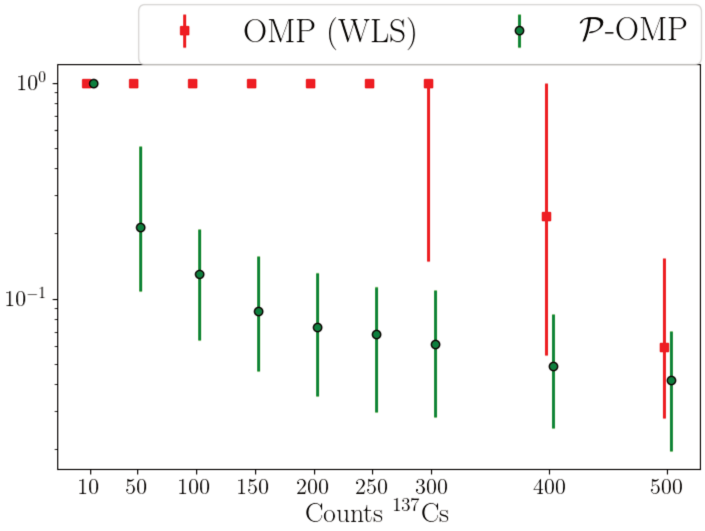

Figure 4.9 – Relative estimation bias of the estimation of ^{137}Cs obtained for scenario II, as a function of the counts number of ^{137}Cs.

Counts ^{137}Cs	**10**	**50**	**100**	**150**	**200**	**250**	**300**	**400**	**500**
OMP (WLS)	99.8	99.8	97.0	86.8	80.8	76.8	70.4	49.0	20.8
$\mathcal{P}$-OMP	98.4	19.2	0	0	0	0	0	0	0

Table 4.3 – False negative rate of ^{137}Cs (%) (Scenario II)

correlation between radionuclides' spectral signatures with NaI detectors, the detection ability of OMP is also limited by the presence of ^{152}Eu, with which ^{137}Cs tends to interact. This is shown by the increased bias of ^{152}Eu when the level of ^{137}Cs increases, as shown in Figure 4.10.

Similarly to the conclusion we drew from scenario I, the increased FPR of some radionuclides, such as ^{207}Bi and ^{237}Np is also likely to further limit the detection capacity of low-level radionuclides.

4.5.4 Application to NaI measurements - scenario III

Scenario III is similar to scenario I with the exception that both isotopes of Cobalt, ^{57}Co and ^{60}Co, are now active. This scenario is particularly interesting as both isotopes of Cobalt have signatures that tend to correlate significantly with ^{152}Eu, that is expected to largely degrade the estimation and detection performances of both algorithms. The average number of counts for the background is 1250, ^{241}Am is 250, ^{133}Ba is 500, ^{57}Co is 400 and ^{60}Co is 400. The spectral signatures are displayed in Figure 4.11.

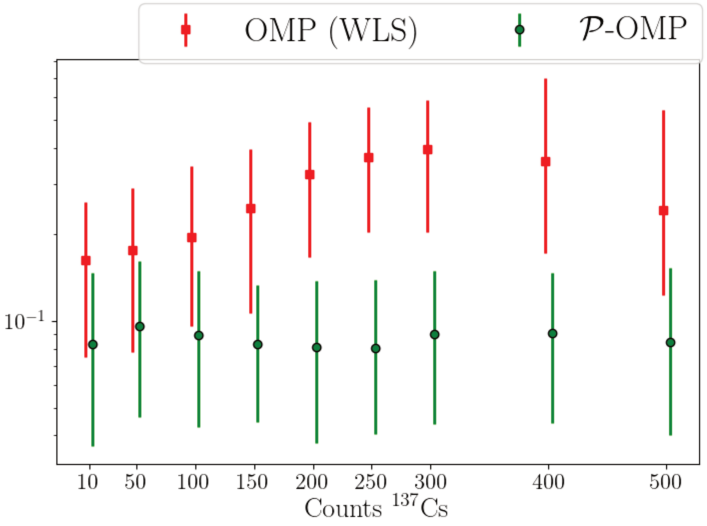

Figure 4.10 – Relative estimation bias of the estimation of ^{152}Eu obtained for scenario II, as a function of the counts number of ^{137}Cs.

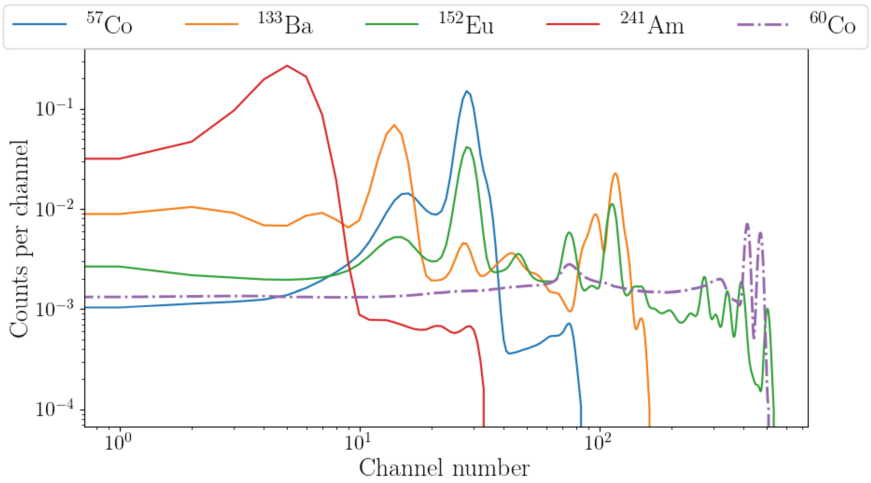

Figure 4.11 – Spectral signatures (NaI) of the radionuclides in scenario III).

The three panels of Figure 4.12 feature the evolution of the relative bias as a function of the counts number of ^{152}Eu. The first shows that the activity of ^{60}Co is very badly estimated with OMP for the whole range of ^{152}Eu activity levels we tested. This is confirmed by the false negative rates reported in Table 4.4, the detection of ^{60}Co with OMP has a FNR constantly larger than 70%. In the model selection process, the widespread energetic response of ^{152}Eu makes it more likely to be detected with respect to ^{60}Co. It has further to be noticed that the selection of ^{152}Eu rather than ^{60}Co also yields a

dramatic increase of the relative bias of ^{57}Co (see the second panel of Figure 4.12). Meanwhile, as shown in the third panel of Figure 4.12), the OMP algorithm also provides a larger estimation bias for the estimation ^{152}Eu.

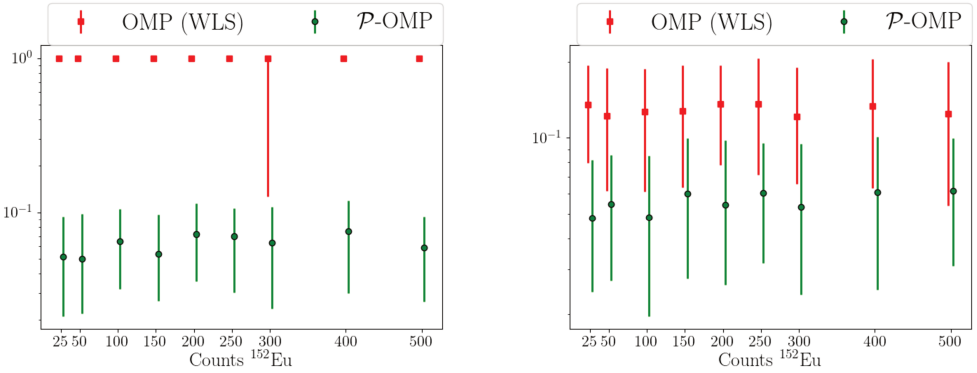

(a) ^{60}Co

(b) ^{57}Co

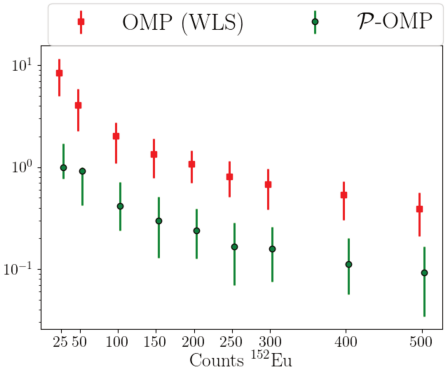

(c) ^{152}Eu

Figure 4.12 – Relative errors comparison of active radionuclides (Scenario III).

4.5.5 Stopping rule, comparing the deviance-based test with information criteria

In this paragraph, we propose substituting the deviance-based statistical test in the $\mathcal{P}$-OMP algorithm with the Akaike and Bayes information criteria. This basically boils down to evaluating either the AIC or BIC criterion at each iteration. The *optimal* model is then the one that leads to the lowest criterion value.

The following experiments are similar to the previous scenario III. Tables 4.5 4.6, 4.7 report the false positive and false negative rates for three

Counts ^{152}Eu		**25**	**50**	**100**	**150**	**200**	**250**	**300**	**400**	**500**
^{57}Co	OMP (WLS)	0	0	0	0	0	0	0	0	0
	$\mathcal{P}$-OMP	0	0	0	0	0	0	0	0	0
^{60}Co	OMP (WLS)	79.2	78.4	76.4	78.4	80.4	79.2	68	76.4	77.2
	$\mathcal{P}$-OMP	0	0	0	0	0	0	0	0	0
^{152}Eu	OMP (WLS)	10	9.2	3.2	1.2	0.4	0	0	0	0
	$\mathcal{P}$-OMP	16.4	10.4	2.4	0	0	0	0	0	0

Table 4.4 – False negative rate of ^{57}Co, ^{60}Co and ^{152}Eu (%) (Scenario III).

different values for the average total number of counts of ^{152}Eu: 25, 100 and 200.

These results first show that AIC systematically over-estimates the number of active radionuclides, leading to a detection rate of a few percents for the 5 non-active radionuclides. This holds true for the three different levels of Europium that were tested. In contrast, BIC is more conservative and leads to detection results that are closed to the deviance-based criterion, a slightly large false positive rate.

It has to be emphasized that controlling the FPR is key for tackling spectral unmixing problem, which favor the use of the deviance-based criterion along with the sparsity penalization for model selection.

	FNR of active radionuclides					FPR of non-active radionuclides				
	^{57}Co	^{60}Co	^{133}Ba	^{152}Eu	^{241}Am	^{88}Y	^{134}Cs	^{137}Cs	^{207}Bi	^{237}Np
Dev.	0	0	0	16.8	0	0	0	0.4	0	0.8
AIC	0	6.8	0	19.2	0	0	6.0	5.2	3.2	5.6
BIC	0	0	0	16.8	0	0	0.8	0.4	0	0.8

Table 4.5 – Comparison of different model complexity penalizations. Average total number of counts for ^{152}Eu of 25.

4.6 Summary of the sparse spectral unmixing

In this chapter, the spectral unmixing is reformulated with a sparsity constraint so as to estimate the subset of active radionuclides present in a measured gamma-ray spectrum. We proposed a novel Poisson Orthogonal

	FNR of active radionuclides					FPR of non-active radionuclides				
	^{57}Co	^{60}Co	^{133}Ba	^{152}Eu	^{241}Am	^{88}Y	^{134}Cs	^{137}Cs	^{207}Bi	^{237}Np
Dev.	0	0	0	1.6	0	0	0	0	0	0
AIC	0	6.8	0	2.8	0	0	4.0	8.8	7.2	7.2
BIC	0	0.8	0	1.6	0	0	0.4	0	0.8	0.8

Table 4.6 – Comparison of different model complexity penalizations. Average total number of counts for ^{152}Eu of 100.

	FNR of active radionuclides					FPR of non-active radionuclides				
	^{57}Co	^{60}Co	^{133}Ba	^{152}Eu	^{241}Am	^{88}Y	^{134}Cs	^{137}Cs	^{207}Bi	^{237}Np
Dev.	0	0	0	0	0	0	0	0	0	0
AIC	0	9.6	0	0	0	0	6.4	5.2	6.8	7.2
BIC	0	0	0	0	0	0	0	0.4	1.2	0.4

Table 4.7 – Comparison of different model complexity penalizations. Average total number of counts for ^{152}Eu of 200.

Matching Pursuit algorithm, named $\mathcal{P}$-OMP, which enables to find the sparsest solution of mixing weights that best fits the measured spectrum according to the Poisson statistics. We evaluated the performance of this $\mathcal{P}$-OMP algorithm by comparing to standard OMP algorithm based on the iterative re-weighted least squares estimation. As results, the $\mathcal{P}$-OMP is shown to provide more accurate estimation of the active radionuclides' subset, as well as their according mixing weights. This further highlights the advantage of accounting for the Poisson data error in spectral unmixing rather than weighted least squares error.

While providing promising results, assuming that the radionuclides' spectral signatures and the background spectrum are accurately known is an important limitation in real data analysis, particularly in case of aerosol measurements that we investigate, since the spectral signatures need to be simulated. In practice, the variability of spectral signatures might increase false identifications as well as estimation bias of the mixing weights. The next chapters will focus on the quantitative analysis of radionuclides' activities with experimental data, where we will discuss the error estimation with characteristic limits and propose calibrations for quantitative analysis.

CHAPTER 5

Characteristic limits in spectral unmixing

Contents

5.1 Characteristic limits in radioactivity measurements 80

5.2 Quantification with Monte Carlo simulations . . 82

5.3 Quantifying the decision threshold 85

5.3.1 Decision threshold in peak-based analysis 85

5.3.2 Decision threshold in spectral unmixing analysis . 86

5.3.3 Evaluation of the decision threshold determination 89

5.4 Confidence interval 95

5.4.1 Fisher information to compute confidence intervals 95

5.4.2 Evaluation of confidence interval in spectral unmixing 96

5.5 Discussion 98

The precise analysis of gamma-ray spectra requires two key ingredients: the first one is an efficient spectral unmixing algorithm, which we thoroughly investigated in the previous chapters. The second ingredient, which is key to reach a truly metrological analysis quality, is the quantification of the errors of the estimation and the detection procedures. As detailed in-depth in this chapter, this requires evaluating the so-called characteristic limits, which are essential for decision making purposes in the quantitative analysis of the radioactivity measurements. The assessment of two major characteristic

limits: the decision threshold and the limits of the confidence interval will be thoroughly evaluated in this chapter.

While being well studied in traditional peak-based analysis, the main goal of this chapter is to introduce and evaluate a new approach to derive such characteristic limits for the spectral unmixing algorithms we introduced previously. More precisely, the contribution of this chapter is as follows:

- We first focus on the concept of characteristic limits for radioactivity measurements in Section 5.1, where we present their definitions.
- In Section 5.2, we review how the characteristic limits can be calculated from Monte Carlo simulations, which were used to determine the significance of results provided with spectral unmixing in Chapter 3.
- The assessment of the decision threshold in spectral unmixing is investigated in Section 5.3.
- The evaluation of the confidence interval of the activity estimation is then carried out in Section 5.4.

The proposed approaches to derive characteristic limits have been evaluated and validated with realistic simulations of HPGe measurements and NaI measurements. Section 5.5 finally discusses their metrological use in the gamma-ray spectrum analysis.

5.1 Characteristic limits in radioactivity measurements

Refer to [ISO 11929, 2010], the notations below are used in the description of the characteristic limits:

- Y: Measurand, the quantity of interest.
- y: Determined value of the measurand Y (*i.e.*, the estimate of Y).
- $\tilde{y}$: True value of the measurand.

We first present the classical statistical hypothesis framework used for decision making in gamma-ray spectrum analysis. It is commonplace to consider testing hypotheses with the two alternatives (associated with type I error and type II error described in Table 5.1):

- H_0: the null hypothesis, where a given radionuclide is not "active".
- H_1: the alternate hypothesis, where the radionuclide is present in the mixture.

	H_0 is true	H_1 is true
rejecting H_0	**Type I error**: the error of rejecting H_0 when it is true, the probability of committing a type I error is denoted by α, called false positive rate.	
accepting H_0		**Type II error**: the error of accepting H_0 when H_1 is true, the probability of committing a type II error is denoted by β, called false negative rate.

Table 5.1 – Two types of errors of hypotheses test.

The standardization document [ISO 11929, 2010] defines the determination of the characteristic limits, namely the decision threshold, the detection limit, and limits of the confidence interval for ionizing radiation measurements. It provides a framework for the computation of the characteristic limits. Referring to [Weise et al., 2005], [Michel, 2016], the definition and interpretation of the characteristic limits for some estimate y of a measurand Y are as follows:

- **Decision threshold (DT)** allows a decision to be made on whether or not the physical effect quantified by the measurand is present.

  The determination of DT is related to the Type I error described in Table 5.1. When the quantity y exceeds the critical value (DT), the null hypothesis H_0 should be rejected with respect to a given false positive rate (FPR). It can be described with:

  $$\alpha = \mathcal{P}\left(y \geq DT | \tilde{y} = 0\right) \tag{5.1}$$

  where $\tilde{y}$ is the true value of the measurand and α is the desired critical FPR.

- **Detection limit (DL)** indicates the smallest true quantity value of the measurand, which can still be detected with the applied measurement procedure.

  The determination of DL is related to the Type II error described in Table 5.1. It is selected with respect to a desired false negative rate (FNR) based on the decision threshold level.

More precisely, the detection limit (DL) is the smallest value that provides a desired Type II error probability β:

$$\beta = \mathcal{P}\left(y \leq DT | \tilde{y} = DL\right) \tag{5.2}$$

where the DT is given and $\tilde{y}$ is the true value of the measurand.

- **The confidence interval** for the estimate y is an interval that has a probability γ of containing the true value $\tilde{y}$.

In this work, we mainly focus on the determination of the decision threshold and the confidence interval, since in practice, these two ingredients allow us to determine whether the resulting activity of a radionuclide is significant. Firstly, we can evaluate the measurement uncertainty of each radionuclide from the combination of the confidence interval and other metrological uncertainties. Secondly, for the decision making purpose, it is sufficient to compare the low boundary of the measurement uncertainty to the decision threshold. In practice, the detection limit can be used as reference values, which is however not useful in case of the aerosol measurements that will be analyzed.

5.2 Quantification with Monte Carlo simulations

A traditional approach to quantify the characteristic limits for some estimation method is to make use of Monte-Carlo simulations. Indeed, we pointed out in Chapter 3 that the significance level of the radionuclide's presence and the confidence interval of the activity estimation with spectral unmixing can be derived from Monte Carlo simulations.

In this chapter, the evaluation of characteristic limits are carried out with the radionuclides' realistic mixture of aerosol measurements (see Chapter 3). Recall that the mixture consists of 10 radionuclides: ^{7}Be, ^{22}Na, ^{40}K, ^{137}Cs, ^{210}Pb, ^{208}Tl, ^{212}Bi, ^{212}Pb, ^{214}Bi, ^{214}Pb. It should be noted that the evaluations from this realistic mixing scenario are meaningful since the counting statistics is similar to typical aerosol routine measurements. In this context we focus on the assessment of characteristic limits for 4 radionuclides: ^{7}Be, ^{22}Na, ^{137}Cs, ^{212}Pb, since these radionuclides cover the whole energy range and different statistic regimes. The simulation model of 10 radionuclides and the contribution of these 4 radionuclides are displayed in Figure 5.1.

Decision threshold from Monte Carlo simulations

Monte Carlo simulations that mimic the mixture under the null hypothesis of a radionuclide allows quantifying the false positive rate of this radionu-

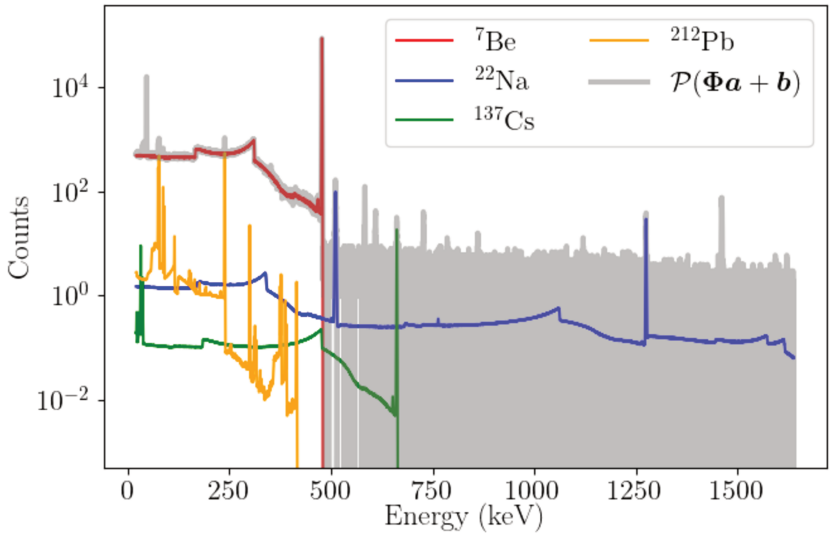

Figure 5.1 – Spectral unmixing model used to illustrate the evaluation of the characteristic limits. The simulated measurements (gray) are composed of the above 10 radionuclides, while individual spectra of ^{7}Be,^{22}Na,^{137}Cs,^{212}Pb will be evaluated.

clide, thus the decision threshold. For each radionuclide, 1000 simulations are performed with this radionuclide set to zero and other radionuclides set to their actual levels. The Poisson-based spectral unmixing algorithm is subsequently applied to estimate mixing weights from these simulated spectra. The distribution of the estimated mixing weight of this radionuclide enables to derive the decision threshold level based on some desired false positive rate.

Confidence interval from Monte Carlo simulations

In practice, and assuming that some estimate of the mixing weights have a limited estimation bias or error, a confidence interval with respect to a given probability γ and for individual radionuclides can be derived by performing Monte-Carlo simulations. More precisely, we first perform 1000 Monte Carlo simulations that mimic the actual mixing scenario of radionuclides. Next, the Poisson-based spectral unmixing algorithm is applied to estimate mixing weights from these simulated spectra. Finally, the confidence interval of radionuclides can be derived from the distribution of their estimated mixing weights.

Illustration of Monte Carlo based assessment of characteristic limits

The distribution of the above Monte Carlo simulations are graphically presented in Figure 5.2 for the 4 radionuclides we are interested in, which demonstrates the distribution of :

- First column of each sub-figure: the mixing weights estimated from 1000 Monte Carlo simulations carried out under null hypothesis of each radionuclide (*i.e.*, the radionuclide is not present in the simulations).
- Second column of each sub-figure: the mixing weights estimated from 1000 Monte Carlo simulations performed with actual mixing weights.

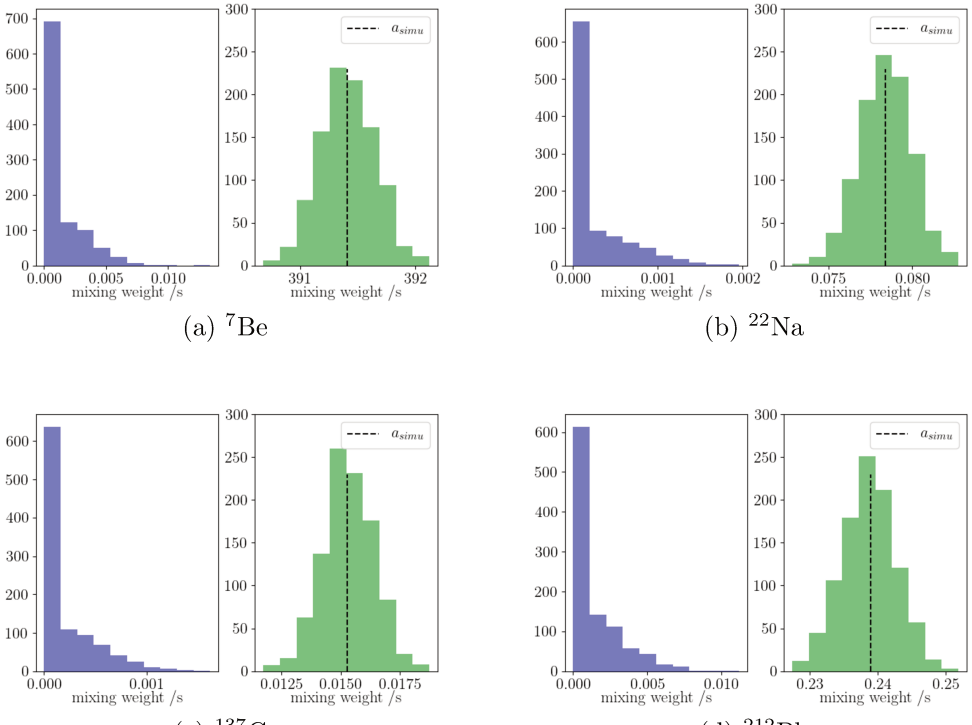

(a) ^{7}Be (b) ^{22}Na

(c) ^{137}Cs (d) ^{212}Pb

Figure 5.2 – Distribution of estimated mixing weights obtained with: i), $a_{simu} = 0$ (*i.e.*, null hypothesis) (blue), ii) a_{simu} = actual level (green), while the true value is shown in dotted line.

Statistically, these two distributions demonstrated in Figure 5.2 give us an idea about the statistical significance of the estimated results. More precisely,

the first ones obtained with simulations under the null hypothesis can be used to quantify the significance of the radionuclide's presence, which allows computing a decision threshold with respect to some false positive rate from the according percentile of the distribution. The second ones obtained with the true mixture allows computing a confidence interval from the according percentiles of the distribution that contains the true value.

In practice, Monte Carlo simulations are seldom used to analyze gamma-ray spectra in routine analysis procedures. The main drawback is their massive computational cost since Monte Carlo simulations are needed for each new spectrum to be analyzed. In the next sections, we focus on computationally cheaper and yet precise alternatives to derive the characteristic limits without resorting to Monte-Carlo simulations.

5.3 Quantifying the decision threshold

5.3.1 Decision threshold in peak-based analysis

In gamma-ray spectrum analysis, the decision threshold is usually derived from some statistical test based on the measured spectrum. This amounts to evaluating how much the estimated quantity associated with a radionuclide's activity departs from the background (*i.e.*, other contributions composed in the measured spectrum) and is therefore statistically consistent or not with this background.

In the peak-based analysis, the activity is associated with the net counts (see details in Chapter 2). Recall that it is the total number of counts measured in a given ROI, which further corrected by the average number of counts of the background:

$$N_n = N_g - N_0 \tag{5.3}$$

where N_n is the net counts number associated to the activity, N_g is the observed gross number of counts and N_0 is the number of background counts. Recall the definition of DT in Section 5.1, the DT level of the measurand (*i.e.*, net counts number) is derived from:

$$\alpha = \mathcal{P}(N_n \geq DT | \tilde{N}_n = 0) \tag{5.4}$$

where α and $\tilde{N}_n$ stands for the desired FPR and the true value of the net number of counts respectively. The estimated number of N_g and N_0, noted $\hat{N}_g$ and $\hat{N}_0$ respectively. In practice, the DT is derived from some statistical test of the quantity $\hat{N}_g - \hat{N}_0$ under the hypothesis of $\tilde{N}_n = 0$, which has:

- mean value equal to zero.

- variance according to $2\hat{N}_0$, since both of N_g and N_0 follow the Poisson statistic thus their mean value are equal to their variance, and $N_g = N_0$ under the hypothesis of $\tilde{N}_n = 0$.

5.3.2 Decision threshold in spectral unmixing analysis

The DT determination in peak-based analysis considers that the background spectrum N_0 is well estimated and provides a mean value of the distribution under the null hypothesis, from which the DT can be derived based on a desired FPR. Now, we aim to investigate the DT in the spectral unmixing approach, where the measurand associated with a radionuclide's activity is the number of counts in the full spectrum range. The DT can be derived with the same idea of statistical test based on a "background", but adapted to the full spectrum analysis.

Recall that the spectral unmixing decomposes a gamma-ray spectrum into individual spectra of radionuclides. To determine the decision threshold of a single radionuclide indexed by j in the unmixing model, we reformulate the true linear mixing model with this radionuclide and an equivalent background:

$$\boldsymbol{\Phi a} + \boldsymbol{b} \rightarrow \boldsymbol{\phi}_j a_j + \boldsymbol{m} \tag{5.5}$$

where $\boldsymbol{\phi}_j a_j$ represents the individual spectrum of the j^{th} radionuclide, while the other radionuclides and the background spectrum $\boldsymbol{b}$ compose an equivalent background:

$$\boldsymbol{m} = \sum^{l \neq j} \boldsymbol{\phi}_l a_l + \boldsymbol{b}$$

In the spectral unmixing analysis, the activity of the j^{th} radionuclide is associated to the mixing weight a_j. Recall the definition in Section 5.1, the DT level of the measurand (*i.e.*, a_j) is derived from:

$$\alpha = \mathcal{P}\left(a_j \geq DT | \tilde{a}_j = 0\right) \tag{5.6}$$

Recall that, the measured spectrum $\boldsymbol{x}$ is composed of M channels, $\forall i \in [1, ..., M]$, the observed counts in each channel of the spectrum follows a Poisson distribution with mean value: $\lambda_i = [\boldsymbol{\phi}_j a_j]_i + m_i$.

The DT can be derived from a standard hypothesis testing procedure test under the null alternative of $H_0 : \tilde{a}_j = 0$, which leads to $\lambda_i = m_i$ for $\forall i \in M$. This can be generally formulated with some statistical test T as follows:

$$\alpha = \mathcal{P}\big(T \geq T(\lambda) | \forall i, \lambda_i = m_i\big) \tag{5.7}$$

For this purpose, we propose to make use of statistical test based on different assumptions as follows:

a. Test based on the sum of observed counts: a simple statistical test to consider is based on the total number of counts, as measured by the sum of observed counts under the null hypothesis H_0. Thanks to the statistical independence of each channel, this quantity should follow a Poisson distribution with mean value $\hat{\boldsymbol{m}}$ (*i.e.*, estimated equivalent background).

$$\sum_i x_i \sim \mathcal{P}oisson\left(\sum_i \hat{m}_i\right) \tag{5.8}$$

Therefore, the DT (noted a_j^*) of the estimated activity for the j^{th} radionuclide with a given false positive rate α, can be derived from the cumulative distribution function (CDF) of the following distribution:

$$\alpha = \mathcal{P}\Big(\sum_{i\in C} x_i \geq \sum_{i\in C}[\boldsymbol{\phi}_j a_j^*]_i + \sum_{i\in C} m_i\Big) \tag{5.9}$$

where C is some set of observed channels. The total number of counts from the full spectrum is a special case where C defines all the observed channels. While it allows to account for the full information carried out by the spectrum, it however poorly distinguishes the radionuclide to be tested from the background. We rather use the pre-specified channels in a region of interest, where the equivalent background is better distinguished from the j^{th} radionuclide. (*e.g*, peak region of the radionuclide).

b. Test based on sum of weighted observed counts: In order to better distinguish between the radionuclide to be tested and the equivalent background, we further investigate statistical test derived from the sum of weighted counts in different channels written as $\sum_i w_i m_i$ with the following choice of w_i:

- Let $\boldsymbol{\Psi} = \begin{bmatrix}\boldsymbol{\phi}_j & \boldsymbol{m}\end{bmatrix}$, the least squares solution of the mixing vector of $\boldsymbol{\Psi}$ can be written as:

$$\hat{\boldsymbol{a}} \in \underset{\boldsymbol{a}}{\operatorname{argmin}} \frac{1}{2}\|\boldsymbol{x} - \boldsymbol{\Psi a}\|^2 \tag{5.10}$$

  for which the solution is $\hat{\boldsymbol{a}} = \boldsymbol{\Psi}^\dagger \boldsymbol{x}$, where $\boldsymbol{\Psi}^\dagger = (\boldsymbol{\Psi}^T\boldsymbol{\Psi})^{-1}\boldsymbol{\Psi}^T$ is the pseudo inverse matrix.

  We make use of the the component of $\boldsymbol{\Psi}^\dagger$ related to $\boldsymbol{\phi_j}$ as the weights matrix, noted as $\boldsymbol{w}_1 = \boldsymbol{\Psi}^\dagger_\phi$. As graphically illustrated in Figure 5.3, it allows projecting onto the span of $\boldsymbol{\phi}_j$ parallelly to $\boldsymbol{m}$.

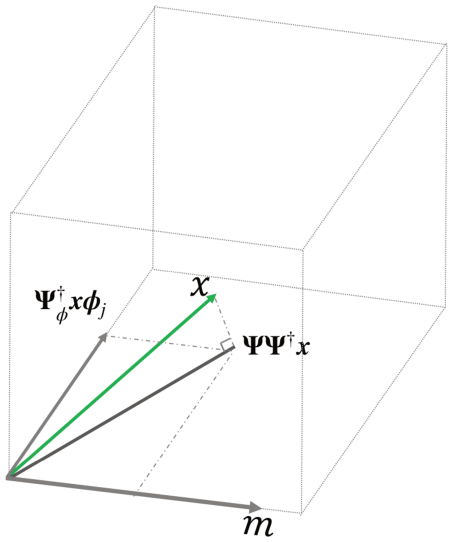

Figure 5.3 – Schema of the least squares solution of the equivalent background model.

Nevertheless, the resulting statistical test do not follow a Poisson distribution. Thankfully, since it is defined as a linear combination of a large number of observed channels, one can approximate the distribution to be Normal. The resulting statistical test with observed counts $\boldsymbol{x}$ and estimated equivalent background $\boldsymbol{m}$ will be carried out as follows:

$$\sum_i w_i x_i \sim \mathcal{N}\left(\sum_i w_i m_i, w_i^2 m_i\right) \tag{5.11}$$

while in each channel, the mean value $\mu = w_i m_i$ and variance $\sigma^2 = w_i^2 m_i$ are considered, since both the mean value and the variance of the model equal to m_i because of the Poisson statistics.

The DT of the estimated activity a_j^* can be derived from the CDF of Normal distribution:

$$\frac{\alpha}{2} = \mathcal{P}\Big(\sum_i w_i x_i \geq \sum_i w_i [\boldsymbol{\phi}_j a_j^*]_i + \sum_i w_i m_i\Big) \tag{5.12}$$

- the weighted background statistical test is further studied with $\boldsymbol{w}_2 = \boldsymbol{\Psi}_\phi^\dagger$ with:

$$\boldsymbol{\Psi}^\dagger = \Big(\boldsymbol{\Psi}^T \mathrm{diag}\big(\frac{1}{\boldsymbol{\phi}_j a_j + \boldsymbol{m}}\big)\boldsymbol{\Psi}\Big)^{-1} \boldsymbol{\Psi}^T \mathrm{diag}\big(\frac{1}{\boldsymbol{\phi}_j a_j + \boldsymbol{m}}\big) \tag{5.13}$$

Next, we evaluate the above statistical tests to assess the decision threshold for HPGe and NaI spectra, while the results are compared to those carried out with Monte Carlo simulations.

5.3.3 Evaluation of the decision threshold determination

For a comparison purpose, by fixing the false positive rate to $\alpha = 2.5\%$, we calculate the DT for Poisson-based spectral unmixing with the following approaches:

- For each radionuclide, the accurate DT level quantified with respect to $1 - \alpha$ percentile of the distribution of estimated value from Monte Carlo simulations under the null hypothesis of this radionuclide.
- the decision threshold assessment with different statistical tests for each Monte Carlo simulation. The comparisons are carried out for:
  - the Poisson statistical test based on the sum of counts in peak region. This is used only for HPGe measurements since using the peak regions to analyze NaI measurements is not interesting due to the correlations of spectra, for which it is better to take into account the full spectrum information.
  - the Gaussian statistical test based on two choices of weighted sum of counts, noted $\boldsymbol{w}_1$ and $\boldsymbol{w}_2$ respectively.

The evaluation are carried out for:

- Experiments on the described mixing scenario (see Figure 5.1) of an HPGe measurement, while the peak region, noted ROI, used are: ^{7}Be at 477 keV, ^{22}Na at 1274 keV, ^{137}Cs at 661 keV and ^{212}Pb at 238 keV.
- Simulations of NaI gamma-ray spectra measurements. By considering the spectral signatures used in [Paradis et al., 2020], simulations are performed with ^{60}Co, ^{134}Cs, ^{137}Cs, ^{152}Eu with a background spectrum. As shown in Figure 5.4, 1000 simulations are performed for the mixture with respect to number of counts shown in Table 5.2.

Radionuclide	^{60}Co	^{134}Cs	^{137}Cs	^{152}Eu	background
Number of counts	1500	500	1500	2500	4000

Table 5.2 – Number of counts of NaI simulations.

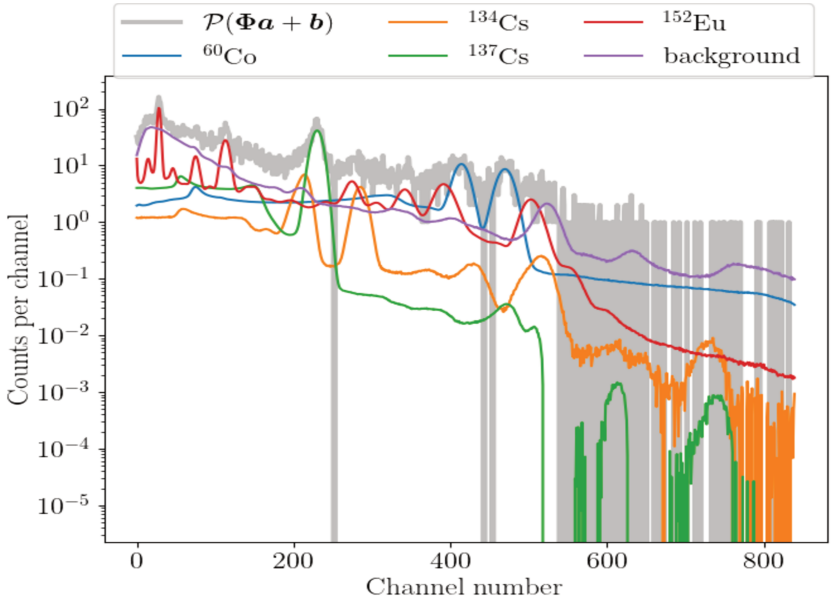

Figure 5.4 – Spectral unmixing model of simulations of NaI measurements.

Results

For HPGe spectra, the different statistical tests are compared in Figure 5.5, 5.6, 5.7 and 5.8. Figure 5.9, 5.10, and 5.11, and 5.12 for NaI spectra respectively. The results report the distribution of:

- Poisson test based on region of interest (ROI) (green) of $\boldsymbol{x}$.
- Gaussian test based on sum of weighted counts carried out by $\boldsymbol{w}_1\boldsymbol{x}$ (blue) and $\boldsymbol{w}_2\boldsymbol{x}$ (orange).
- For a comparison purpose, the accurate DT level calculated from Monte Carlo (*i.e.*, $1-\alpha$ percentile of the distribution under the null hypothesis) is displayed with a dotted line (red).

From these results, we can draw the following conclusions:

- Firstly, compared to the Gaussian statistical test based on the sum of weighted counts, the Poisson statistical test based on the sum of the counts in the ROI is less efficient to derive the DT. Since the peaks are not well distinguished from the continua.
- For HPGe measurement, for ^{22}Na, ^{137}Cs and ^{212}Pb, the Gaussian statistical test of weighted counts with w_2 derives similar DT levels comparing to the actual $1-\alpha$ percentile of the distribution (*i.e.*, accurate

DT level), which is better than the choice of w_1. This is not valid for ^{7}Be due to the fact that ^{7}Be is predominant in the measured spectrum, while its equivalent background is poorly estimated. However, the determination of accurate DT level for low-level radionuclides is more important for the decision making purpose; in such case, the dominant spectral contribution such as ^{7}Be can provide a better estimation of the equivalent background thus more accurate DT determination for low-level radionuclides.

- When we further focus on the results of NaI measurements, the choice of using w_2 is shown to be more consistent than w_1; it allows better distinguishing a radionuclide from its equivalent background when the spectra are overlapped in the whole energy range.

It should be noted that, the methods introduced in this section for the decision threshold determination are evaluated with simulations of realistic HPGe detector performed aerosol measurements. The validated statistical test based on the sum of weighted counts (with the choice of $\boldsymbol{w}_2$) of the equivalent background can be therefore used in the quantitative analysis of experimental measurements with the Poisson-based spectral unmixing, which will be investigated in Chapter 6.

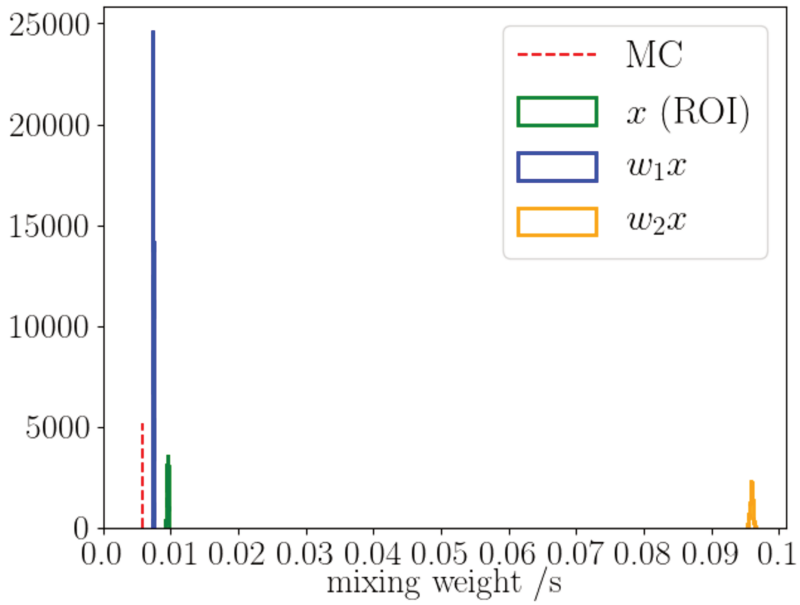

Figure 5.5 – DT assessment for HPGe measurements: ^{7}Be

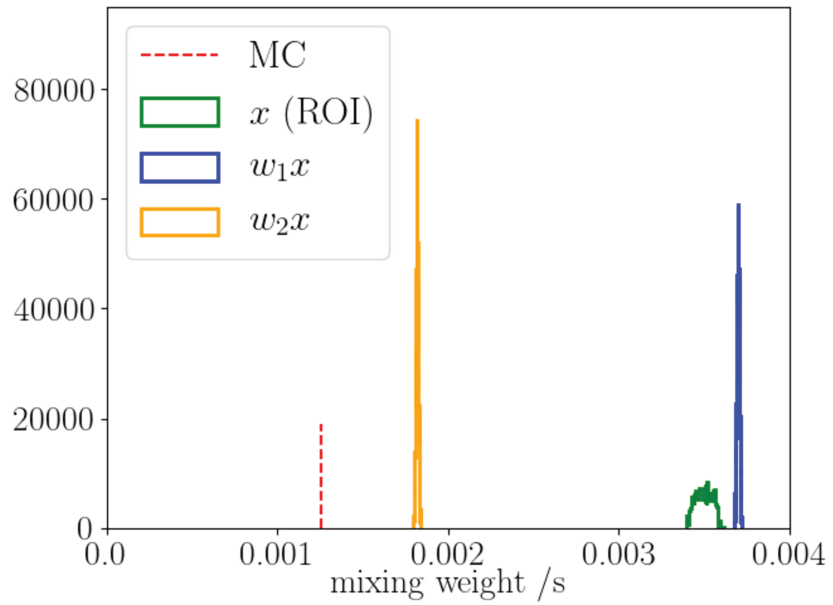

Figure 5.6 – DT assessment for HPGe measurements: ^{22}Na

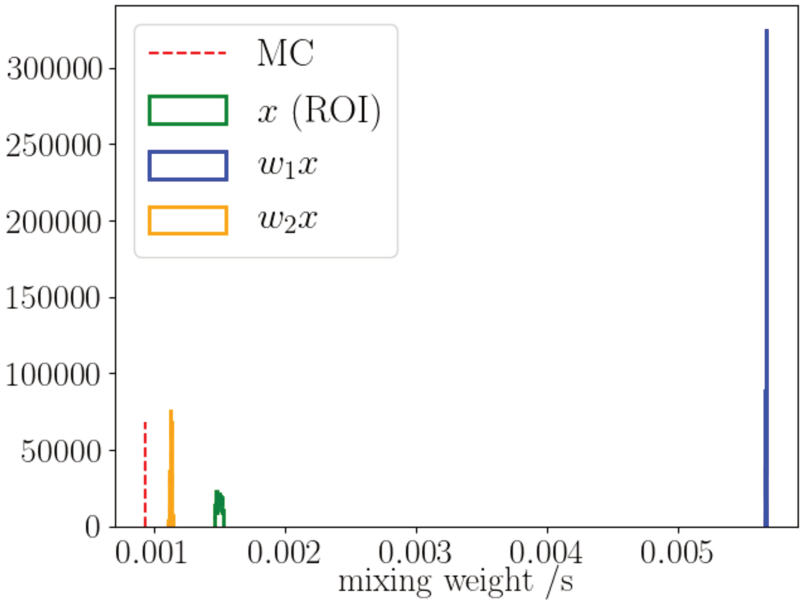

Figure 5.7 – DT assessment for HPGe measurements: ^{137}Cs

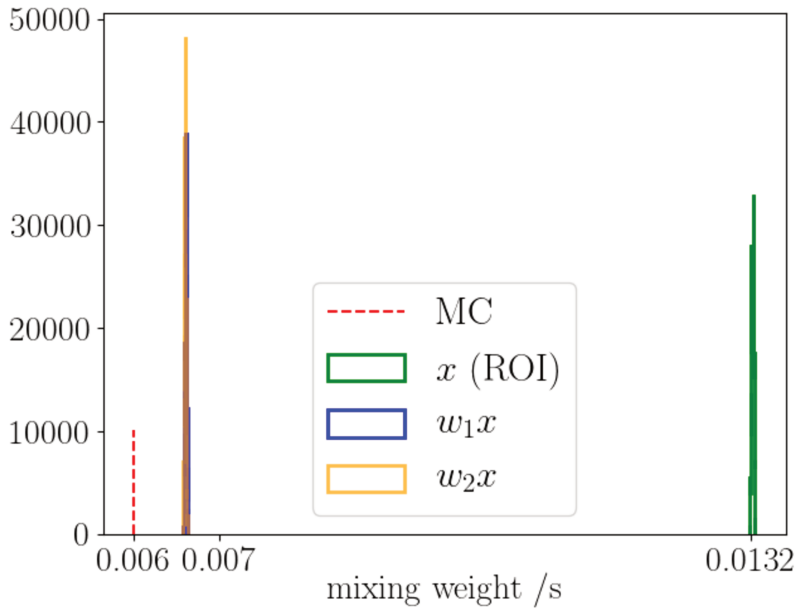

Figure 5.8 – DT assessment for HPGe measurements: ^{212}Pb

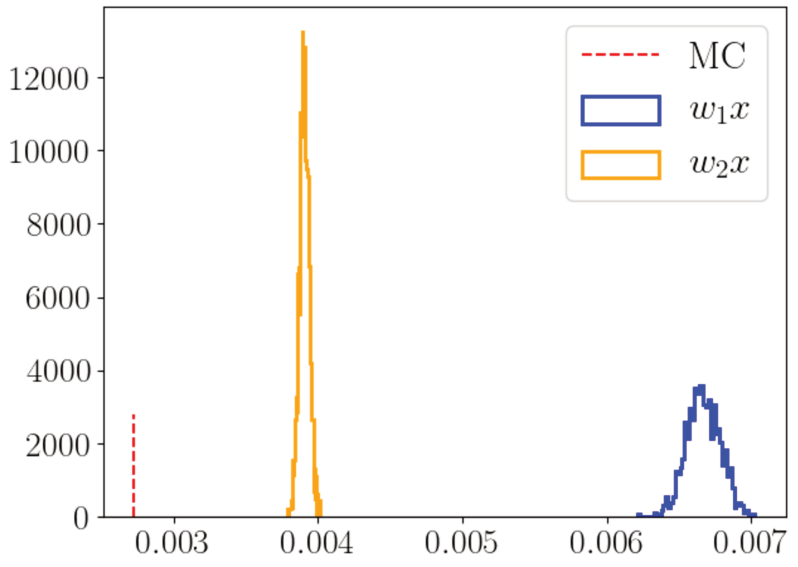

Figure 5.9 – DT assessment for NaI measurements: ^{60}Co

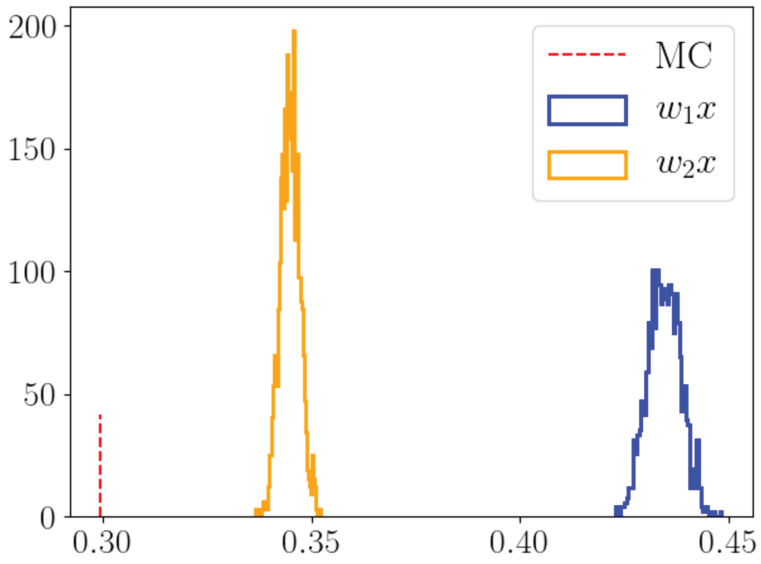

Figure 5.10 – DT assessment for NaI measurements: ^{134}Cs

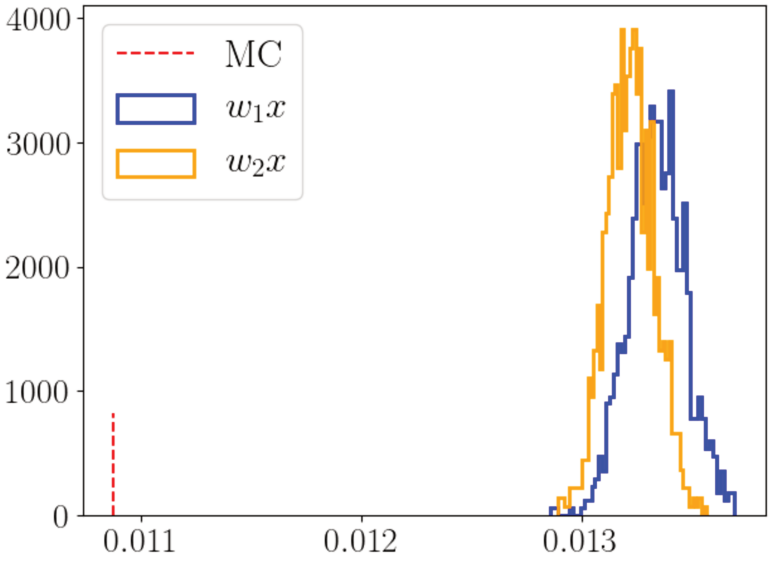

Figure 5.11 – DT assessment for NaI measurements: ^{137}Cs

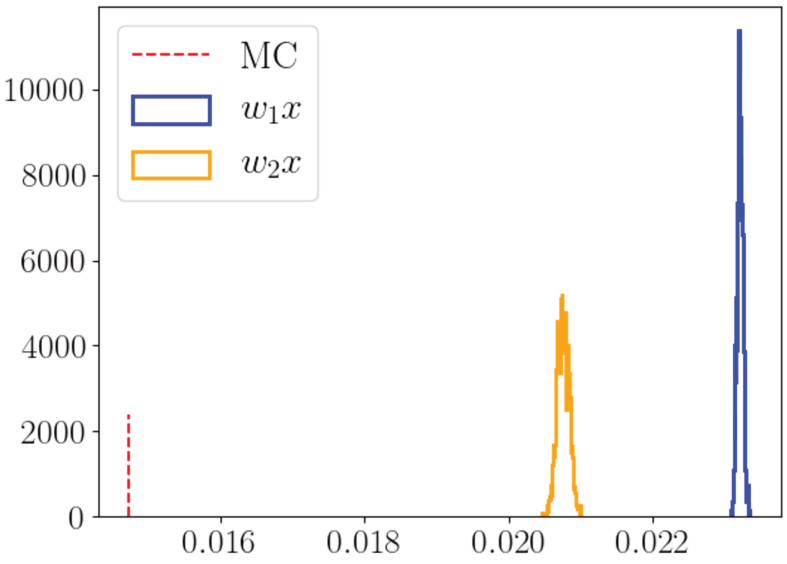

Figure 5.12 – DT assessment for NaI measurements: ^{152}Eu

5.4 Confidence interval

The statistical uncertainty of the estimation of a parameter is twofold: the estimation bias and an interval of values that contains the true value of the parameter. In the spectral unmixing approach, the assessment of uncertainties can be carried out from Monte Carlo simulations that mimic the actual mixture of radionuclides as presented in Section 5.2. The distribution of estimated values provides both the estimation bias and the confidence interval (see Figure 5.2). However, this requires a massive amount of simulations, making this approach hard to implement in practice. Nevertheless, the Poisson-based spectral unmixing is shown to provide accurate activity estimations; we can only focus on determining a confidence interval from the estimated mixing weights.

5.4.1 Fisher information to compute confidence intervals

For the observed variable x distributed as $f\left(x|\theta\right)$, the maximum likelihood estimator (MLE) can be approximated with a Gaussian distribution:

$$\mathcal{N}\left(\theta, I(\theta)^{-1}\right) \tag{5.14}$$

where $I(\theta)$ is the Fisher information ([Fisher, 1956]) defined as:

$$I(\theta) = \mathbb{E}_\theta \left[\frac{\partial^2 \log f(x|\theta)}{\partial \theta^2} \right] \tag{5.15}$$

The estimation standard error can be obtained by replacing the unknown true value θ by the estimated value $\hat{\theta}$.

In our activity estimation problem, the investigated Poisson-based spectral unmixing provides a maximum likelihood estimate of the mixing weights, noted $\hat{\boldsymbol{a}}$. According to the Poisson likelihood, the Fisher information matrix can be written as:

$$I(\hat{\boldsymbol{a}}) = \boldsymbol{\Phi}^T \mathrm{diag}\big(\boldsymbol{x} \oslash (\boldsymbol{\Phi}\hat{\boldsymbol{a}} + \boldsymbol{b})^2\big)\boldsymbol{\Phi} \tag{5.16}$$

We propose to assess the confidence interval of the estimated mixing weights $\hat{\boldsymbol{a}}$ by the diagonal elements of $\sqrt{I(\hat{\boldsymbol{a}})^{-1}}$, which approximates the standard deviation of the distribution.

5.4.2 Evaluation of confidence interval in spectral unmixing

In this paragraph, the confidence interval assessment with Fisher information matrix is evaluated with simulations of HPGe and NaI measurements described in the previous section. More precisely, we calculate the standard deviation from the Fisher information matrix and evaluate the results with Monte Carlo simulations.

Firstly, we make use of the Q-Q (quantile-quantile) plots, which compares the distribution of estimated activities of Monte Carlo simulations to the distribution generated from the standard deviation carried out with Fisher information. The aim is to i), test the normality of the estimator, which allows validating the confidence interval with a standard uncertainty in terms of Normal distribution. ii), compare the distribution to those obtained with Fisher information.

More precisely, for each radionuclide, we show the Q-Q plot for two data samples noted A_1 and A_2:

- A_1 for estimated activity values of Monte Carlo simulations.
- A_2 for Normal distribution generated from the Fisher information of the estimation:

  $$\mathcal{N}\left(a_0, \sigma_f^2\right)$$

  where a_0 is the expected mixing weight of the radionuclide and σ_f is the standard uncertainty calculated from the Fisher information matrix.

For each value a in a sample (A_1 and A_2), quantiles are calculated with:

$$\boldsymbol{q} = \frac{\boldsymbol{a} - \mu}{\sigma} \tag{5.17}$$

where μ and σ are the mean value and the standard deviation of the given sample.

The Q-Q plots shown in Figure 5.13 and Figure 5.14 for the HPGe measurement and the NaI measurement, respectively, display the quantiles of A_2 (Fisher quantiles) as a function of A_1 (Estimation distribution quantiles).

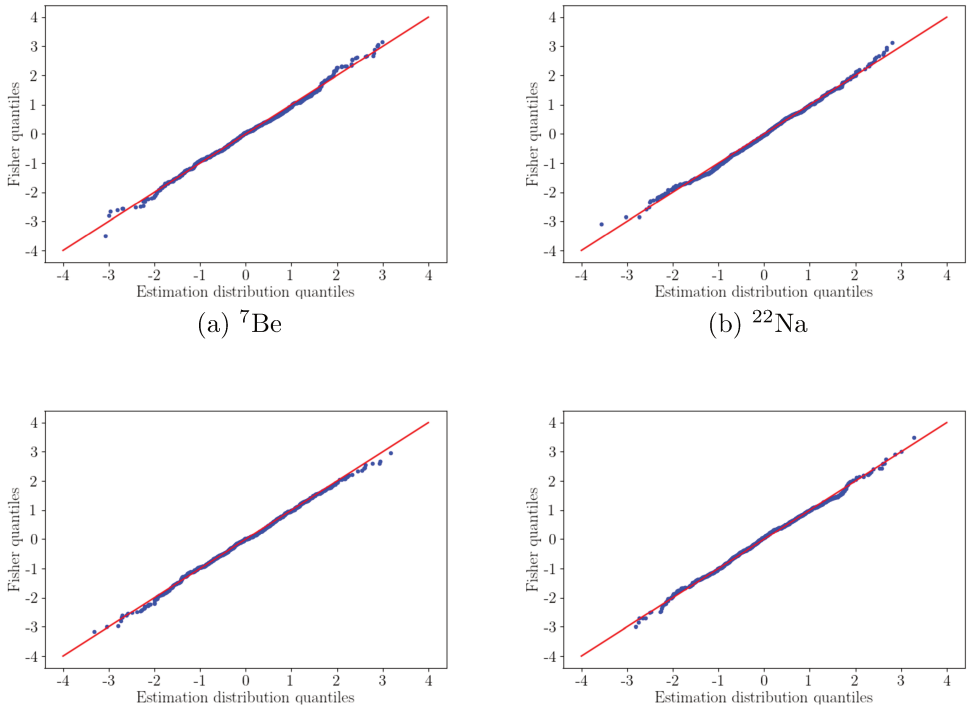

(a) ^{7}Be (b) ^{22}Na

(c) ^{137}Cs (d) ^{212}Pb

Figure 5.13 – Evaluation for the HPGe simulation: the Q-Q plots for Fisher quantiles versus estimation distribution quantiles for radionuclides.(blue). The theoretical Q-Q plots are shown in red.

Firstly, the results show the normality of activity estimation of Monte Carlo simulations with the straight line of the Q-Q plots and absolute values from 0 to 3. This confirms that the confidence interval of the estimation can be carried out with an approximation of the Normal distribution. Secondly, the Normal distribution generated with spectral unmixing (Maximum likelihood estimation) and Fisher information matrix provides similar confidence

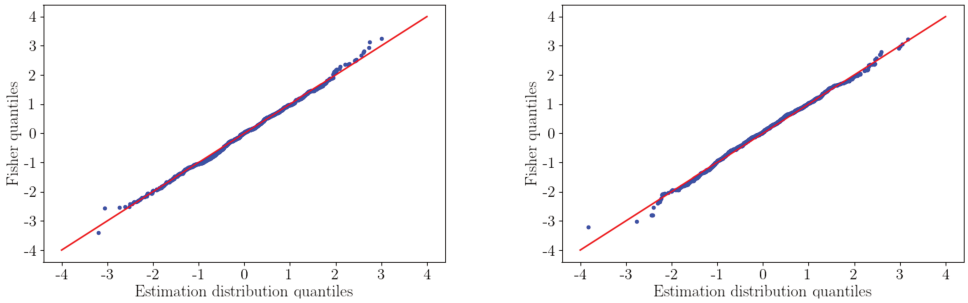

(a) ^{60}Co (b) ^{134}Cs

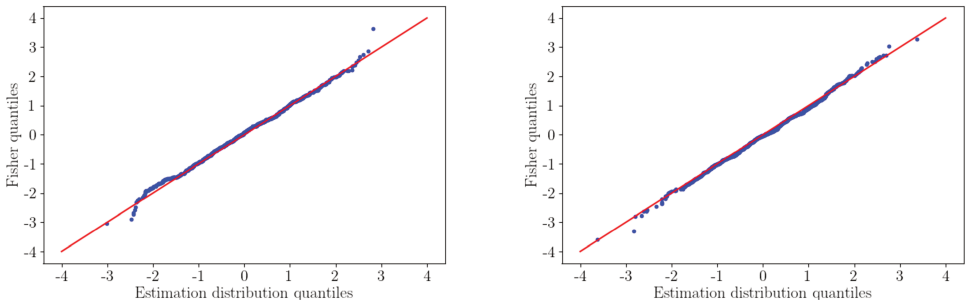

(c) ^{137}Cs (d) ^{152}Eu

Figure 5.14 – Evaluation for the NaI simulation: the Q-Q plots for Fisher quantiles versus estimation distribution quantiles for radionuclides.(blue). The theoretical Q-Q plots are shown in red.

intervals comparing to the real Monte Carlo distribution. To further valid this conclusion, we calculate the percentage of the values estimated from Monte Carlo simulations within the interval of:

$a_0 \pm \sigma_f$, $a_0 \pm 2\sigma_f$ and $a_0 \pm 3\sigma_f$,

where a_0, σ_f stand for the expected mixing weight (*i.e.*, simulated value) and standard error determined by the Fisher matrix. These percentage values are expected to be 68.27 %, 95.45 % and 99.73 % for normal distribution. The results are shown in Table 5.3 and Table 5.4 for HPGe and NaI measurements respectively.

5.5 Discussion

The determination of characteristic limits of the Poisson-based spectral unmixing are investigated in this chapter. The decision threshold and the

	^{7}Be	^{22}Na	^{137}Cs	^{212}Pb
percentage within $a_0 \pm \sigma_f$	68.0	66.1	68.6	68.4
percentage within $a_0 \pm 2\sigma_f$	96.4	93.9	95.7	95.0
percentage within $a_0 \pm 3\sigma_f$	99.9	99.8	99.8	99.9

Table 5.3 – Standard deviation from Fisher information matrix comparing to Monte Carlo simulations (HPGe measurements).

	^{60}Co	^{134}Cs	^{137}Cs	^{152}Eu
percentage within $a_0 \pm \sigma_f$	68.1	66.0	67.5	66.2
percentage within $a_0 \pm 2\sigma_f$	95.3	95.0	94.0	95.5
percentage within $a_0 \pm 3\sigma_f$	99.7	99.5	99.9	99.8

Table 5.4 – Standard deviation from Fisher information matrix comparing to Monte Carlo simulations (NaI measurements).

confidence interval are evaluated and validated for simulations of HPGe and NaI measurements. It should be noted that the simulations of HPGe measurement mimic realistic activities of aerosol measurements; therefore, the decision making with the proposed decision threshold and the confidence interval (*i.e.*, statistical uncertainty) assessment with the Fisher information matrix can be used in the quantitative analysis of HPGe gamma-ray spectra measurements, this will be presented in Chapter 6.

CHAPTER 6

Analysis of HPGe gamma-ray spectra measurements

Contents

6.1 Challenges of calibrations in gamma-ray spectrum analysis 102

6.1.1 Calibrations in peak based analysis 103

6.1.2 Towards calibrations for spectral unmixing 105

6.2 Efficiency calibration and resolution calibration in simulation process 106

6.2.1 Efficiency calibration 107

6.2.2 Resolution calibration in spectral unmixing 108

6.3 Complexity of the spectral signatures 109

6.4 Re-calibration of energy in spectral unmixing . 110

6.5 Validation with the standard source analysis . . 116

6.6 Experiments on aerosol measurements 118

6.6.1 Uncertainty budget of the aerosol measurements . 118

6.6.2 Re-analysis of aerosol measurements 120

6.7 Conclusion 122

In this chapter, we investigate the application of spectral unmixing methods to analyze spectra of HPGe gamma-ray measurements. We focus on the evaluation and validation of the spectral analysis pipeline for gamma-ray measurements performed with a detection system (*i.e.*, detector and source

geometry) used in the laboratory, which can be virtually applied to other detection systems.

Applying the spectral unmixing to real measurements is not straightforward as the data need to be calibrated for a precise analysis. The general questions of calibrations in gamma-ray spectrum analysis are described in Section 6.1; we describe how these calibration tasks are carried out in standard peak based analysis and propose the calibration procedures in the spectral unmixing approach. Next, three calibrations steps are investigated and evaluated with a standard multi-gamma source of known activities:

- The calibrations required in the simulation process of spectral signatures are presented in Section 6.2. In this framework, the efficiency and the resolution are adjusted to mimic the response of the detection system.
- In Section 6.3, we discuss the complexity of the spectral signatures, which amounts to adding spectral contributions due to the lead shielding system into the spectral signatures.
- Section 6.4 presents the energy calibration for the Poisson based spectral unmixing algorithm.

The calibrations are subsequently validated with the spectrum analysis of the standard source in Section 6.5. Next, the proposed quantitative pipeline is applied to analyze past measurements of environmental samples (aerosol filters) in Section 6.6, where the results are compared to those obtained with the standard method. Finally, conclusions and perspectives can be found in Section 6.7.

6.1 Challenges of calibrations in gamma-ray spectrum analysis

The qualitative analysis in gamma-ray spectrometry consists of: i), the identification of radionuclides in the sample. ii), the quantification of each radionuclide by determining the activity in becquerel (Bq), as well as its characteristic limits and the uncertainties of the measurement.

In practice, the accurate quantitative analysis in gamma-ray spectrometry strongly depends on the proper calibration of the measurement instrument (*i.e.*, the detector and the sample geometry), which relates the detected counts in a measured spectrum to the activity of radionuclides. The main calibration tasks are: energy calibration for identifying radionuclides, efficiency calibration and resolution calibration for the quantification of radionuclides.

In this section, we detail these calibrations and how they are performed in standard peak based analysis. The calibrations in spectral unmixing analysis need to be performed differently; they are introduced at the end of this section.

6.1.1 Calibrations in peak based analysis

Energy calibration

We would like to recall that a gamma-ray spectrum measurement provides the energy response of emitted photons (gamma-ray or X-ray) with multi-channel analyzer (MCA), such a spectrum is the histogram of detected events as a function of the voltage ranges (*i.e.*, channel number). More precisely, the number of channels in MCA used for gamma-ray spectrometry is fixed: 1024 channels (*i.e.*, NaI measurements [Paradis et al., 2020]) up to 16384 channels (*i.e.*, HPGe measurements used in the laboratory). Referring to Chapter 2, the MCA collects pulses in all voltage ranges (depending on the deposited energies), noted $0 - V_{max}$, while each pulse height increments the count in a corresponding channel. For instance, when V_{max} takes 12 V and the number of channels is set to 16384, the number of counts of 5 V is according to channel 8192. The radionuclides are characterized by energies, the energy calibration is thus needed to identify radionuclides, which allows to relate the channel number to the corresponding energy:

$$E = f\left(N_{Ch}\right) \tag{6.1}$$

where N_{Ch} and E are the channel number and the corresponding energy. As shown in Figure 6.1, the energy calibration is performed by localizing peaks of known energies, which allows fitting the calibration function introduced in Eq.(6.1).

Efficiency calibration

Efficiency calibration defines a function that relates the number of observed photons and the disintegration rate. In peak based analysis, the detection efficiency of full energy peak is defined as:

$$\epsilon = \frac{N_p}{N_s} \tag{6.2}$$

As illustrated in Figure 6.2, it relates the number of counts in the full energy energy peak, noted N_p, and the number of photons emitted by the source for this energy, noted N_s, with $N_s = A \times I \times t$ (A: activity, I: emission

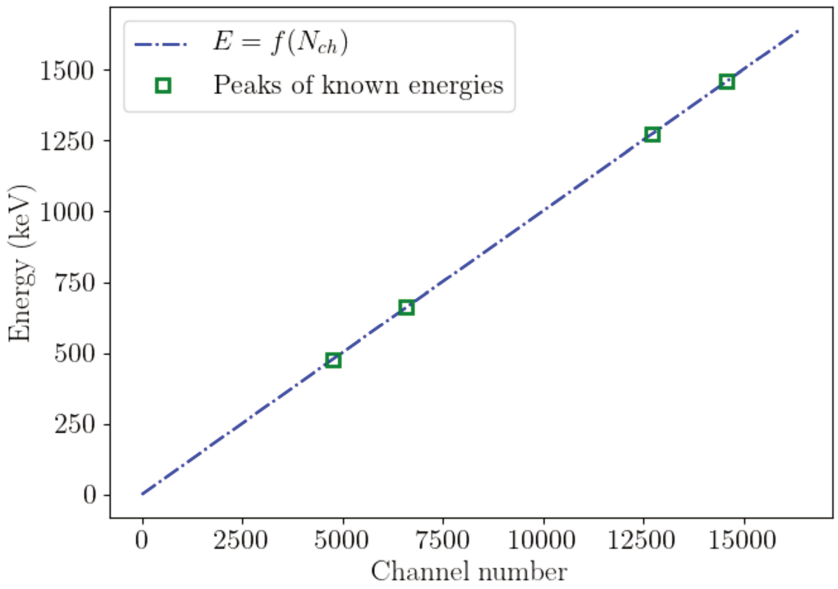

Figure 6.1 – Energy calibration in gamma-ray spectrum analysis.

intensity, t: counting time). The efficiency calibration consists in describing a function of ϵ as a function of energy. It is conventionally performed by measuring multi-gamma standard sources of known activities (see [Gilmore, 2008] for more details).

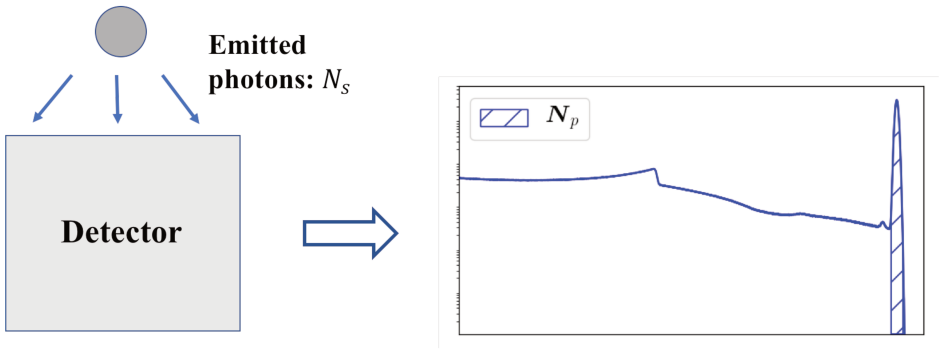

Figure 6.2 – Full energy peak efficiency model.

Resolution calibration

The resolution calibration aims to describe the shape of energy peaks as a function of energy, which is usually performed by fitting an empirical

function to describe the peak shape versus the corresponding energy:

$$FWHM = a + b\sqrt{(E + cE^2)} \tag{6.3}$$

where E is the peak energy and $FWHM$ represents the full width at half maximum of the peak.

6.1.2 Towards calibrations for spectral unmixing

In the spectral unmixing setting, the activities of radionuclides are proportional to the estimated mixing weights $\hat{\boldsymbol{a}}$ in the mixing model: $\boldsymbol{\Phi}\hat{\boldsymbol{a}} + \boldsymbol{b}$. While we are concerned with measurements of environmental samples, the spectral signatures (*i.e.*, each column of $\boldsymbol{\Phi}$) need to be simulated, since the radionuclides contained in environmental samples are rarely present in standard sources. To this end, we make use of simulated spectral signatures based on the MCNP particle transport code [Briesmeister, 2000], which is used to perform gamma-ray spectra simulations throughout this thesis. The experiments in this thesis use two versions of the MCNP code (see Appendix C for details of the simulation code).

- MCNPX (MCNP eXtended) [Pelowitz, 2011] for the gamma-ray spectrum simulation of source that emits photons at specific energies.
- MCNP-CP (A Correlated Particle Radiation Source Extension of a General Purpose Monte Carlo N-Particle Transport Code) [Berlizov, 2006] for the gamma-ray spectrum simulation of radionuclides, which simulates the physics of nuclear decay and the subsequent emissions.

Quantitative analysis with simulated spectral signatures

The MCNP simulates gamma-ray spectrum and finally normalizes the spectrum by the number of source-particle histories run in the simulation process. Accordingly, a simulated spectral signature corresponds to the energy response with unit particle (*i.e.* one disintegration). The estimated mixing weight $\hat{a}$ of a radionuclide is therefore the number of disintegrations. Recall that activity unit becquerel (Bq) is defined as the number of disintegrations per second. This leads to quantify the radionuclides' activity with:

$$\text{Activities (Bq)} = \frac{\hat{\boldsymbol{a}}}{t} \tag{6.4}$$

where $\hat{\boldsymbol{a}}$ is the estimated mixing weights and t is the counting time of the measurement. To validate the quantification in Eq.(6.4), the simulation

of spectral signatures $\mathbf{\Phi}$ needs to be adjusted with the aim of providing the accurate experimental features of the detection system (*i.e.* detector and source geometry).

An HPGe detection system in the laboratory is used in this work, Figure 6.3 shows the model of MCNP-CP simulation according to the actual detection system, using the detector specifications and dimensions given by the supplier (see Appendix C).

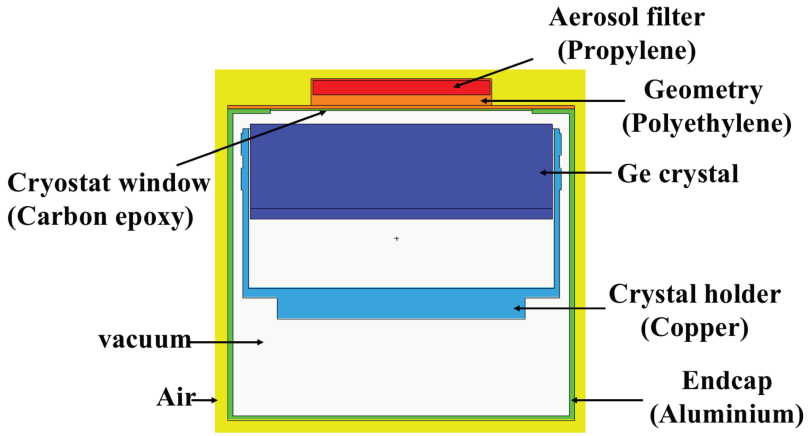

Figure 6.3 – MCNP-CP simulation model of the detection system.

The calibrations will be carried out with a multi-gamma standard source of known activities. The source dimensions are $h = 4.64$mm, $\emptyset = 52$mm and the source is contained in a 10 mL container. The gamma-ray spectrum measured for this sources is shown in Figure 6.4.

6.2 Efficiency calibration and resolution calibration in simulation process

With the aim of providing similar spectral features than the experimental responses of the detection system, the simulation configurations are set to the dimension, material features of the detection system shown in Figure 6.3. They are slightly changed to provide a better agreement of the efficiency and resolution. The final simulation input configuration can be found in Appendix C.

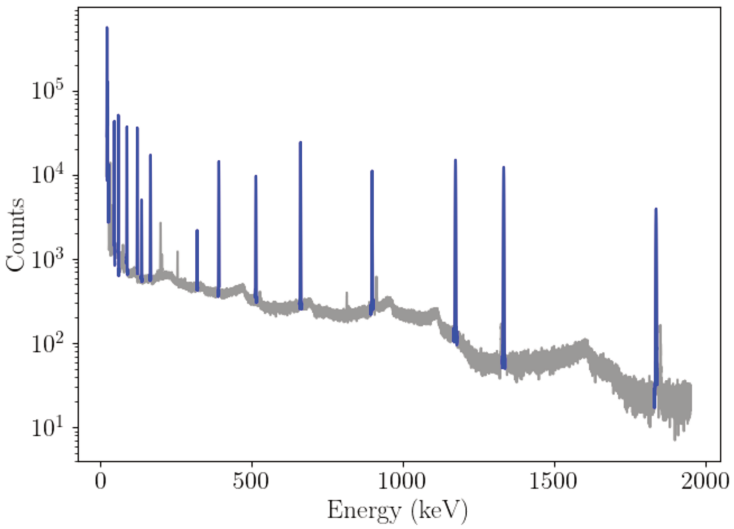

Figure 6.4 – Measured gamma-ray spectrum of a multi-gamma standard source, which contains ^{51}Cr, ^{57}Co, ^{60}Co, ^{85}Sr, ^{88}Y, ^{109}Cd, ^{113}Sn, ^{137}Cs, ^{139}Ce, ^{210}Pb, ^{241}Am. The measurement was performed with a cylindrical counting geometry ($h = 4.64$mm, $\emptyset = 52$mm) measured with an HPGe detector (60% relative efficiency). Peaks for calibrations are shown in blue.

6.2.1 Efficiency calibration

For a given radionuclide, the simulated detection response has one or several peaks and their associated continua. The calibration of total detection efficiency related to the number of counts in the full spectrum (*i.e.*, peaks and continua) can not be generated as a function of energy, since the spectral features are different for radionuclides at the same energy. Therefore, we consider the efficiency calibration of full energy peak efficiency as in peak based analysis.

More precisely, we aim to simulate energy responses that provide a good agreement of the full energy peak efficiency for each peak of the source measurement (shown in blue in Figure 6.4). Hereafter noted as efficiency. The efficiency calibration includes two steps:

- **Experimental efficiencies:** we firstly determine the experimental efficiencies of each peak. This is done by measuring the standard source with peak based analysis, the efficiency of an energy peak E is determined with:

$$\epsilon^{exp}(E) = \frac{N_p(E)}{\mathrm{A} \times I(E) \times t} \tag{6.5}$$

where N_p is the number of observed counts in this full energy peak E, A is the activity of the radionuclide that emits photons at this energy, which is known for the standard source, I is the intensity of this energy peak (*i.e.* the probability of emission of the corresponding gamma-ray for 100 disintegrations of the radionuclide) and t is the counting time of the measurement.

- **Efficiency calibration in simulation configurations:** the objective is to calibrate the simulation detection system so that simulated detection efficiencies are close to ϵ^{exp} values. In the settings of MCNP-CP, F8 tally (pulse height tally) specifies the energy distribution of pulses, which allows us to simulate the photon energy peak as a Dirac by default (see details in Appendix C).

  Recall that a radionuclide emits photons at several energy peaks. Simulations are performed individually for each radionuclide of the source. Knowing that the simulated response is normalized by the number of particles run in the simulation, the detection efficiency of a full energy peak E of the simulated detection system is:

$$\epsilon^{simu}(E) = \frac{H(E)}{I(E)} \tag{6.6}$$

  where H is the peak height of this peak and I is the intensity according to E.

The simulation configurations have been changed so as to provide better agreement of ϵ^{exp} and ϵ^{simu}, while the details can be found in Appendix C. By comparison, the full energy peak efficiency of radionuclides in the reference source, noted ϵ^{exp} and the full energy efficiency calculated with MCNP-CP simulations, noted ϵ^{simu}, the ratio $\frac{\epsilon^{simu}}{\epsilon^{exp}}$ at each peak energy are displayed in Figure 6.5.

As a result, the full energy peak efficiency ratio shows a difference within 5% for all the peaks, which will be taken into account in the uncertainty evaluation of the measurement.

6.2.2 Resolution calibration in spectral unmixing

The detection resolution is an important feature of gamma-ray measurements, for which the calibration is particularly key in the analysis of HPGe measurements since the number of counts is large in the few channels of the peaks. In the MCNP-CP input file, the resolution can be specified with the option GEB card, the parameters in the empirical model Eq. (6.3) need to be calibrated in this step.

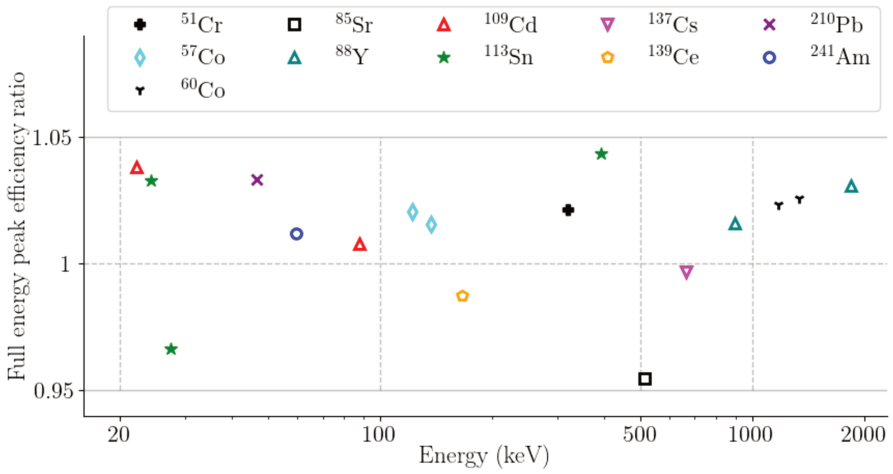

Figure 6.5 – Ratio between simulated efficiencies and the experimental efficiencies for full energy peaks, different scatters for radionuclides within the source.

More precisely, we measure the FWHM of different energy peaks, which leads to the experimental data points: $[\boldsymbol{E}, \boldsymbol{r}]$. $\boldsymbol{E}$ and $\boldsymbol{r}$ are the peaks' energies and their according $FWHM$ values, respectively. Then, we make use of these points to fit the empirical model in the form of Eq. (6.3) to find the parameters a,b and c in the model.

Figure 6.6 compares the $FWHM$ values of the measured spectrum and those calculated from the model defined in simulations. The comparison shows a good agreement of the peak width in the simulations. However, the model is less efficient to fit the peak at 21.9 keV, which is of X-ray origin. It should be noted that X-rays at low energies have larger peak width and can not be well calibrated with the empirical function Eq. (6.3). Nevertheless, the spectral unmixing is usually performed for energy higher than 40 keV for gamma-ray spectral analysis of aerosol measurements, where the simulation allows to produce good spectral responses in terms of detection resolution.

6.3 Complexity of the spectral signatures

The interaction of photons, emitted by the source or coming from the surrounding background, with the lead shielding induces the emission of X-rays of Pb; this should be considered in the dictionary of spectral signatures to unmix an HPGe gamma-ray spectrum.

Nevertheless, we are not interested in the quantification of these spectral

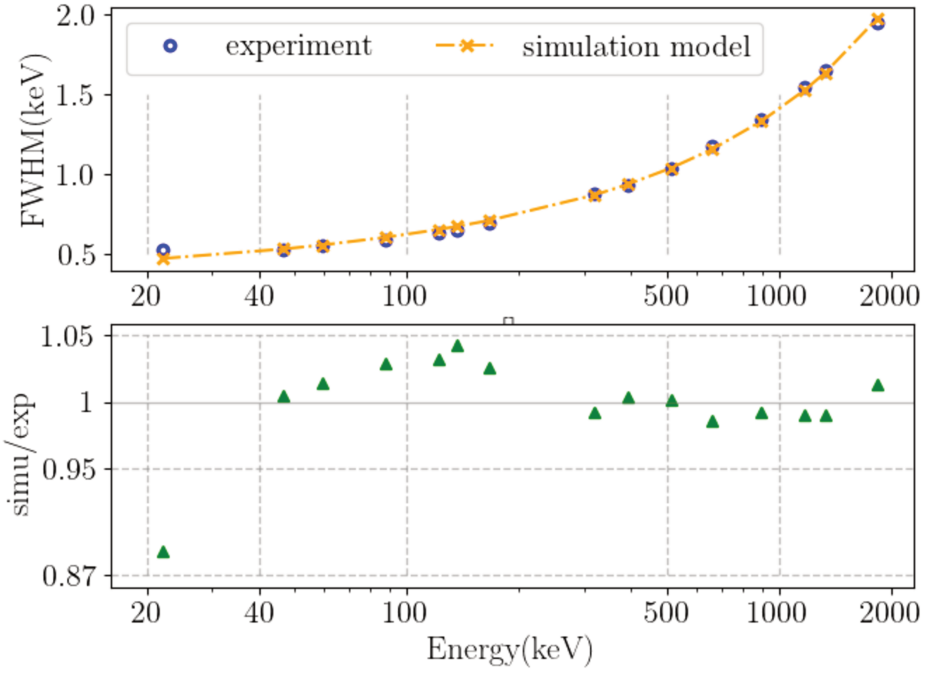

Figure 6.6 – The resolution fit versus energy. Comparison of $FWHM$ of peaks measured with the standard source and those of fitted simulation model, as well as their ratio.

components. An additional spectral signature is therefore considered, which is simulated for the mixture of X-rays of Pb at 72.8 keV (60 %), 75 keV (100 %), 84.4 keV (12 %), 84.9 keV (23 %) and 87.3 keV (8 %) with their respective emission intensity. The simulation is performed with MCNPX ((MCNP eXtended)) that simulates gamma-ray spectrum with specific energies; the simulation input file uses the configurations calibrated in Section 6.2.

6.4 Re-calibration of energy in spectral unmixing

As presented in Section 6.1, the energy calibration of a measured spectrum is performed by localizing peaks of known energies. In the spectral unmixing analysis, the re-calibration of energy on the spectral signatures is needed, since the MCNP-CP performs simulated energy response in small identical width of energy bins. In contrast, the energy bins of measured spectra are not identical.

The re-calibration poses the following practical problems:

- Simulated spectral signatures need to be interpolated to the measurement energy bins.
- Estimation bias can be caused by the shift of energy between a measured spectrum and simulated spectral signatures.

To overcome these problems, we propose to use interpolations of simulated spectral signatures in a high resolution domain corresponding to responses in smaller energy bins. It can be formulated as follows:

$$\mathbf{\Phi} = H\mathbf{\Phi}_{hr},\ \mathbf{\Phi}_{hr} = L\mathbf{\Phi} \tag{6.7}$$

where $\mathbf{\Phi}$ and $\mathbf{\Phi}_{hr}$ represent spectral signatures respectively in actual energy domain and high resolution domain. Note that E and E_{hr} are energy bins of $\mathbf{\Phi}$ and $\mathbf{\Phi}_{hr}$. The operator H and L correspond to the interpolations of $E_{hr} \rightarrow E$ and $E \rightarrow E_{hr}$ respectively.

More precisely, the energy re-calibration for the analysis of the mentioned standard source is described as follows:

Step 1: Interpolation of simulated spectral signatures In the MCNP simulation process, the energy bin scheme of the simulated spectrum is set to interval of 0.1 keV (*i.e.*, simulation of energy responses at each 0.1 keV). As illustrated in Figure 6.7, simulated spectral signatures $\mathbf{\Phi}_{simu}$ are firstly interpolated into high resolution energy bins (see illustration in Figure 6.7-a), with 10 energy bins in one channel (*i.e.*, energy responses at each 0.01 keV). Then the high resolution spectral signatures $\mathbf{\Phi}_{hr}$ are interpolated into measurement energy bins (see illustration in Figure 6.7-b), noted $\mathbf{\Phi}_r$.

Step 2: First activity estimation By using $\mathbf{\Phi}_r$, knowing that $\boldsymbol{x}$ (measured spectrum) and $\boldsymbol{b}$ (background). The spectral unmixing provides a first estimation of activities, which is denoted as $\hat{\boldsymbol{a}}_r$. The energy shift is illustrated in Figure 6.8 for a single peak.

Step 3: Correction of the energy shift for peaks of known energies The energy shift present in the first estimation for one of the energy peaks is illustrated in Figure 6.8, we aim to fit an energy shift correction function from k peaks, noted $[e_0, ...e_k]$. In such context, to determine the energy shift of each peak, we define a maximum number of shift step in the high resolution domain, which is fixed to $N_{max} = 15$ (*i.e.*, shift the spectra to left or right with maximum 15 energy bins in the high resolution domain, which is according to 0.15 keV in our simulated response). The energy shift of a peak can be therefore obtained with the shift step that minimizes the estimation residual. Details are given in Algorithm 7.

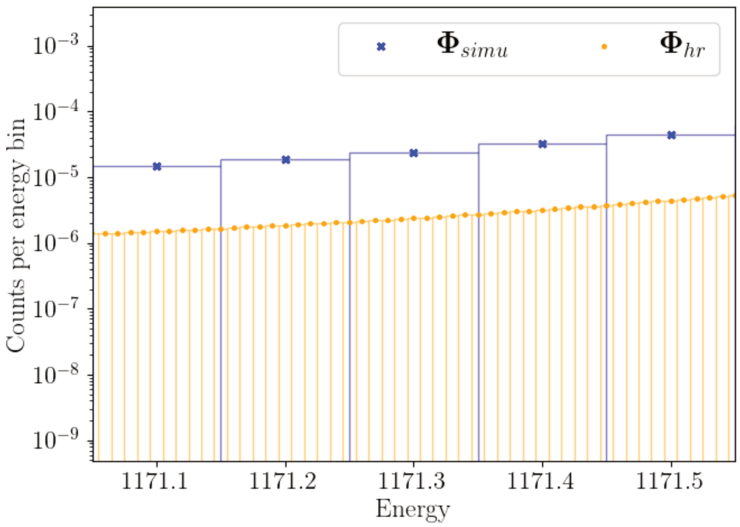

(a) $\mathbf{\Phi}_{hr} = L\mathbf{\Phi}_{simu}$

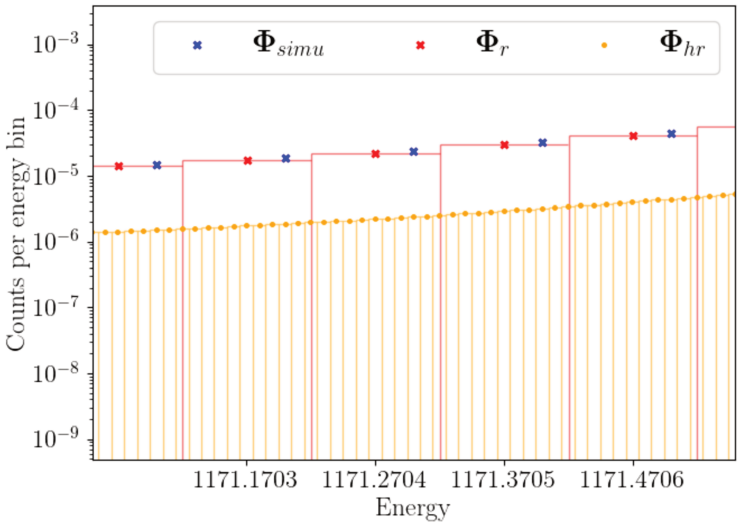

(b) $\mathbf{\Phi}_{r} = H\mathbf{\Phi}_{hr}$

Figure 6.7 – Illustration of energy bins at which to evaluate the interpolated values. (a), First interpolation: MCNP-CP simulated spectral signatures (blue) → spectral signatures at high resolution domain(orange), (b) Second interpolation: spectral signatures at high resolution → spectral signatures at energy bins of the measurement(red).

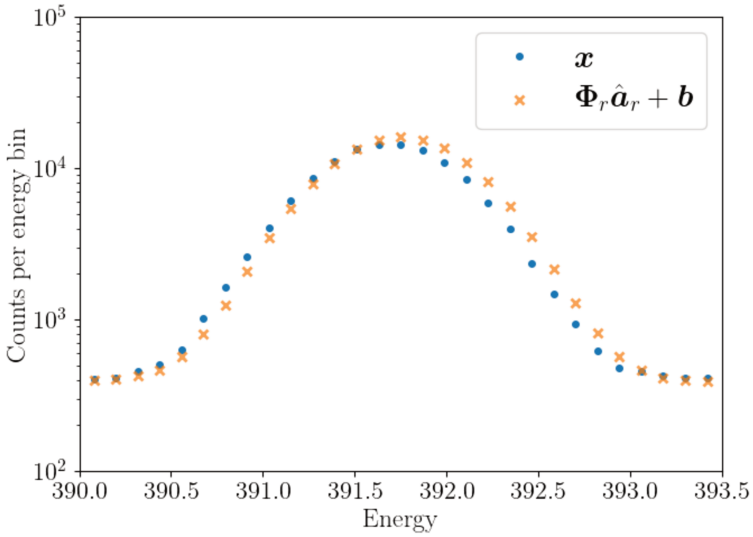

Figure 6.8 – Energy shift of the spectral unmixing compared to the measured spectrum, where $\boldsymbol{x}$ is the measured spectrum and $\boldsymbol{\Phi}_r\hat{\boldsymbol{a}}_r + \boldsymbol{b}$ is the estimated model with step 2.

Algorithm 7 Energy shift determination for the i^{th} peak

for $-N_{max} < n < N_{max}$ **do**

shift n step for $\boldsymbol{\Phi}_{hr}$, we obtain $\boldsymbol{\Phi}_{hr}^{'}$

calculate the quadratic residual:

$$r = \sum_{\text{channels in the } i^{th}\text{peak}} \|\boldsymbol{x} - \boldsymbol{b} - H\boldsymbol{\Phi}_{hr}^{'}\hat{\boldsymbol{a}}_r\|$$

end for

- Select the shift step n that minimizes the residual r
- The energy shift $\Delta_e^i = n\delta_e$, ($\delta_e = 0.01$ keV is the energy bin in high resolution domain in this experiment)

Step 4: Energy correction function fitting Once the energy shift of the peaks have been determined in step 3, we can perform the energy correction by fitting a 3 degree polynomial function of the peaks energies. This re-calibration procedure is an empirical choice for HPGe measurements.

It is of interest to extract more information from the peaks that are better distinguished from other spectral contributions. Therefore, we propose to

re-calibrate the spectral signatures' energy by solving the following weighted least squares problem that aims to fit a polynomial function with c_0, c_1, c_2, c_3.

$$\min \sum_{i=1}^{k} w_i \left(e_i + \Delta_e^i - (c_0 + c_1 e_i + c_2 e_i^2 + c_3 e_i^3)\right)^2 \tag{6.8}$$

where e_i is the photon energy of the i^{th} peak, $e_i + \Delta_e^i$ is the target energy of the i^{th} peak, and k is the number of peaks used in this calibration step. The weight of each peak is computed as follows:

$$w_i = \frac{1}{\sum_{\text{channels in the } i^{th}\text{peak}} \boldsymbol{m}} \tag{6.9}$$

$\boldsymbol{m}$ is the equivalent background with respect to other spectral contributions with the exception of the radionuclide that emits photons at the i^{th} peak.

To overcome this problem, we can write the coefficients with a vector $\boldsymbol{c} = [c_0, c_1, c_2, c_3]$, by considering the following matrix form:

- Vector $\boldsymbol{e} = [e_1, ...e_k]$ is the photon energies of the k peaks
- Matrix of variables in the polynomial function noted as:

$$\boldsymbol{V} = \begin{pmatrix} 1 & e_1 & e_1^2 & e_1^3 \\ . & . & . & . \\ . & . & . & . \\ 1 & e_k & e_k^2 & e_k^3 \end{pmatrix}$$

- Vector energy shift of peaks: $\Delta_e = [\Delta_e^1, ...\Delta_e^k]$
- Weights matrix $\Sigma = \text{diag}\,(w_1, ...w_k)$

The coefficients can be calculated by solving the following problem:

$$\underset{\boldsymbol{c}}{\text{argmin}}\, \Sigma^{-1} \|\boldsymbol{e} + \Delta_e - \boldsymbol{V}\boldsymbol{c}\|_2^2 \tag{6.10}$$

which leads to:

$$\boldsymbol{c} = \left(\boldsymbol{V}^T \Sigma^{-1} \boldsymbol{V}\right)^{-1} \boldsymbol{V}^T \Sigma^{-1} \left(\boldsymbol{e} + \Delta_e\right) \tag{6.11}$$

Finally, the corrected spectral signatures $\boldsymbol{\Phi}$ can be obtained by interpolating the corrected energy bins (High resolution domain) into energy bins of the measurement.

$$\boldsymbol{\Phi}_f = H\left(c_0 + c_1 E_{hr} + c_2 E_{hr}^2 + c_3 E_{hr}^3\right)$$

where H is the interpolation operator described in Eq.(6.7), and $\boldsymbol{\Phi}_f$ is the final re-calibrated spectral signatures.

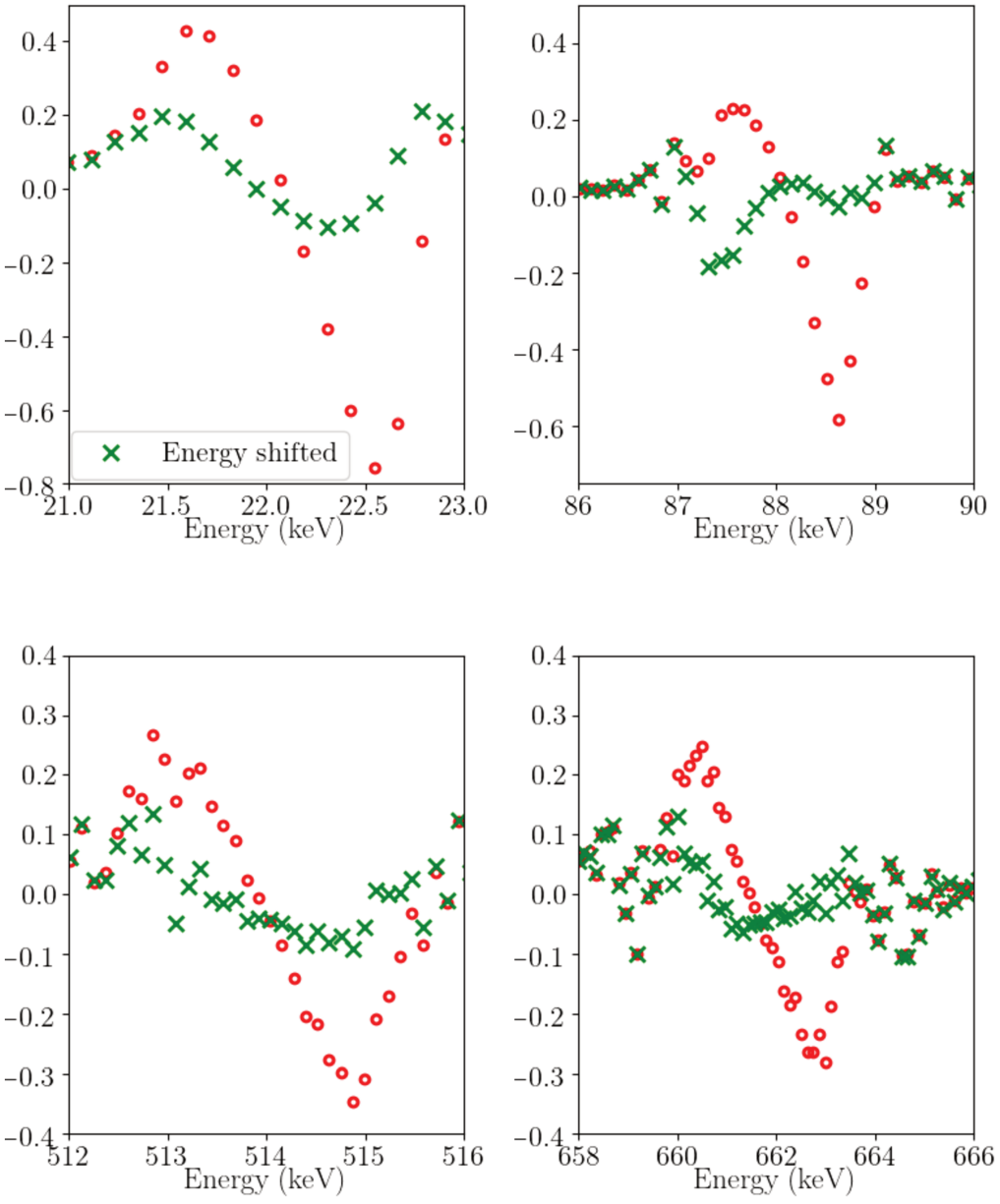

Figure 6.9 – Evaluation of energy calibration in zoomed peak regions, with respect to estimation residual normalized by the observed counts: $\frac{\boldsymbol{x}-\boldsymbol{\Phi a}-\boldsymbol{b}}{\boldsymbol{x}}$. The residual before correction and those obtained after correction are display in points (red) and cross (green) respectively

Evaluation of the energy re-calibration The estimation residual is compared for results that we computed before and after energy correction. These residuals, which are normalized by the observed counts, are displayed for peaks in Figure 6.9. This result highlights that the energy shift correction improves the spectral unmixing, which has significant benefits by reducing the estimation residual in peak regions of the spectrum. For the analysis of HPGe gamma-ray spectrum, where the counts in peaks regions are dominant, we can especially benefit from a significant improvement from this energy re-calibration step.

6.5 Validation with the standard source analysis

In this section, we aim to validate the proposed calibrations with the standard source. For this purpose, the standard source is measured with the calibrated detection system. The measured spectrum is analyzed with the investigated spectral analysis pipeline, which includes the calibration steps presented in previous sections and characteristic limits assessment introduced in Chapter 5.

Uncertainties of the standard source analysis

Before proceeding with the spectral analysis, the main practical problem comes from the uncertainties of the actual measurements. It is well known that the measurement uncertainties contain not only statistical uncertainties of the estimation, but also metrological uncertainties related to the material and the analysis method. In practice, the uncertainties of the results are determined from the probability that the estimated activity is contained in a confidence interval based on a given p-value γ, where $\gamma = 0.05$ is usually taken into account. The uncertainty is according to 2σ for the Normal distribution assumption (*i.e.* k=2). For this purpose, we make use of the relative uncertainties defined with:

$$u = \frac{2\sigma}{\hat{a}}$$

where $\hat{a}$ is the estimated activity.

We establish an uncertainty budget by using the spectral unmixing, which contains the following uncertainty terms:

- For a given radionuclide, the statistical uncertainty with the Fisher information matrix as described in Section 5.4, noted:

$$u_1 = \frac{2\sigma_f}{\hat{a}}$$

where σ_f and $\hat{a}$ stand for the standard deviation calculated from Fisher information matrix and the estimated activity respectively.

- As previously investigated, spectral signatures $\mathbf{\Phi}$ are calibrated with a relative uncertainty of $u_2 = 5\%$.
- The uncertainty of the standard source that used for the calibration: $u_3 = 5\%$.
- The uncertainty to take into account the variation of the sample position, for which we take the same value as considered in Genie 2000 analysis in the laboratory $u_4 = 2\%$.
- The uncertainty associated withthe variation of the detector $u_5 = 5\%$.

The relative uncertainty of the estimated activities can be assessed with the combination of the above uncertainty terms:

$$u = \sqrt{u_1^2 + u_2^2 + u_3^2 + u_4^2 + u_5^2} \tag{6.12}$$

As a result, the activity estimation carried out with the Poisson based spectral unmixing are compared to the reference activities given by the source in Table 6.1. To further evaluate the results, we make use of the ζ_{scores} [ISO 13528, 2015] derived with a standard normal distribution centered at the reference activity:

$$\zeta_{scores} = \frac{\hat{a} - a_{ref}}{\sqrt{\sigma^2 + \sigma_{ref}^2}} \tag{6.13}$$

where $\hat{a}$ and σ are the estimated activity and the standard uncertainty (according to $k = 1$ of Eq.(6.12)), a_{ref} and σ_{ref} represent the activity and uncertainty ($k = 1$) of the reference source.

As reported in Table 6.1, the ζ_{scores} assessed for radionuclides of the standard source satisfies the following criteria:

- $|\zeta_{scores}| \leq 2$ indicates "satisfactory"
- $2 \leq |\zeta_{scores}| \leq 3$ indicates "questionable"
- $|\zeta_{scores}| \geq 3$ indicates "unsatisfactory"

The evaluation of calibrations in spectral unmixing with the standard source allows drawing the following conclusion: the activity and uncertainty estimation with the spectral unmixing method is able to provide quantitative analysis such that close to reference values. It can be used to analyze the aerosol measurements performed with the same detection system.

	source		spectral unmixing		
	reference activity	uncertainty (k=2)	estimated activity	uncertainty (k=2)	$\lvert\zeta_{scores}\rvert$
^{241}Am	50.4	2.2	50.9	4.3	0.201
^{109}Cd	378	21	376	32	0.114
^{57}Co	18.70	0.64	18.70	1.57	0.004
^{139}Ce	14.89	0.63	14.45	1.22	0.644
^{51}Cr	22.6	1.1	23.0	2.0	0.435
^{113}Sn	37.5	1.7	39.1	3.3	0.877
^{85}Sr	23.51	0.91	25.7	2.2	1.888
^{137}Cs	95.8	3.3	99.5	8.4	0.817
^{88}Y	73.9	2.6	75.9	6.4	0.568
^{60}Co	135.0	4.7	136.5	11.5	0.241
^{210}Pb	353.5	9.3	355	30	0.081

Table 6.1 – Results of the standard source analysis with Poisson based spectral unmixing (Bq).

6.6 Experiments on aerosol measurements

6.6.1 Uncertainty budget of the aerosol measurements

The uncertainty terms to analyze spectra performed with the calibrated detection system has been assessed in the previous section. To analyze aerosol measurements, another uncertainty term associated with the variation of the pressed filter needs to be taken into account in the uncertainty budget. More precisely, due to the preparation process of aerosol samples, the thickness and the density of the pressed filter samples are different than those of the standard source, which leads to variations of the detection efficiency.

This uncertainty term is evaluated for the first time during the thesis. To this end, the thickness and the density of 1500 filters of past gamma-ray measurements in the laboratory are measured and the results are summarized in table 6.2.

The spectral analysis procedure is calibrated with the standard source of thickness = 4.64 mm and density = 1.15 g/cm^3, which is however far from the median values of the actual sample geometries. Therefore, to analyze the aerosol measurements, we make use the spectral signatures simulated with

	Thickness (mm)	Density (g/cm^3)
Standard source	**4.64**	**1.15**
2.5%	3.21	0.65
median	3.76	0.77
97.5%	4.79	0.98

Table 6.2 – Variation of aerosol filters' thickness and density.

the median values of thickness = 3.76mm and density = 0.77 g/cm^3 to better reproduce the detector response.

In order to take into account this uncertainty, we compare the detection efficiencies obtained with the geometry configuration according to the 2.5 and 97.5 percentiles of the samples in the archive. The detection efficiencies compare to those obtained with the median values are displayed in Figure 6.10, where the detection efficiencies are calculated in the same manner as in Section 6.2.

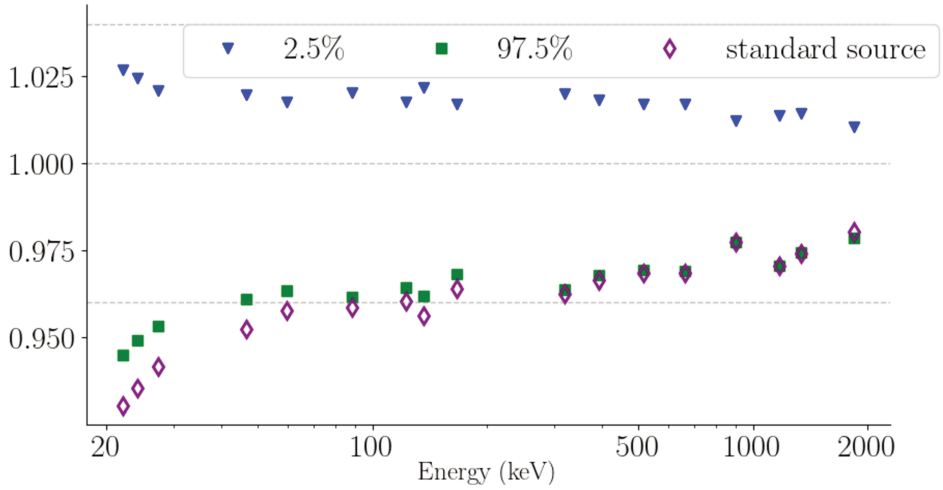

Figure 6.10 – Efficiency ratio comparing to those obtained with the median value: with 2.5 percentile values of the geometry setting (blue), 97.5 percentile values of the geometry setting (green) and the standard source geometry (purple), respectively.

Therefore, we add an uncertainty term of $u_6 = 4\%$ of the source geometry variation into the resulting activities of the spectral unmixing, *i.e.*, combining with other uncertainty terms in Eq.(6.12).

6.6.2 Re-analysis of aerosol measurements

The challenging problem to analyze environment radioactivity measurements is to estimate the activity of low-level radionuclides with high accuracy and high sensitivity. We make use of the Poisson based spectral unmixing to re-analyze past measurements of environmental samples (aerosol filter) performed with the calibrated detection system. The results are carried out with the characteristic limits introduced in Chapter 5 and the evaluated uncertainty budget.

The spectral unmixing is applied to analyze 67 aerosol measurements during the past two years. They have been measured with the calibrated HPGe detector. The results of the estimated activities consist of:

- Activity of radionuclides.
- Assessment of uncertainties.
- Decision threshold of radionuclides derived from statistical test introduced in Chapter 5 with $\alpha = 0.025$.

For a comparison purpose, we focus on the activity estimation of ^{7}Be, ^{22}Na, ^{40}K, ^{137}Cs and ^{210}Pb resulting from the Poisson-based spectral unmixing and Genie 2000. Figure 6.11 illustrates the distribution of the ratio of activities estimated with the two methods:

$$r = \frac{\hat{a}_1}{\hat{a}_2}$$

where $\hat{a}_1$ for Poisson based spectral unmixing and $\hat{a}_2$ for Genie 2000.
The ratio of activity estimations of the two methods show that:

- For ^{7}Be and ^{210}Pb, the estimated activities with the spectral unmixing are systematically lower than those obtained with Genie 2000. Recall that Genie 2000 determines radionuclides' activities with an efficiency curve calibrated from the standard source. However, as we can see in Figure 6.10, the efficiency performed with the source geometry is systematically less efficient than routine measurements, which leads to an over-estimate of the activities. In the proposed spectral unmixing analysis, the spectral signatures are simulated with median values of the geometries' height and density (see Table 6.2 for details).
- For the analysis of low-level radionuclides, the spectral unmixing provides larger activities than Genie 2000. This can be explained by some over-estimation with spectral unmixing or under estimation with Genie 2000 at low statistics. For further validation of low-level radionuclides' quantification, low activity sources of known activities are needed.

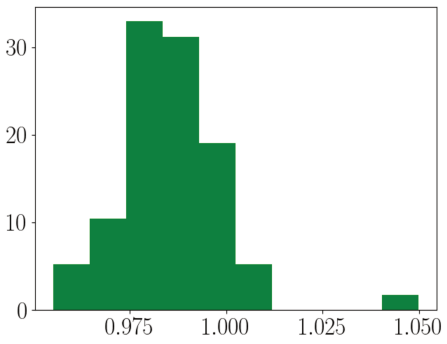

(a) ^{7}Be

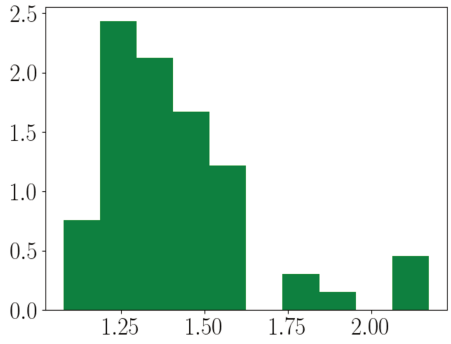

(b) ^{22}Na

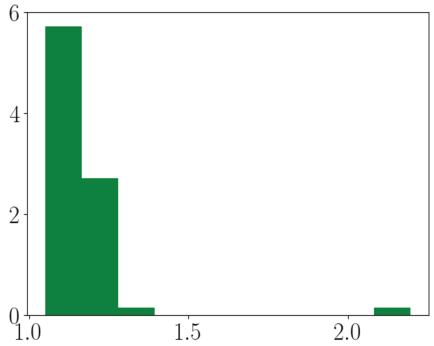

(c) ^{40}K

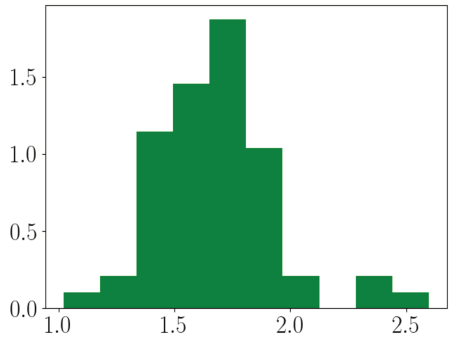

(d) ^{137}Cs

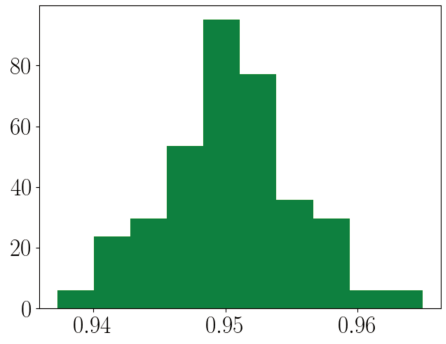

(e) ^{210}Pb

Figure 6.11 – Distribution of ratio between radioactivity estimation with spectral unmixing and Genie 2000 for 67 aerosols measurements.

Furthermore, we compare the activity estimation of the two methods by considering the uncertainties. Figure 6.10 displays the activities estimated with Genie 2000 as a function of those estimated with Poisson based spectral unmixing, where the error bars represent the uncertainties of the results.

In Figure 6.10, the error bars box (red) includes the uncertainties of the results is comparable with the line of $y = x$ (blue) for ^{7}Be, ^{40}K and ^{210}Pb. For ^{22}Na and ^{137}Cs of very low-level activities, the error bars boxes are under the line of $y = x$. The results confirm that the spectral unmixing tends to systematically provides larger activity estimation comparing to the Genie 2000. To interpret the results, the Genie 2000 is likely to over estimate the background when the number of counts in the peak region is low. However, the quantification of low activity radionuclides needs to be further investigated with reference sources.

Next, we focus on the sensibility of the Poisson spectral unmixing analysis to detect the ^{137}Cs at trace level. Table 6.3 reports the activity estimation of ^{137}Cs for 6 of the 67 measurements, for which the ^{137}Cs is not detected with Genie 2000 but with the Poisson based spectral unmixing.

Date	09/07/18	11/10/19	21/03/19	18/10/19	25/10/19	17/12/19
Activity	0.136	0.043	0.045	0.058	0.040	0.054
Uncertainty	0.063	0.025	0.016	0.022	0.019	0.021
DT	0.040	0.016	0.009	0.012	0.011	0.011

Table 6.3 – Activity (μBq/m^3) of ^{137}Cs analyzed with spectral unmixing for measurements when ^{137}Cs is not detected with Genie 2000. Uncertainties are assessed with k=2 (2σ), DT = decision threshold.

The results reported in Table 6.3 are illustrated in Figure 6.11. The detection of ^{137}Cs of these 6 measurements are shown to be significant comparing to the decision threshold, whereas the results are non-significant with Genie 2000, This further confirms the sensibility of the spectral unmixing analysis.

6.7 Conclusion

In this chapter, we investigated the quantitative analysis of experimental aerosol measurements with HPGe gamma-ray spectrometry. Instrumentation calibration procedures of the spectral unmixing are proposed to analyze HPGe measurements using MCNP-CP simulated spectral signatures. To summarize, the quantitative analysis with a given detection system is performed with the following calibration tasks: i), in the simulation process,

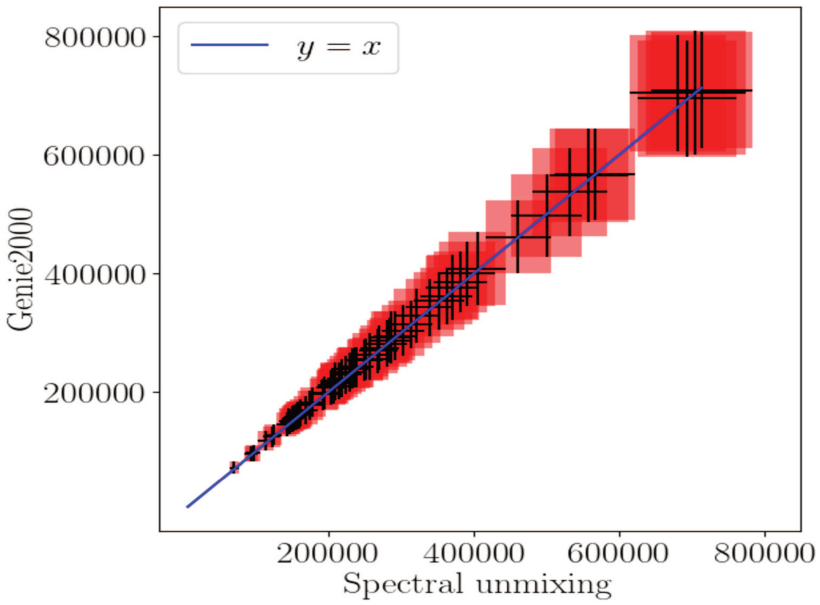
y = x
800000
600000
400000
200000
Genie2000
200000
400000
600000
800000
Spectral unmixing

(a) ^{7}Be

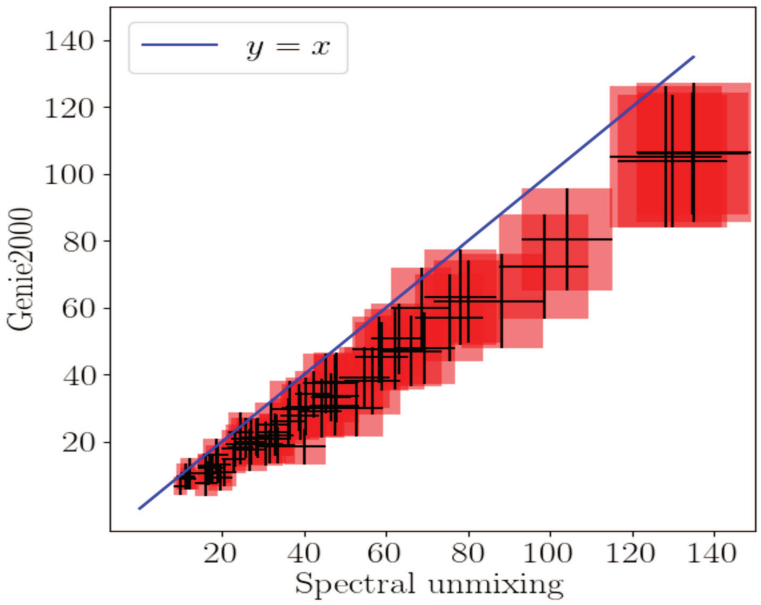
y = x
140
120
100
80
60
40
20
Genie2000
20
40
60
80
100
120
140
Spectral unmixing

(b) ^{22}Na

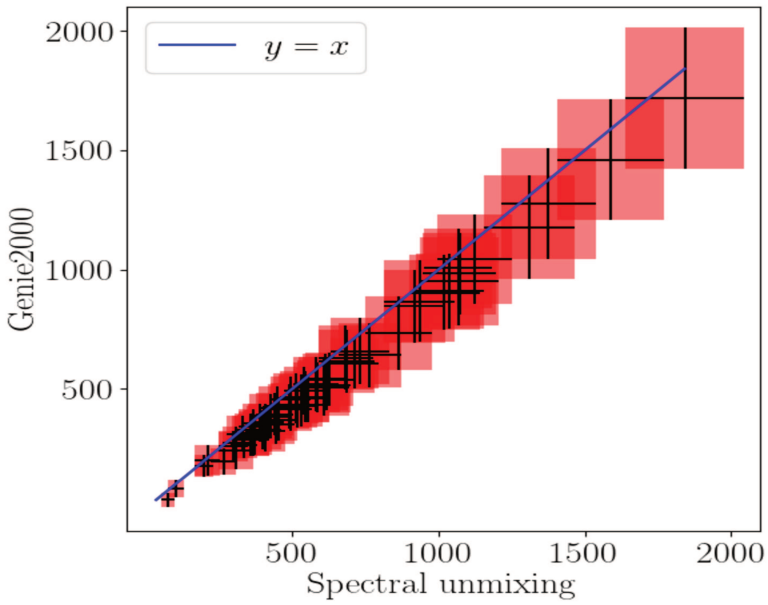
y = x
2000
1500
1000
500
Genie2000
500
1000
1500
2000
Spectral unmixing

(c) ^{40}K

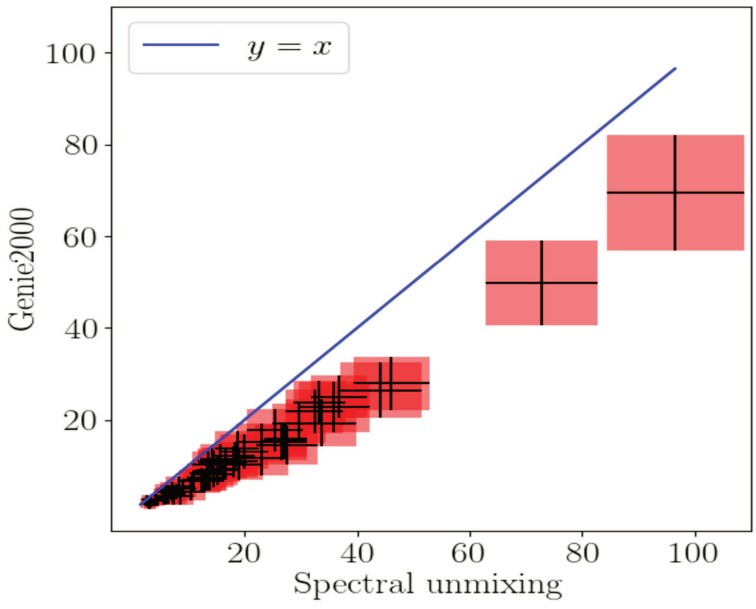
y = x
100
80
60
40
20
Genie2000
20
40
60
80
100
Spectral unmixing

(d) ^{137}Cs

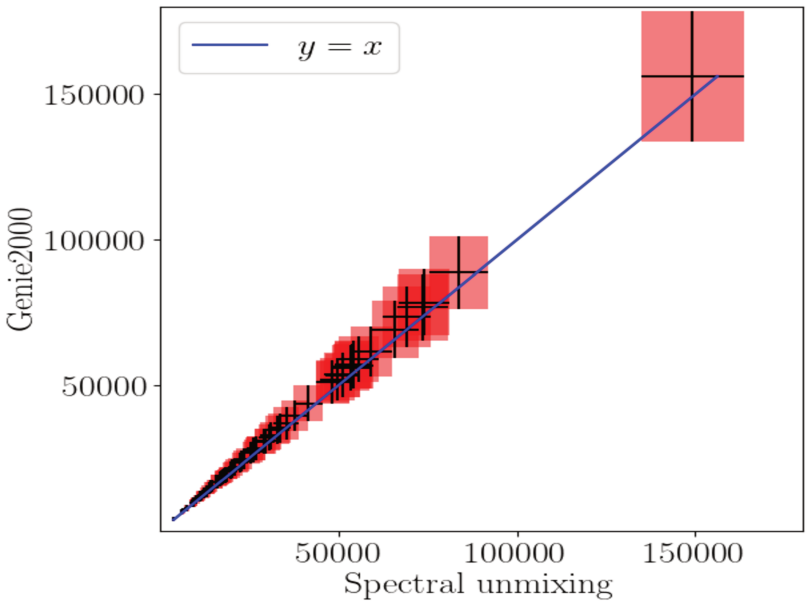

(e) ^{210}Pb

Figure 6.10 – Activity estimation of aerosol measurements with Poisson-based spectral unmixing and Genie 2000. Error bars for activity (mBq) ± uncertainty (k=2) for each measurement.

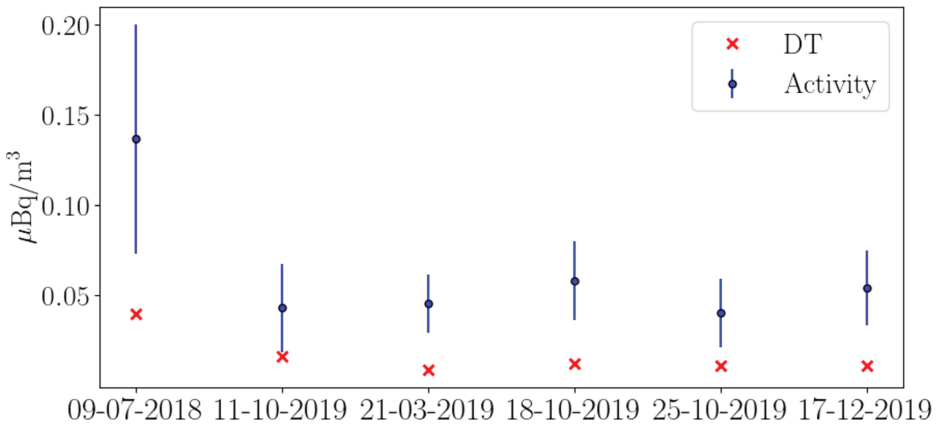

Figure 6.11 – Results obtained with Poisson based spectral unmixing. Activity ± uncertainty of ^{137}Cs (blue), the decision threshold (red).

the efficiency and the resolution are calibrated so that the simulated spectral signatures can reproduce the actual energy response of the detection system, ii) the measured spectrum need to cope with the spectral contributions due to the specific installations of the detection system (*e.g.*, lead shielding) by adding a spectrum into the spectral signatures' dictionary, iii), an energy re-calibration step is proposed to correct the energy shift between energy bins of the simulations and the measured spectrum.

The proposed calibration procedures are evaluated and validated for a detection system with a multi-gamma standard source of known activities. The aerosol measurements performed with this calibrated detection system are subsequently analyzed with the proposed analysis pipeline (characteristic limits + calibrations). The results are compared to those obtained with Genie 2000 analysis. In conclusion, the Poisson based spectral unmixing significantly improves the sensitivity of radionuclides' identification, which is particularly required by the rapid detection and rapid characterization of artificial radionuclides (*e.g.*, ^{137}Cs) under emergency conditions. Future investigations with low-level standard source are necessary to validate the quantification of low-level radionuclides in real data analysis.

CHAPTER 7

Conclusion and perspectives

Contents

7.1 Conclusion 127

7.2 Perspectives 129

7.2.1 Spectral unmixing with temporal signatures 129

7.2.2 Making profit of the past processed data, learn to unmix 133

7.3 Open questions 140

7.4 Publications 142

7.1 Conclusion

The thesis addresses the gamma-ray spectrum analysis problem, which covers both the development of analysis methods and metrological aspects of the radioactivity determination with gamma-ray spectrometry technique. We investigated the spectral unmixing to tackle the identification and quantification of radionuclides with the aim of finding the spectral contributions from a measured gamma-ray spectrum. The proposed spectral unmixing was formulated as a regularized inverse problem that makes use of the observed data in the full energy range and takes into account the Poisson statistics of the underlying physical process.

The spectral unmixing aims at decomposing a measured spectrum into the radionuclides' spectral signatures and a background spectrum. We first tackled the problem in a supervised framework in Chapter 3, where the

spectral signatures and the background spectrum are considered as known. Experiments on both simulated and measured gamma-ray spectra indicated the significant advantages of using the Poisson-based full spectral unmixing. The time to detect the low-level radionuclide ^{137}Cs in aerosol filters was reduced to 4 days after the sampling, whereas we need 8 days with standard analysis method.

In the spectral unmixing problem, the identification of the spectral signatures is usually a challenging problem, it is as well an important issue that we need to cope with in gamma-ray spectrum analysis, since the active radionuclides present in a measurement is actually unknown in advance. For this purpose, we presented the sparse spectral unmixing in Chapter 4. A novel Poisson-based Greedy algorithm has been proposed, it enables to accurately identify the active radionuclides and improves the accuracy of the activity estimation.

Next, the quantitative analysis of the radioactivity measurements by using spectral unmixing methods has been investigated by focusing on different metrological problems. In the field of radioactivity measurements, the characteristic limits need to be assessed. In Chapter 5, we presented the characteristic limits calculation for the spectral unmixing analysis tool investigated in this thesis. In Chapter 6, we proposed the spectrum analysis procedure for experimental gamma-ray measurements, in which the instrumentation calibrations are thoroughly investigated and further evaluated with a detection system used in the laboratory.

The novel spectral unmixing approach has been applied to analyze gamma-ray spectra measurements and compared to standard analysis method, the spectral unmixing is shown to be more sensitive in the task of detecting low-level radionuclides.

In this thesis, we focused on the spectrum analysis of aerosol measurements performed with HPGe detectors. The investigated methods can be further applied to other detectors and other radioactivity measurement domains:

- The measurements with NaI(Tl) detectors are performed by the TRILATAC device designed by IRSN for the radioactivity monitoring in food and feed. The objective of these measurements is to control if the activity in the food and feed samples exceed the maximum permitted levels of radioactive contamination following a nuclear accident or any other case of radiological emergency laid down by the Council Regulation (Euratom) 2016/52. Due to the large number of samples to be measured in this case, fast measurements are particularly required while keeping good identification performance.

- In the framework of controlling illegal nuclear material trafficking, the investigated spectral unmixing method can be applied to measurements using radiation portal monitors with scintillation detectors (plastic, NaI(Tl)) to improve the detection limits.

7.2 Perspectives

7.2.1 Spectral unmixing with temporal signatures

In the thesis, we focused on the analysis of individual gamma-ray spectra, where only information about the signatures in energy of the radionuclides can be used in the unmixing process. In Chapter 3, we investigated the analysis of a temporal sequence of 11 HPGe spectra, which corresponds to a non-standard data acquisition procedure at IRSN. However, for the rapid detection of artificial radionuclides, it is expected that further accounting for the temporal information carried out by the radioactive decay will be beneficial for the accuracy and sensitivity of the spectral unmixing.

More precisely, as presented in Chapter 2, the activity of a given radionuclide at time t can be obtained by an exponential decay function:

$$a[t] = a[0]e^{-\lambda t} \tag{7.1}$$

where $a[0]$ is the activity at $t[0]$. Each radionuclide has a specific decay constant λ, which can further help discriminating between distinct radionuclides. The Poisson unmixing algorithm we investigated in this thesis can be therefore extended to jointly take into account the spectral signatures and the temporal signatures of radionuclides to estimate their activities.

As depicted in Figure 7.1, for a given measurement between two different times t_i and t_j, a radionuclide's activity, noted a^j, is defined as the integral of the activity decay between t_i and t_j:

$$a^j = \int_{t_i}^{t_j} a[0]e^{-\lambda t}dt \tag{7.2}$$

$$= \frac{a[0]}{\lambda}(e^{-\lambda t_i} - e^{-\lambda t_j}) \tag{7.3}$$

In the experiments described in Section 3.5, the time intervals are contiguous, the starting time of some measurement is exactly the ending time of the previous one.

Let's now define by $\mathbf{S}$ the matrix defined as the row-wise concatenation of L temporal measurements, where the j^{th} column of $\mathbf{S}$ defines the measurement ending at time t_j. The mixing model can now be extended to the

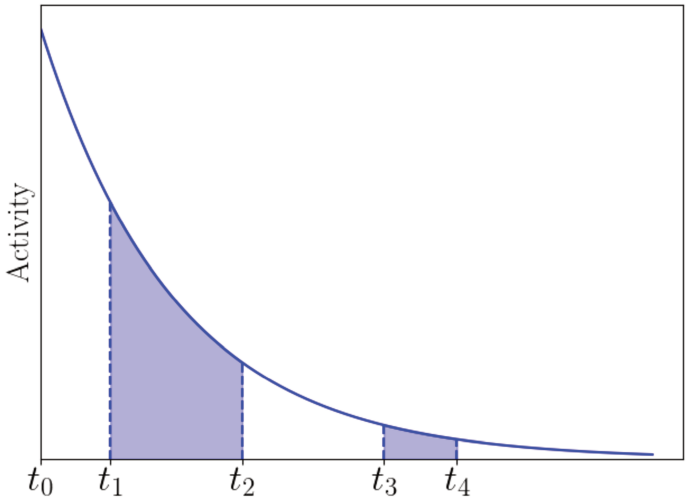

Figure 7.1 – Activity decay illustration

following one:

$$\mathbf{S} = \sum_{k=1}^{N} a_k[0] \mathbf{\Psi}_k \otimes \mathbf{\Phi}_k \tag{7.4}$$

where $a_k[0]$ defines the activity at time t_0 for the k^{th} radionuclide. The signature of a given radionuclide is now bi-dimensional and defined as the tensor product between its temporal signature $\mathbf{\Psi}_k$ and its signature in energy $\mathbf{\Phi}_k$.

The spectral unmixing algorithm we investigated in Section 3.2 can be extended to cope with this new unmixing problem. We hereafter propose to apply such extension to the joint analysis of HPGe measurements we described in Section 3.5, where 11 measurements are successively performed. We make use of the last 5 measurements (*i.e.*, s7-s11) to let the decay chains achieve the state of equilibrium. Briefly speaking, over a determined time, the secular equilibrium can be considered to account for the decay process of radionuclides in a decay chain, which allows considering the same decay constant of the parent radionuclide and its daughter radionuclides.

In brief, these simulations are composed of 5 successive measurements with ^{7}Be, ^{22}Na, ^{40}K, ^{137}Cs, ^{210}Pb, ^{208}Tl, ^{212}Bi, ^{212}Pb, ^{214}Bi, ^{214}Pb. The simulations that mimic realistic radionuclides' activities are described in Table 7.2 (according to experiments in 3.5). For each mixture, 100 Monte Carlo simulations are performed. The actual decay process of 10 radionuclides

are considered in the simulations, where the decay constant of the parent radionuclide is used for its daughter radionuclide (see Table 7.1).

Half-life time	decay chain
10.64 h (^{212}Pb)	^{212}Pb $\rightarrow$ ^{212}Bi $\rightarrow$ ^{208}Tl
26.916 min (^{214}Pb)	^{214}Pb $\rightarrow$ ^{214}Bi

Table 7.1 – Decay constant considered in the equilibrium state.

	start time from collecting	counting time
s7	5.5h	10800
s8	8.5h	54000
s9	23.5h	28000
s10	1day and 7h	240000
s11	4day and 2 h	320000

Table 7.2 – Simulation of measurements for spectral unmixing with temporal signatures.

The temporal/spectral-based unmixing algorithm is compared with our standard Poisson unmixing algorithm based on the relative estimation error. The comparisons are carried out for the 5 radionuclides and featured in Figure 7.2, where the median values and the first and last quartiles are displayed.

Unsurprisingly, further accounting for the temporal information featured by the difference in activity decay of different radionuclides, help improving the estimation accuracy to a large extent. This is especially true for early measurements, where the increased complexity of the measured spectra dramatically hampers the estimation of the low-activity radionuclides. It is also expected that accounting for both temporal and spectral information can help improving the sensitivity and detection abilities of the unmixing process.

Future work will also have to deal with the full complexity of gamma-ray measurements by also accounting for the measurements in which radionuclides are not in equilibrium (*e.g.*, the measurements corresponding to s1-s5 in experiments of Section 3.5). In this case, the activity decay is not known for certain radionuclides, which either requires an hybrid mixture model or a joint estimation of their activity decay.

The preliminary results carried out with the temporal/spectral-based unmixing opens the perspectives of the following applications:

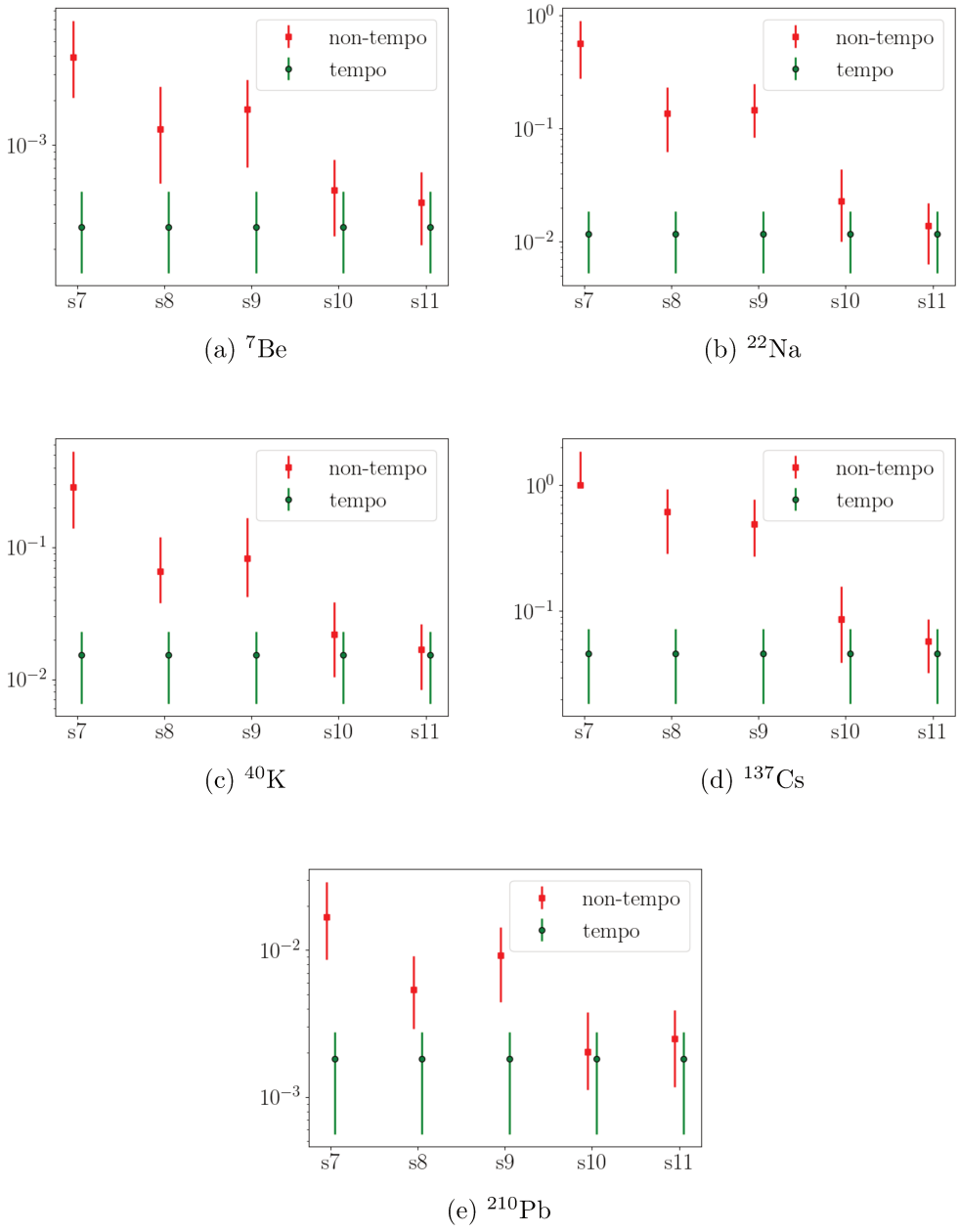

(a) ^{7}Be (b) ^{22}Na

(c) ^{40}K (d) ^{137}Cs

(e) ^{210}Pb

Figure 7.2 – Comparison of estimation errors of spectral unmixing with/without temporal signatures

- New measurement modalities involving sequential temporal measurement that allow better accounting for both the temporal information

(timeline of the measurements) and the spectral information (counting statistics of each measurement).

- Online analysis of aerosol filters collected with high volume air samplers measured with HPGe detectors in LMRE. These samplers, part of the OPERA-Air network of IRSN, are localized all over France and the filters are thus received at LMRE at least 24 hours after sampling; the radon progenies are therefore at equilibrium and the future algorithm taking into account the decay information should improve the radioactivity analysis in terms of sensibility, rapidity and accuracy (bias).

7.2.2 Making profit of the past processed data, learn to unmix

Involved in the radioactivity monitoring work, the laboratory is in charge of gamma-ray spectra measurements with 20 HPGe detectors. 400-500 aerosol filter measurements have been performed per year during the last decade. The unmixing algorithms we introduced during this thesis apply to a single measurement without accounting for the knowledge accumulated from the processing of past measurements. In other words, they are agnostic to the available archive of past measurements, which bring highly valuable information to perform accurate radionuclide activity estimation, especially for the challenging low-statistics regime.

Extracting information from the archive of past processed measurements can be done in several ways. Following a traditional statistical approach would boil down to deriving a statistical model for the past measured radionuclides' activities to build a prior distribution, which can be plugged in our Poisson unmixing algorithm. However, the relationship between the activities of several radionuclides may be intricate and therefore hard to model with simple statistical models.

In contrast, machine learning is a potentially interesting framework to design a model for the sought-after radionuclides' activities that could better account for their complexity. Interestingly, deep unfolding techniques have attracted a growing interest during the last five years [Diamond et al., 2017],[Monga et al., 2019], allowing to combine standard solvers for linear inverse problems with prior model learning. In a nutshell, such methods consist in building a recurrent network that reproduces that inversion process of common optimization algorithms (*e.g.* Forward-Backward Splitting [Gregor and Lecun, 2010, Adler and Öktem, 2017, Andrychowicz et al., 2016] and proximal primal-dual [Adler and Öktem, 2018] algorithms or Neumann Network -NN- [Gilton et al., 2019]) while allowing to learn a data-driven regularization from some training set. An unrolled version of the ADMM

algorithm [Boyd et al., 2011] has been introduced in [Yang et al., 2016] to specifically tackle deconvolution problems in MRI.

For Poisson-based spectral unmixing, we proposed in [Bobin et al., 2019] an unrolled version of the ADMM (alternating directions method of multipliers) algorithm to tackle the underlying maximum Poisson likelihood regression problem along with a learning of a data-driven regularization.

Problem Formulation: Let us recall that a single gamma-ray spectrum $\boldsymbol{x}$ is composed of M samples that measure the number of events in different channels of energy as illustrated in Figure 7.3. It is modeled as the linear combination of N individual radionuclides $\{\phi_i\}_{i=1,\cdots,N}$, to which a background signal $\boldsymbol{b}$ is added. Furthermore, an observation $\boldsymbol{x}$ follows a Poisson distribution:

$$\boldsymbol{x} \sim \mathcal{P}oisson\left(\boldsymbol{\Phi a} + \boldsymbol{b}\right)$$

where $\boldsymbol{\Phi} = [\phi_1, \cdots, \phi_n]$ and the background $\boldsymbol{b}$ are generally known accurately.

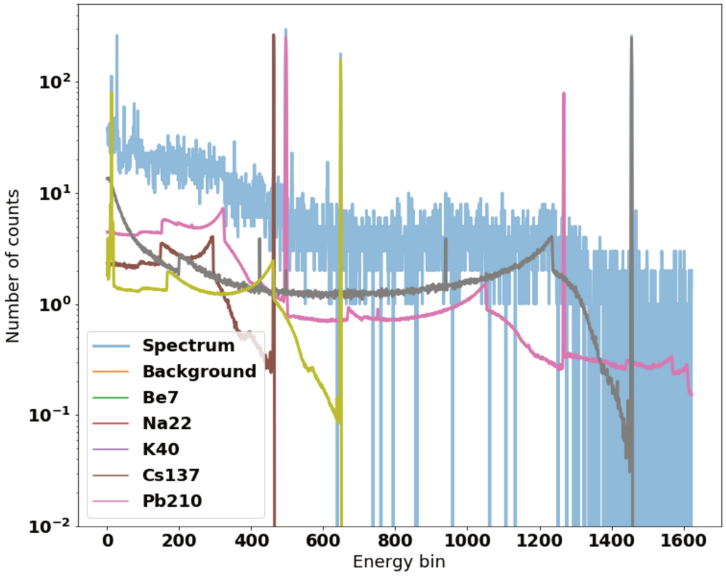

Figure 7.3 – Description of the data: Example of a single spectrum with its individual components.

Based on Poisson statistics, the unmixing problem to be tackled takes the generic form:

$$\min_{\boldsymbol{a}} \lambda \mathcal{J}(\boldsymbol{a}) + \boldsymbol{\Phi a} + \boldsymbol{b} - \boldsymbol{x} \odot \log\left(\boldsymbol{\Phi a} + \boldsymbol{b}\right), \tag{7.5}$$

where $\odot$ is the Hadamard product. The term $\mathcal{J}$ stands for a penalization term based on some prior knowledge about $\boldsymbol{a}$, *e.g.*, non-negativity investigated in Chapter 3. The second term is the neg-log-likelihood of the Poisson distribution. Beyond the non-negativity of $\mathbf{a}$, one could benefit from the available archive of hundreds to thousands of routinely taken measurements to further learn a data-driven prior $\mathcal{J}(\,.\,)$, which should improve both the estimation bias/variance.

In [Bobin et al., 2019], we introduced an unrolled version of the ADMM algorithm to tackle the following equivalent of the problem in Eq.(7.5):

$$\min_{\mathbf{u},\boldsymbol{a}} \max_{\mathbf{v}} \mathcal{J}_{\boldsymbol{\Theta}}(\boldsymbol{a}) + \mathbf{u} - \mathbf{x} \odot \log\left(\mathbf{u}\right) + \mathbf{v}^T(\mathbf{u} - \boldsymbol{\Phi a} - \mathbf{b}) + \frac{\rho}{2}\|\mathbf{u} - \boldsymbol{\Phi a} - \mathbf{b}\|_2^2$$

where $\boldsymbol{u}$ is an extra variable, $\mathbf{v}$ is the dual variable related to the constraint $\mathbf{u} = \boldsymbol{\Phi a} + \mathbf{b}$ and ρ is a positive scalar. The regularization term $\mathcal{J}_{\boldsymbol{\Theta}}$ now depends on some parameters $\boldsymbol{\Theta}$ to be learned from the available training set.

In the present context, the advantage of ADMM is that it allows to split the inversion of spectral signatures dictionary and the application of the regularization in two distinct steps. A single iteration k of the proposed Learned-ADMM, and subsequently each layer of the resulting recurrent network, reads as:

- **Update of u :** minimizing Eq.(7.5) with respect to $\mathbf{u}$ leads to: $\mathbf{u}^{(k+1)} = \text{prox}_{1/\rho\mathcal{P}}\left(\boldsymbol{\Phi a}^{(k)} + \mathbf{b} - 1/\rho\mathbf{v}^{(k)}\right)$, where $\text{prox}_{1/\rho\mathcal{P}}$ is proximal operator of the Poisson neg-likelihood with scaling parameter $1/\rho$ [Combettes and Pesquet, 2007], the proximal operator of the Poisson neg-likelihood is calculated in Appendix B.

- **Update of $\boldsymbol{a}$:** updating $\boldsymbol{a}$ for fixed parameters $\boldsymbol{\Theta}$ is done as follows:

$$\boldsymbol{a}^{(k+1)} = \underset{\boldsymbol{a}}{\text{argmin}}\, \mathcal{J}_{\boldsymbol{\Theta}}(\boldsymbol{a}) + \frac{\rho}{2}\|\boldsymbol{\Phi a} + \mathbf{b} + 1/\rho\mathbf{v}^{(k)} - \mathbf{u}^{(k+1)} - \boldsymbol{a}^{(k)}\|_2^2$$

  Since the dictionary of spectral signatures $\boldsymbol{\Phi}$ is not orthogonal, this problem does not admit a closed-form solution. Instead of resorting to a numerical evaluation with an extra iterative procedure, it is rather approximated with a projected least-square estimate of the form:

$$\boldsymbol{a}^{(k+1)} = \mathcal{R}_{\boldsymbol{\Theta}}\left(\boldsymbol{\Phi}^{\dagger}\left(\mathbf{u}^{(k+1)} - \mathbf{b} + 1/\rho\mathbf{v}^{(k)}\right)\right)$$

where $\mathbf{\Phi}^\dagger$ is the pseudo-inverse of $\mathbf{\Phi}$.

The operator $\mathcal{R}_{\mathbf{\Theta}}$ stands for a *shrinkage* operator that depends on parameters Θ that are updated during training procedure so as to minimize the mean estimation bias of $\sum_p \|\hat{\boldsymbol{a}}_p - \boldsymbol{a}_p^\star\|$, from a training set of T samples $\{(\mathbf{x}_p, \boldsymbol{a}_p^\star)\}_{p=1,\cdots,T}$.

The processing of routine aerosol measurements generally leads to activities that do not vary to a large extent for natural radionuclides (see Figure 7.4). Therefore, the goal of learning $\mathcal{R}_\Theta$ is to capture this standard regime as well as the intricate correlation between the radionuclides' estimated activities.

- **Gradient ascent on v :** the dual variable is updated as: $\mathbf{v}^{(k+1)} = \mathbf{v}^{(k)} + \rho\left(\mathbf{u}^{(k+1)} - \mathbf{\Phi}\boldsymbol{a}^{(k+1)} - \mathbf{b}\right)$. The parameter ρ is also trained along with the inversion procedure.

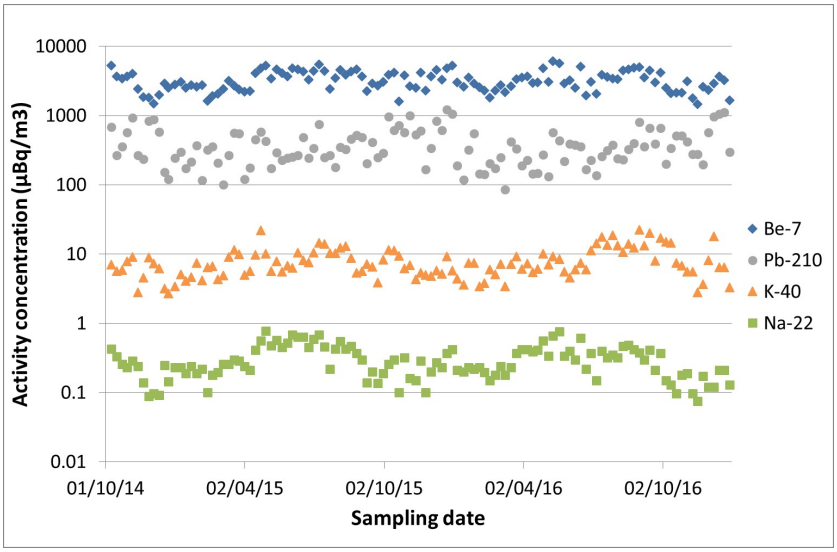

Figure 7.4 – Natural radionuclides activity concentrations in the air sampled in Orsay (France) as a function of the sampling date.

As displayed in Figure 7.5, each recurrent block is composed of a main block where $\boldsymbol{u}$ and $\boldsymbol{a}$ are updated sequentially. The update of the dual variable $\mathbf{v}$ appears externally and is the only variable that explicitly cumulates information in the recurrence; this is reminiscent of skip connections. Several values for the number of recurrent layers L have been tested. In these experiments, $L = 5$ provides the best results; more layers did not provide significant improvements.

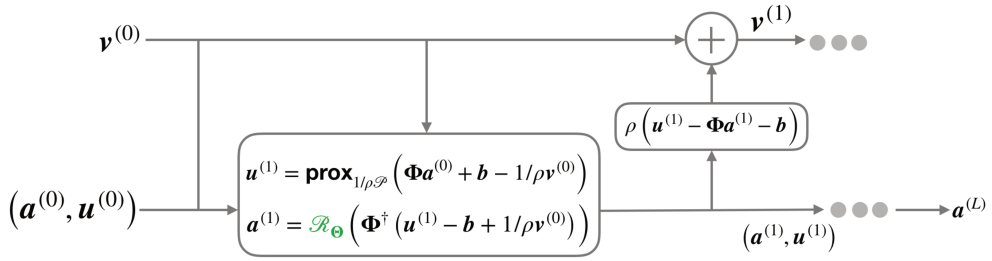

Figure 7.5 – L-ADMM implementation, sketch of a single recurrent layer.

The data-driven shrinkage operator $\mathcal{R}_{\boldsymbol{\Theta}}$ is encoded with a MLP (multi-layer perceptron) with ℓ layers and n hidden units per layer (*i.e.*, one per radionuclide); activation functions are rectified linear units (ReLU). Trainable variables are therefore the weight matrices and the bias for all layers. In this application, $\ell = 2$ and $n = 5$ provided a simple, robust and effective regularization. More complex models with more layers or undercomplete weight matrices did not lead to improved results.

The parameter Θ is learned so as to:

$$\min_{\Theta} \|\boldsymbol{a}^{(L)} - \boldsymbol{a}^{*}\|_2^2 \tag{7.6}$$

However, and in contrast to standard practice in unrolling approaches, learning individual parameters (weights and biases) for each recurrent block yielded significantly better estimation results without increasing the robustness of the training. The proposed network has been implemented with Keras with Tensorflow backend [Chollet et al., 2015], [Abadi et al., 2015]; the ADAM optimizer [Kingma and Ba, 2014] is used with a learning rate of 10^{-4}. The initial first guess for $\mathbf{u}^{(0)}$ and $\mathbf{v}^{(0)}$ set to 0 and $\boldsymbol{a}^{(0)}$ is set as the PoissonML estimate.

Preliminary results: Preliminary experiments have been performed on realistic simulations of gamma-ray spectra refer to Chapter 3. The data are composed of the 4 natural radionuclides that are routinely measured in the environment (^{7}Be, ^{22}Na, ^{40}K, ^{210}Pb) and ^{137}Cs, a commonly sought-after artificial radionuclide. The training and testing sets are composed of $T = 1000$ samples unless stated otherwise; validation is carried out on 10% of the training samples. In these sets, the variability of the simulated activities is based on the levels that are measured on routine measurements as illustrated in Figure 7.3

In these experiments, 4 different algorithms are compared for tackling spectral unmixing problems:

- non-negative Poisson log-likelihood minimization, noted PoissonML (see Chapter 3).
- least-squares with non-negativity constraint, noted LS (see Chapter 3).
- a Neumann Network (NN) with a trainable prior that is similar to the one we implemented in L-ADMM.
- the proposed L-ADMM approach

The robustness of the learning-based approaches with respect to the training set size is evaluated first. For that purpose, the relative bias $|\hat{a} - a^\star|/a^\star$ is computed for each radionuclide. Figure 7.6 displays the results when the mean total number of counts is 15.10^3. The results are shown for ^{7}Be only; similar conclusions can raised for the 4 other radionuclides. The median value as well as the 25% and 75% percentiles across the test set are featured. This shows that for a number of samples larger than 1000, the L-ADMM algorithm provides a significantly smaller bias as well as narrower variance, which is expected with a properly learned prior regularization.

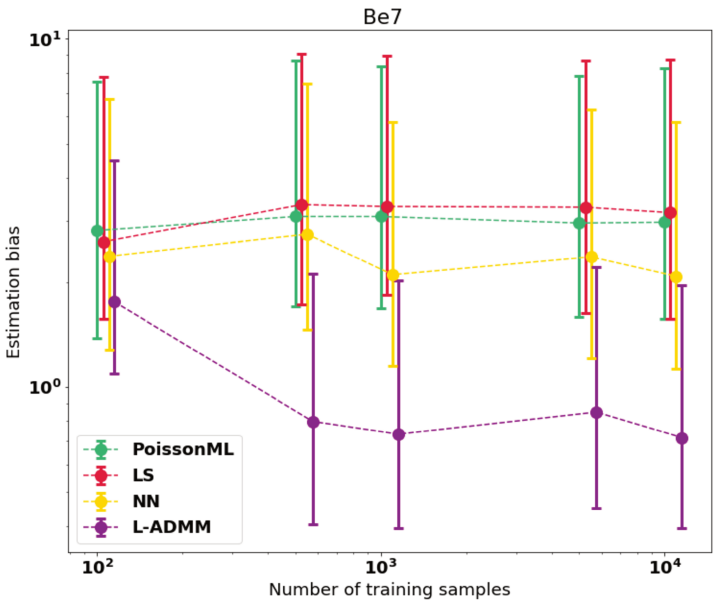

Figure 7.6 – Robustness with respect to the sample size. Relative errors as a function of the sample sizes.

Figure 7.7 displays the evolution of the relative bias for the estimated ^{210}Pb activity when the total number of counts evolves from 15.10^3 to 240.10^3. Unsurprisingly, the bias decreases when the number of counts increases since the noise level decreases. However, the proposed L-ADMM algorithm provides a significantly lower bias, especially for lower number of counts. A similar phenomenon is observed for the NN algorithm when the number of counts is equal to 15.10^3.

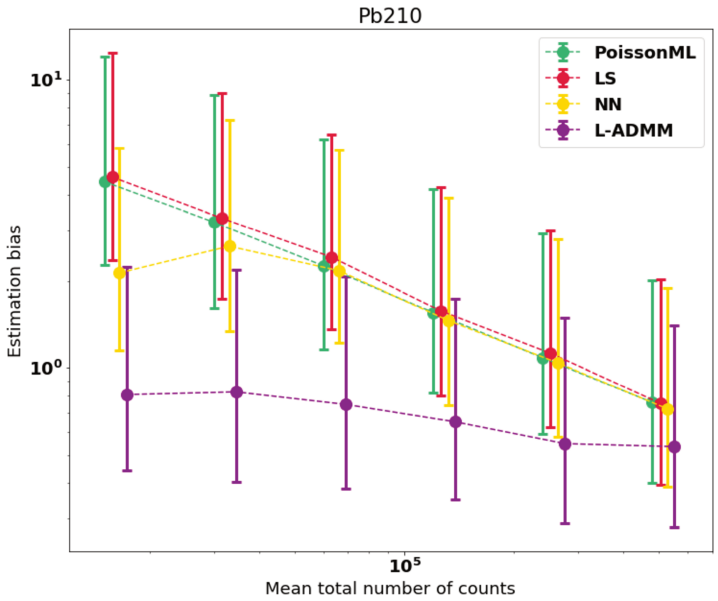

Figure 7.7 – Evolution of the relative bias for the estimated ^{210}Pb activity when the total number of counts evolves from 15.10^3 to 240.10^3.

With these preliminary results, we investigate how deep unrolling can be implemented to design a spectral unmixing algorithm that can precisely account for the statistical modeling of the measurements with learning some regularization based on past processed measurements. Beyond these promising results, future work will focus on combining deep unrolling and model selection to further tackle detection problems. As well, it will require to be thoroughly evaluated with real measurements to assess its applicability to more realistic settings.

Future research might apply to:

- Learn prior of radionuclides' activities from routine measurements of aerosol samples performed in the laboratory. The 4 natural radionu-

clides of interest in aerosol filters have been weekly measured at LMRE with HPGe for several decades (see Figure 7.4 for 2-years period). The learning algorithm allows extracting knowledge of the average levels and the variability of their activity concentrations. Future investigations can also focus on the rapid detection of anomaly events with information learned from these routine measurements.

- Use of high frequency in situ measurements. In situ air measurements are performed by gamma probes, part of the OPERA-Air network of IRSN, for environmental radiation surveillance and early warning purposes. They measure continuously the environmental gamma dose rate. Replacing this probes by new spectrometric probes with NaI(Tl) (e.g. SpectroTracer, Bertin Instruments) would allow to use air measurements by NaI detectors every 10 minutes to improve the analysis tools. A similar approach could be applied to the in situ measurements of the aerosols filters collected by air samplers. For instance, the air samplers of the international network managed by the Comprehensive Nuclear-Test-Ban Treaty Organization (CTBTO) performed one sampling/measurement per day. Using the acquisition of the HPGe daily measurement could improve the analysis tools.

7.3 Open questions

- **Dealing with the variability of the spectral signatures:** It is a question of future research to investigate the variability of the spectral signatures. The detection efficiency varies from one detector to another, using spectral signatures simulated for a detector to analyze spectra measured with other detectors can provide significant estimations bias. For a given detector, the detection efficiency varies when measuring the actual geometries of different dimensions (*e.g.*, 10 mL and 30 mL used in the laboratory).

  We investigated the instrument calibrations in Chapter 6 for quantitative analysis of HPGe gamma-ray measurements. In such context, the efficiency and the resolution of a given detection system (detector + source geometry) are adjusted thanks to a standard source. However, the characteristics of the detector vary over time and lead to variable spectral signatures. Moreover, as discussed in Chapter 6, the dimension and the density of pressed aerosol samples has an impact on the detection efficiency. *e.g.*, Figure 7.8 illustrates the simulated spectra of ^{40}K by slightly changing the configurations of the detector or geometry.

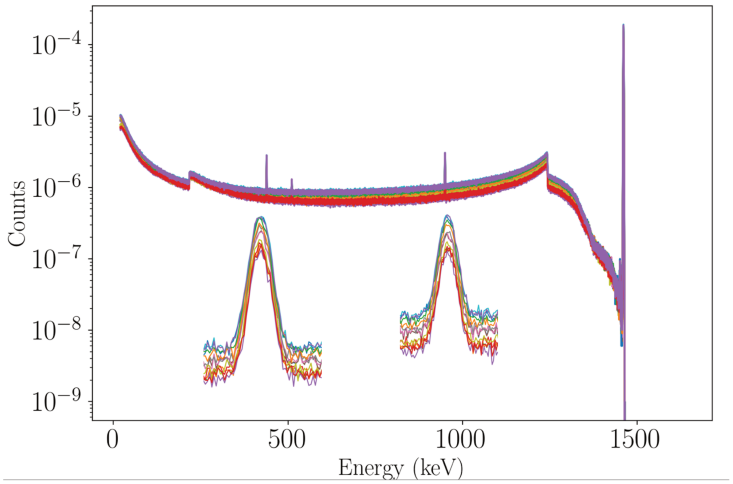

Figure 7.8 – Variability of the spectral signatures of ^{40}K, with zoom-in on the peaks of 439 keV and 950 keV.

To further tackle this problem, the spectral signatures need to be jointly estimated by adding some spectral constraint of $\boldsymbol{\Phi}$:

$$\min_{\boldsymbol{a},\boldsymbol{\Phi}} \; \mathcal{L}\left(\boldsymbol{x}|\boldsymbol{\Phi a}+\boldsymbol{b}\right)+\mathcal{G}\left(\boldsymbol{a}\right)+\mathcal{J}\left(\boldsymbol{\Phi}\right)$$

where $\mathcal{J}\left(\boldsymbol{\Phi}\right)$ would be some regularization on the sought-after spectral signatures.

- **Accounting for the inaccuracy of the background:** In the current spectral unmixing problem, the background radiation spectrum is considered as known. However, the background spectrum at the time of the measurement is unknown. As mentioned in Chapter 2, the background radiation originates from different sources, including the radon progeny (*e.g.*, ^{214}Bi, ^{214}Pb) in the air that varies according to the meteorological conditions. Furthermore, when the system of flushing vapors of liquid nitrogen is defective, we can see large variations of the background spectrum.

  In the laboratory, the background spectrum is measured every two months and used for measurements during the next two months. These measurements allow confirming that the background spectrum is consistent with regular levels. However, the variability of the background still exists and can affect the activity estimation:

  – With the aim of fitting a measured gamma-ray spectrum with the model $\boldsymbol{\Phi a}+\boldsymbol{b}$, the full spectrum analysis is sensitive to the

estimation error of the background $\boldsymbol{b}$, which leads to over/under estimate of radionuclides' activities.

- Moreover, the background spectrum may consists of several radionuclides, which also participate in the measured sample, *e.g.*, ^{40}K, which hampers the estimation accuracy of these radionuclides.

Therefore, it is of interest to jointly estimate the background spectrum in the spectral unmixing problem, which would allow to improve the estimation accuracy of the radionuclides' activities.

7.4 Publications

Papers

- Xu, J., Bobin, J., de Vismes Ott, A., and Bobin, C. (2020). Sparse spectral unmixing for activity estimation in γ-ray spectrometry applied to environmental measurements. *Applied Radiation and Isotopes*, 156:108903.

- André, R., Bobin, C., Bobin, J., Xu, J., and de Vismes Ott, A. Metrological approach of γ-emitting radionuclides identification at low statistics: application of sparse spectral unmixing to scintillation detectors. *Metrologia* in revision.

Papers in preparation

- Analysis of γ-ray spectra with spectral unmixing: determination of characteristic limits. In Prep.

- Calibrations for quantitative analysis of HPGe γ-ray measurements. In Prep.

Presentations

- Sparse spectral unmixing for activity estimation in gamma-ray spectrometry. Oral presentation, International Conference on Radionuclide Metrology and its Applications (ICRM), Salamanca, Spain. 2019.

- Learning to unmix from Poisson measurements with application to γ-spectroscopy. Poster, Signal Processing with Adaptive Sparse Structured Representations (SPARS) workshop, Toulouse, France. 2019.

- learning to unmix in gamma-ray spectrometry. Oral presentation, Journées Machine Learning et Physique Nucléaire, Orsay, France. 2019.

Open source code

The methods developed in this thesis have been tested on both simulated and experimental data. The code will be available at `https://github.com/IRSN-LMRE`.

APPENDIX A

Nuclear data of radionuclides

RN	Element	Z	Half-life	RN	Element	Z	Half-life
^{7}Be	Beryllium	4	53.22 D	^{134}Cs	Cesium	55	2.0644 Y
^{22}Na	Sodium	11	2.6029 Y	^{137}Cs	Cesium	55	30.05 Y
^{40}K	Potassium	19	1.2504E9 Y	^{139}Ce	Cerium	58	137.641 D
^{51}Cr	Chromium	24	27.704 D	^{152}Eu	Europium	63	13.522 Y
^{54}Mn	Manganese	25	312.19 D	^{207}Bi	Bismuth	83	32.9 Y
^{57}Co	Cobalt	27	271.81 D	^{208}Tl	Thallium	81	3.058 M
^{60}Co	Cobalt	27	5.2711 Y	^{210}Pb	Lead	82	22.23 Y
^{85}Sr	Strontium	38	64.850 D	^{212}Bi	Bismuth	83	60.54 M
^{88}Y	Yttrium	39	106.63 D	^{212}Pb	Lead	82	10.64 H
^{106}Rh	Rhodium	45	30.1 S	^{214}Bi	Bismuth	83	19.8 M
^{109}Cd	Cadmium	48	461.9 D	^{214}Pb	Lead	82	26.916 M
^{110m}Ag	Silver	47	249.78 D	^{228}Ac	Actinium	89	6.15 H
^{113}Sn	Tin	50	115.09 D	^{237}Np	Neptunium	93	2.144E6 Y
^{129}I	Iodine	53	16.1E6 Y	^{234}Th	Thorium	90	24.10 D
^{131}I	Iodine	53	8.0233 D	^{241}Am	Americium	95	432.6 Y
^{133}Ba	Barium	56	10.539 Y				

Table A.1 – S = second, M = minute, D = day, Y = year, RN = radionuclide, Z = atomic number.

PERIODIC TABLE

Atomic Properties of the Elements

National Institute of Standards and Technology
U.S. Department of Commerce

Physical Measurement Laboratory www.nist.gov/pml
Standard Reference Data www.nist.gov/srd

FREQUENTLY USED FUNDAMENTAL PHYSICAL CONSTANTS§

1 second = 9 192 631 770 periods of radiation corresponding to the transition between the two hyperfine levels of the ground state of ^{133}Cs

speed of light in vacuum	c	299 792 458 m s^{-1}	(exact)
Planck constant	h	6.626 070 15 x 10^{-34} J Hz^{-1}	(exact)
elementary charge	e	1.602 176 634 x 10^{-19} C	(exact)
Avogadro constant	N_A	6.022 140 76 x 10^{23} mol^{-1}	(exact)
Boltzmann constant	k	1.380 649 x 10^{-23} J K^{-1}	(exact)
electron volt	eV	1.602 176 634 x 10^{-19} J	(exact)
electron mass	m_e	9.109 383 70 x 10^{-31} kg	
energy equivalent	$m_e c^2$	0.510 998 950 MeV	
proton mass	m_p	1.672 621 924 x 10^{-27} kg	
energy equivalent	$m_p c^2$	938.272 088 MeV	
fine-structure constant	α	1/137.035 999	
Rydberg energy	$R_\infty hc$	13.605 693 1230 eV	
Newtonian constant of gravitation	G	6.674 x 10^{-11} m^3 kg^{-1} s^{-2}	

§For the most accurate values of these and other constants, visit pml.nist.gov/constants.

Solids
Liquids
Gases
Artificially Prepared

Group	1 IA	2 IIA	3 IIIB	4 IVB	5 VB	6 VIB	7 VIIB	8	9 VIII	10	11 IB	12 IIB	13 IIIA	14 IVA	15 VA	16 VIA	17 VIIA	18 VIIIA
Period 1	1 $^2S_{1/2}$ **H** Hydrogen 1.008 1s 13.5984																	2 $^1S_0$ **He** Helium 4.0026 $1s^2$ 24.5874
2	3 $^2S_{1/2}$ **Li** Lithium 6.94 $1s^2 2s$ 5.3917	4 $^1S_0$ **Be** Beryllium 9.0122 $1s^2 2s^2$ 9.3227											5 $^2P^o_{1/2}$ **B** Boron 10.81 $1s^2 2s^2 2p$ 8.2980	6 $^3P_0$ **C** Carbon 12.011 $1s^2 2s^2 2p^2$ 11.2603	7 $^4S^o_{3/2}$ **N** Nitrogen 14.007 $1s^2 2s^2 2p^3$ 14.5341	8 $^3P_2$ **O** Oxygen 15.999 $1s^2 2s^2 2p^4$ 13.6181	9 $^2P^o_{3/2}$ **F** Fluorine 18.998 $1s^2 2s^2 2p^5$ 17.4228	10 $^1S_0$ **Ne** Neon 20.180 $1s^2 2s^2 2p^6$ 21.5645
3	11 $^2S_{1/2}$ **Na** Sodium 22.990 [Ne]3s 5.1391	12 $^1S_0$ **Mg** Magnesium 24.305 $[Ne]3s^2$ 7.6462											13 $^2P^o_{1/2}$ **Al** Aluminum 26.982 $[Ne]3s^2 3p$ 5.9858	14 $^3P_0$ **Si** Silicon 28.085 $[Ne]3s^2 3p^2$ 8.1517	15 $^4S^o_{3/2}$ **P** Phosphorus 30.974 $[Ne]3s^2 3p^3$ 10.4867	16 $^3P_2$ **S** Sulfur 32.06 $[Ne]3s^2 3p^4$ 10.3600	17 $^2P^o_{3/2}$ **Cl** Chlorine 35.45 $[Ne]3s^2 3p^5$ 12.9676	18 $^1S_0$ **Ar** Argon 39.948 $[Ne]3s^2 3p^6$ 15.7596
4	19 $^2S_{1/2}$ **K** Potassium 39.098 [Ar]4s 4.3407	20 $^1S_0$ **Ca** Calcium 40.078 $[Ar]4s^2$ 6.1132	21 $^2D_{3/2}$ **Sc** Scandium 44.956 $[Ar]3d4s^2$ 6.5615	22 $^3F_2$ **Ti** Titanium 47.867 $[Ar]3d^2 4s^2$ 6.8281	23 $^4F_{3/2}$ **V** Vanadium 50.942 $[Ar]3d^3 4s^2$ 6.7462	24 $^7S_3$ **Cr** Chromium 51.996 [Ar]3d^{5}4s 6.7665	25 $^6S_{5/2}$ **Mn** Manganese 54.938 $[Ar]3d^5 4s^2$ 7.4340	26 $^5D_4$ **Fe** Iron 55.845 $[Ar]3d^6 4s^2$ 7.9025	27 $^4F_{9/2}$ **Co** Cobalt 58.933 $[Ar]3d^7 4s^2$ 7.8810	28 $^3F_4$ **Ni** Nickel 58.693 $[Ar]3d^8 4s^2$ 7.6399	29 $^2S_{1/2}$ **Cu** Copper 63.546 [Ar]3d^{10}4s 7.7264	30 $^1S_0$ **Zn** Zinc 65.38 $[Ar]3d^{10} 4s^2$ 9.3942	31 $^2P^o_{1/2}$ **Ga** Gallium 69.723 $[Ar]3d^{10} 4s^2 4p$ 5.9993	32 $^3P_0$ **Ge** Germanium 72.630 $[Ar]3d^{10} 4s^2 4p^2$ 7.8994	33 $^4S^o_{3/2}$ **As** Arsenic 74.922 $[Ar]3d^{10} 4s^2 4p^3$ 9.7886	34 $^3P_2$ **Se** Selenium 78.971 $[Ar]3d^{10} 4s^2 4p^4$ 9.7524	35 $^2P^o_{3/2}$ **Br** Bromine 79.904 $[Ar]3d^{10} 4s^2 4p^5$ 11.8138	36 $^1S_0$ **Kr** Krypton 83.798 $[Ar]3d^{10} 4s^2 4p^6$ 13.9996
5	37 $^2S_{1/2}$ **Rb** Rubidium 85.468 [Kr]5s 4.1771	38 $^1S_0$ **Sr** Strontium 87.62 $[Kr]5s^2$ 5.6949	39 $^2D_{3/2}$ **Y** Yttrium 88.906 [Kr]4d5s^2 6.2173	40 $^3F_2$ **Zr** Zirconium 91.224 $[Kr]4d^2 5s^2$ 6.6341	41 $^6D_{1/2}$ **Nb** Niobium 92.906 [Kr]4d^{4}5s 6.7589	42 $^7S_3$ **Mo** Molybdenum 95.95 [Kr]4d^{5}5s 7.0924	43 $^6S_{5/2}$ **Tc** Technetium (97) $[Kr]4d^5 5s^2$ 7.1194	44 $^5F_5$ **Ru** Ruthenium 101.07 [Kr]4d^{7}5s 7.3605	45 $^4F_{9/2}$ **Rh** Rhodium 102.91 [Kr]4d^{8}5s 7.4589	46 $^1S_0$ **Pd** Palladium 106.42 [Kr]4d^{10} 8.3369	47 $^2S_{1/2}$ **Ag** Silver 107.87 [Kr]4d^{10}5s 7.5762	48 $^1S_0$ **Cd** Cadmium 112.41 $[Kr]4d^{10} 5s^2$ 8.9938	49 $^2P^o_{1/2}$ **In** Indium 114.82 $[Kr]4d^{10} 5s^2 5p$ 5.7864	50 $^3P_0$ **Sn** Tin 118.71 $[Kr]4d^{10} 5s^2 5p^2$ 7.3439	51 $^4S^o_{3/2}$ **Sb** Antimony 121.76 $[Kr]4d^{10} 5s^2 5p^3$ 8.6084	52 $^3P_2$ **Te** Tellurium 127.60 $[Kr]4d^{10} 5s^2 5p^4$ 9.0097	53 $^2P^o_{3/2}$ **I** Iodine 126.90 $[Kr]4d^{10} 5s^2 5p^5$ 10.4513	54 $^1S_0$ **Xe** Xenon 131.29 $[Kr]4d^{10} 5s^2 5p^6$ 12.1298
6	55 $^2S_{1/2}$ **Cs** Cesium 132.91 [Xe]6s 3.8939	56 $^1S_0$ **Ba** Barium 137.33 $[Xe]6s^2$ 5.2117		72 $^3F_2$ **Hf** Hafnium 178.49 $[Xe]4f^{14} 5d^2 6s^2$ 6.8251	73 $^4F_{3/2}$ **Ta** Tantalum 180.95 $[Xe]4f^{14} 5d^3 6s^2$ 7.5496	74 $^5D_0$ **W** Tungsten 183.84 $[Xe]4f^{14} 5d^4 6s^2$ 7.8640	75 $^6S_{5/2}$ **Re** Rhenium 186.21 $[Xe]4f^{14} 5d^5 6s^2$ 7.8335	76 $^5D_4$ **Os** Osmium 190.23 $[Xe]4f^{14} 5d^6 6s^2$ 8.4382	77 $^4F_{9/2}$ **Ir** Iridium 192.22 $[Xe]4f^{14} 5d^7 6s^2$ 8.9670	78 $^3D_3$ **Pt** Platinum 195.08 $[Xe]4f^{14} 5d^9 6s$ 8.9588	79 $^2S_{1/2}$ **Au** Gold 196.97 $[Xe]4f^{14} 5d^{10} 6s$ 9.2256	80 $^1S_0$ **Hg** Mercury 200.59 $[Xe]4f^{14} 5d^{10} 6s^2$ 10.4375	81 $^2P^o_{1/2}$ **Tl** Thallium 204.38 [Hg]6p 6.1083	82 $^3P_0$ **Pb** Lead 207.2 $[Hg]6p^2$ 7.4167	83 $^4S^o_{3/2}$ **Bi** Bismuth 208.98 $[Hg]6p^3$ 7.2855	84 $^3P_2$ **Po** Polonium (209) $[Hg]6p^4$ 8.414	85 $^2P^o_{3/2}$ **At** Astatine (210) $[Hg]6p^5$ 9.3175	86 $^1S_0$ **Rn** Radon (222) $[Hg]6p^6$ 10.7485
7	87 $^2S_{1/2}$ **Fr** Francium (223) [Rn]7s 4.0727	88 $^1S_0$ **Ra** Radium (226) $[Rn]7s^2$ 5.2784		104 $^3F_2$ **Rf** Rutherfordium (267) $[Rn]5f^{14} 6d^2 7s^2$ 6.02	105 $^4F_{3/2}$ **Db** Dubnium (268) $[Rn]5f^{14} 6d^3 7s^2$ 6.8	106 ^{0} **Sg** Seaborgium (269) $[Rn]5f^{14} 6d^4 7s^2$ 7.8	107 $^{5/2}$ **Bh** Bohrium (270) $[Rn]5f^{14} 6d^5 7s^2$ 7.7	108 ^{4} **Hs** Hassium (269) $[Rn]5f^{14} 6d^6 7s^2$ 7.6	109 **Mt** Meitnerium (278)	110 **Ds** Darmstadtium (281)	111 **Rg** Roentgenium (282)	112 **Cn** Copernicium (285)	113 **Nh** Nihonium (286)	114 **Fl** Flerovium (289)	115 **Mc** Moscovium (289)	116 **Lv** Livermorium (293)	117 **Ts** Tennessine (294)	118 **Og** Oganesson (294)

Lanthanides	57 $^2D_{3/2}$ **La** Lanthanum 138.91 $[Xe]5d6s^2$ 5.5769	58 $^1G^o_4$ **Ce** Cerium 140.12 $[Xe]4f5d6s^2$ 5.5386	59 $^4I^o_{9/2}$ **Pr** Praseodymium 140.91 $[Xe]4f^3 6s^2$ 5.4702	60 $^5I_4$ **Nd** Neodymium 144.24 $[Xe]4f^4 6s^2$ 5.5250	61 $^6H^o_{5/2}$ **Pm** Promethium (145) $[Xe]4f^5 6s^2$ 5.577	62 $^7F_0$ **Sm** Samarium 150.36 $[Xe]4f^6 6s^2$ 5.6437	63 $^8S^o_{7/2}$ **Eu** Europium 151.96 $[Xe]4f^7 6s^2$ 5.6704	64 $^9D^o_2$ **Gd** Gadolinium 157.25 $[Xe]4f^7 5d6s^2$ 6.1498	65 $^6H^o_{15/2}$ **Tb** Terbium 158.93 $[Xe]4f^9 6s^2$ 5.8638	66 $^5I_8$ **Dy** Dysprosium 162.50 $[Xe]4f^{10} 6s^2$ 5.9391	67 $^4I^o_{15/2}$ **Ho** Holmium 164.93 $[Xe]4f^{11} 6s^2$ 6.0215	68 $^3H_6$ **Er** Erbium 167.26 $[Xe]4f^{12} 6s^2$ 6.1077	69 $^2F^o_{7/2}$ **Tm** Thulium 168.93 $[Xe]4f^{13} 6s^2$ 6.1843	70 $^1S_0$ **Yb** Ytterbium 173.05 $[Xe]4f^{14} 6s^2$ 6.2542	71 $^2D_{3/2}$ **Lu** Lutetium 174.97 $[Xe]4f^{14} 5d6s^2$ 5.4259
Actinides	89 $^2D_{3/2}$ **Ac** Actinium (227) $[Rn]6d7s^2$ 5.3802	90 $^3F_2$ **Th** Thorium 232.04 $[Rn]6d^2 7s^2$ 6.3067	91 $^4K_{11/2}$ **Pa** Protactinium 231.04 $[Rn]5f^2 6d7s^2$ 5.89	92 $^5L_6$ **U** Uranium 238.03 $[Rn]5f^3 6d7s^2$ 6.1941	93 $^6L_{11/2}$ **Np** Neptunium (237) $[Rn]5f^4 6d7s^2$ 6.2655	94 $^7F_0$ **Pu** Plutonium (244) $[Rn]5f^6 7s^2$ 6.0258	95 $^8S^o_{7/2}$ **Am** Americium (243) $[Rn]5f^7 7s^2$ 5.9738	96 $^9D^o_2$ **Cm** Curium (247) $[Rn]5f^7 6d7s^2$ 5.9914	97 $^6H^o_{15/2}$ **Bk** Berkelium (247) $[Rn]5f^9 7s^2$ 6.1978	98 $^5I_8$ **Cf** Californium (251) $[Rn]5f^{10} 7s^2$ 6.2817	99 $^4I^o_{15/2}$ **Es** Einsteinium (252) $[Rn]5f^{11} 7s^2$ 6.3676	100 $^3H_6$ **Fm** Fermium (257) $[Rn]5f^{12} 7s^2$ 6.50	101 $^2F^o_{7/2}$ **Md** Mendelevium (258) $[Rn]5f^{13} 7s^2$ 6.58	102 $^1S_0$ **No** Nobelium (259) $[Rn]5f^{14} 7s^2$ 6.66	103 $^2P^o_{1/2}$ **Lr** Lawrencium (266) $[Rn]5f^{14} 7s^2 7p$ 4.96

Atomic Number — Ground State
Symbol
Name
Standard Atomic Weight†(u)
Ground-state Configuration — Ionization Energy (eV)

58 $^1G^o_4$
Ce
Cerium
140.12
$[Xe]4f5d6s^2$
5.5386

†Based upon ^{12}C. () indicates the mass number of the longest-lived isotope.

For the most precise values and uncertainties visit ciaaw.org and pml.nist.gov/data.

NIST SP 966 (July 2019)

APPENDIX B

Proximal algorithms for spectral unmixing

B.1 Optimization problem underlying the spectral unmixing

As mentioned in Chapter 3, the spectral unmixing aims to solve the minimization of an objective function of the form:

$$\hat{\boldsymbol{a}} \in \underset{\boldsymbol{a}}{\operatorname{argmin}}\, f(\boldsymbol{a}) + g_1(\boldsymbol{a}) + ... + g_n(\boldsymbol{a}) \tag{B.1}$$

More precisely, the above minimization problem in the gamma-ray spectral unmixing problem can be described as follows:

- The data fidelity term $f(\boldsymbol{a})$ associated to least squares error is smooth with a Lipschitz gradient, it can be solved with gradient descent algorithms. However, along with non-differentiable regularization terms such as the non-negativity constraint used in the gamma-ray spectral unmixing, it requires the use of non-smooth optimization algorithms, more specifically the use of proximal algorithms [Parikh and Boyd, 2014].

- In case that we consider the exact Poisson statistics based data fidelity term, which is not differentiable. Along with the non-negativity constraint, none of the two terms is differentiable. Fortunately, both terms admit a proximal operator, which also makes the application of the proximal algorithms.

Involved in solving convex non-smooth optimization problems, the overall advantage of using proximal algorithms is the flexibility and simplicity it provides to add regularization terms. Since the optimization steps in these

algorithms involve the proximal operators of the terms in the objective function independently, such as the non-negativity regularization investigated in Chapter 3 and data-driven regularization terms discussed in Chapter 7.

B.2 Proximal operators and proximal algorithms

B.2.1 Definition of the proximal operator

The proximal operator ([Parikh and Boyd, 2014]) of a closed proper and lower semi-continuous convex function $h : \mathbb{R}^n \cup \infty$ is defined by:

$$\text{prox}_h(y) = \underset{u}{\text{argmin}}\, h(u) + \frac{1}{2}\|u - y\|_2^2 \tag{B.2}$$

where $\|.\|_2$ is the usual Euclidean norm. The function is strongly convex and not everywhere infinite, so it has a unique minimizer for $y \in \mathbb{R}^n$.

The proximal operator of the scaled function ρh with the scale parameter $\rho > 0$ is more commonly used, which can be expressed as:

$$\text{prox}_{\rho h}(y) = \underset{u}{\text{argmin}}\, h(u) + \frac{1}{2\rho}\|u - y\|_2^2 \tag{B.3}$$

For more interpretations of the proximal operators, refer to [Parikh and Boyd, 2014].

B.2.2 Proximal algorithms used in this work

Forward-Backward splitting

The Forward-Backward splitting(FBS) algorithm ([Combettes and Wajs, 2006]) tackles the minimization problem of the form:

$$\hat{\boldsymbol{a}} \in \underset{\boldsymbol{a}}{\text{argmin}}\, f(\boldsymbol{a}) + g(\boldsymbol{a}) \tag{B.4}$$

with f differentiable and g admits a proximal algorithm. In the non-negativity regularized least squares problem described in Chapter 3:

- the data fidelity term:

$$f(\boldsymbol{a}) = \frac{1}{2}\|\boldsymbol{\Phi a} + \boldsymbol{b} - \boldsymbol{x}\|^2 \tag{B.5}$$

  is differentiable, its gradient is:

$$\nabla f(\boldsymbol{a}) = \boldsymbol{\Phi}^T(\boldsymbol{\Phi a} + \boldsymbol{b} - \boldsymbol{x}) \tag{B.6}$$

with Lipschitz constant $L = \|\boldsymbol{\Phi}^{\boldsymbol{T}}\boldsymbol{\Phi}\|_2$, where $\|\,.\,\|_2$ stands for the spectral norm of a matrix (*i.e.,* its largest eigenvalue).

Similarly, when weighted least squares error is considered, in which:

$$f(\boldsymbol{a}) = (\boldsymbol{\Phi a} + \boldsymbol{b} - \boldsymbol{x})^T \boldsymbol{W}^{-1} (\boldsymbol{\Phi a} + \boldsymbol{b} - \boldsymbol{x}) \tag{B.7}$$

the gradient is:

$$\nabla f(\boldsymbol{a}) = \boldsymbol{\Phi}^T \boldsymbol{W}^{-1} (\boldsymbol{\Phi a} + \boldsymbol{b} - \boldsymbol{x}) \tag{B.8}$$

with Lipschitz constant $L = \|\boldsymbol{\Phi}^{\boldsymbol{T}}\boldsymbol{W}^{-\boldsymbol{1}}\boldsymbol{\Phi}\|_2$.

- the regularization term $g(\boldsymbol{a}) = i_{\cdot \boldsymbol{a} \geq 0}$ is convex and admits a proximal operator.

Also known as the proximal gradient algorithm, the minimization step of the FBS algorithm can be described as:

$$\boldsymbol{a}_{(k+1)} = \text{prox}_{\gamma g}\left(\boldsymbol{a}_{(k)} - \gamma \nabla f\left(\boldsymbol{a}_{(k)}\right)\right) \tag{B.9}$$

where the "forward" referring to the gradient step on the differential function f and the "backward" to the proximal step of the function g. The algorithm is guaranteed to converge to the unique minimum when the gradient step $\gamma \leq 1/L$.

Primal-dual algorithm

Recall the Poisson statistics-based activity estimator with non-negativity constraint presented in Chapter 3:

$$\hat{\boldsymbol{a}}_{Poisson} \in \underset{\boldsymbol{a}}{\text{argmin}}\, \boldsymbol{\Phi a} + \boldsymbol{b} - \boldsymbol{x} \odot \log(\boldsymbol{\Phi a} + \boldsymbol{b}) + i_{\cdot \boldsymbol{a} \geq 0} \tag{B.10}$$

In the above optimization problem, none of the two terms is differentiable. Hence, different algorithmic strategies can be considered to design a minimizer. This includes the Alternating Direction Method of Multipliers (ADMM - see [Boyd et al., 2011]) or primal-dual proximal algorithms such as the one introduced by Chambolle and Pock in [Chambolle and Pock, 2011]. In this thesis, we chose the latter as it requires few algorithmic hyperparameters to be tuned, which can further be fixed in a quite easy manner.

More generally, the Chambolle-Pock algorithm aims at tackling optimization problems of the form:

$$\underset{\boldsymbol{a}}{\text{argmin}}\, f(\boldsymbol{\Phi a}) + g(\boldsymbol{a}) \tag{B.11}$$

Recall the convex conjugate of the function f:

$$f^*(\boldsymbol{u}) = <\boldsymbol{\Phi a}, \boldsymbol{u}> - f(\boldsymbol{\Phi a}) \tag{B.12}$$

The dual problem of the minimization of $f(\boldsymbol{\Phi a})$ is:

$$\max_{\boldsymbol{u}} <\boldsymbol{\Phi a}, \boldsymbol{u}> - f^*(\boldsymbol{u}) \tag{B.13}$$

The primal-dual problem of Eq.(B.11) can be therefore written as:

$$\min_{\boldsymbol{a}} \max_{\boldsymbol{u}} <\boldsymbol{\Phi a}, \boldsymbol{u}> - f^*(\boldsymbol{u}) + g(\boldsymbol{a}) \tag{B.14}$$

In the framework of the Chambolle-Pock algorithm, each iteration alternates the minimization on the dual variable $\boldsymbol{u}$ and the primal variable $\boldsymbol{a}$ by calculating the proximal gradient descent, since we can easily get the proximal operators of the function f^* and g. The main minimization step is described as follows:

1. Dual proximal: $\boldsymbol{u}_{(k+1)} = \text{prox}_{\sigma f^*}\left(\boldsymbol{u}_{(k)} + \sigma \boldsymbol{\Phi} \bar{\boldsymbol{a}}_{(k)}\right)$
2. Primal proximal: $\boldsymbol{a}_{(k+1)} = \text{prox}_{\tau g}\left(\boldsymbol{a}_{(k)} - \tau \boldsymbol{\Phi}^T \boldsymbol{u}_{(k+1)}\right)$
3. Update the primal variable: $\bar{\boldsymbol{a}}_{(k+1)} = \boldsymbol{a}_{(k+1)} + \theta\left(\boldsymbol{a}_{(k+1)} - \boldsymbol{a}_{(k)}\right)$

The convergence of the algorithm is ensured with $\sigma\tau \leq 1/L$ and $\theta = 1$.

B.2.3 Proximal operators calculation

The proximal operators of functions used in this work are given as follows:

1. The non-negativity indicator function defined by:

$$i_{\cdot \boldsymbol{a} \geq 0} = \begin{cases} 0, \text{if } \boldsymbol{a} \geq 0 \\ \infty, \text{otherwise} \end{cases} \tag{B.15}$$

   Its proximal operator is defined as the orthogonal projection onto the non-negative orthant:

$$\text{prox}_{i_{\cdot \boldsymbol{a} \geq 0}} = \begin{cases} 0, \text{if } \boldsymbol{a} < 0 \\ \boldsymbol{a}, \text{otherwise} \end{cases} \tag{B.16}$$

2. The negative log-likelihood of the Poisson estimation: $\mathcal{P}oisson\left(x|\lambda\right)$ of the form:

$$f\left(\lambda\right)=\lambda-x\log\left(\lambda\right) \tag{B.17}$$

Its proximal operator is calculated as:

$$\text{prox}_{\rho f}\left(y\right)=\frac{y-\rho+\sqrt{\left(\rho-y\right)^{2}+4\rho x}}{2} \tag{B.18}$$

In the gamma-ray spectrum formulation, we need to calculate the proximal operator of the function:

$$f\left(\boldsymbol{\Phi a}\right)=\left(\boldsymbol{\Phi a}+\boldsymbol{b}\right)-\boldsymbol{x}\odot\left(\boldsymbol{\Phi a}+\boldsymbol{b}\right) \tag{B.19}$$

According to the basic operations of the proximal operator (see [Parikh and Boyd, 2014]), the proximal operator of Eq.(B.19) is:

$$\text{prox}_{\rho f}(\boldsymbol{y})=\frac{\boldsymbol{y}+\boldsymbol{b}-\rho+\sqrt{\left(\rho-\boldsymbol{y}-\boldsymbol{b}\right)^{2}+4\rho\boldsymbol{x}}}{2}-\boldsymbol{b} \tag{B.20}$$

where $\boldsymbol{x}$ and $\boldsymbol{b}$ stand for the measured spectrum and the background spectrum in Eq.(B.19).

3. Refer to [Parikh and Boyd, 2014], by Moreau decomposition, the proximal operator of the convex conjugate of the function f:

$$\text{prox}_{\rho f^{*}}\left(\boldsymbol{v}\right)=\boldsymbol{v}-\rho\text{prox}_{(1/\rho)f}\left(\frac{\boldsymbol{v}}{\rho}\right) \tag{B.21}$$

APPENDIX C

The MCNP simulation code

Gamma-ray spectrum simulations can be performed with Monte Carlo simulation by using different software refer to [Lépy et al., 2019]. In this thesis, we make use of the MCNP simulation process based on the random number generators by taking into account the interaction of particles with materials. The MCNPX and MCNP-CP codes configure the detection system information in the same manner with an input file, which allows us to specify:

- the three-dimensional geometrical cells according to the detection system.
- the material densities and the interaction of particles with materials.

The MCNP can be used for neutron, photon, electron, or coupled neutron/photon/electron transport. The specific configurations for the gamma-ray spectrum simulations are:

- Tally F8 enables to obtain pulse height per emitted particle in the source, which can provide the energy distribution of pulses created in a detector, *i.e.*, a spectrum.
- The E8 card specifies the energy bins of the spectrum.
- By default, the simulation code provides the detector response with photon energy peak as a Dirac. With GEB card option, the parameters of the empirical function:

  $$FWHM = a + b\sqrt{(E + cE^2)}$$

  can be set to reproduce the actual resolution of the experimental measurements (see Section 6.1 for details).

- SDEF card is used to specify the source and its position, in which:
  - the keyword "ERG" in MCNPX specifies the energies for which we aim to simulate the detector response.
  - the keyword "ZAM" in MCNP-CP specifies the radionuclides for which we aim to simulate the detector response with their respective atomic and mass numbers Z and A, M indicates an isomeric state. It simulates the statistical processes accomplished following the disintegration of the given radionuclides, including the cascade emissions, the escape peaks, and the peak sum, with the nuclear data from the Evaluated Nuclear Structure Data File [1]

The spectral signatures used in the experiments in Chapter 6 are performed with MCNP-CP code. To reproduce the actual energy response of a detection system, the simulation input file is configured for the specification of the detector illustrated in Figure C.1.

For a better agreement of the simulated spectral signatures and the actual energy response of the detection system (*i.e.*, efficiency calibration), the configurations of the Ge crystal dimension (see Figure C.2) can be slightly changed with the following principles:

- changing the crystal diameter has an impact of the detection efficiencies on the whole energy range.
- changing the dimension at the bottom of the Ge crystal has an impact of the detection efficiency for source that emit photons at high energy.
- the thickness of the dead layer on the top of the Ge crystal has an impact of the detection efficiency for source that emit photons at low energy.

In summary, the configurations of the Ge crystal dimension is changed by removing $3mm$ thickness from the bottom of Ge Crystal to decrease the efficiency of sources that emit photons at high energy and changing the dead layer of $4\mu m$ to $13\mu m$ in the top of Ge Crystal to decrease the efficiency of sources that emit photons at low energy.

[1] `https://www.iaea.org/resources/databases/evaluated-nuclear-structure-data-file`

S/N 09050

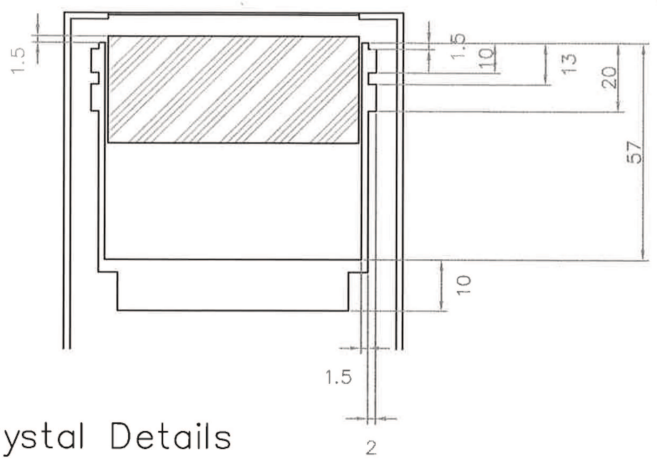

Ge Crystal Details

Outer Electrode Thickness: 0.5 mm
Ge Enterance Window Thickness: 0.4 μm
Crystal Diameter: 81 mm
Crystal Length: 31 mm

Detector Chamber Material Details

Ge front to inside of endcap distance: 5 mm
Cryostat Window Material: Carbon Epoxy Thickness: 0.5 mm
Endcap Material: LB Al Thickness: 1.5 mm
Crystal Holder Material: LB Cu

INNER DRAWING BE - TYPE			Appr.:
Date: 08/05/08		Doc: MCNPBe-type	CANBERRA
MAT:		Auth.: Mar	
SCALE: not to scale	Ra:	BestelNr: b 09050	
TOL:		Aantal:	

Figure C.1 – Detector specification

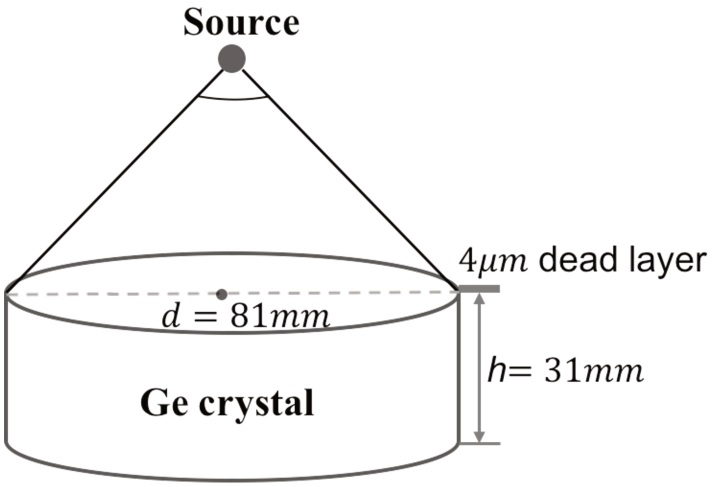

Figure C.2 – The Ge crystal dimensions of the detector.

Bibliography

[Abadi et al., 2015] Abadi, M., Agarwal, A., Barham, P., Brevdo, E., Chen, Z., Citro, C., Corrado, G. S., Davis, A., Dean, J., Devin, M., Ghemawat, S., Goodfellow, I., Harp, A., Irving, G., Isard, M., Jia, Y., Jozefowicz, R., Kaiser, L., Kudlur, M., Levenberg, J., Mané, D., Monga, R., Moore, S., Murray, D., Olah, C., Schuster, M., Shlens, J., Steiner, B., Sutskever, I., Talwar, K., Tucker, P., Vanhoucke, V., Vasudevan, V., Viégas, F., Vinyals, O., Warden, P., Wattenberg, M., Wicke, M., Yu, Y., and Zheng, X. (2015). TensorFlow: Large-scale machine learning on heterogeneous systems. Software available from tensorflow.org.

[Adler and Öktem, 2017] Adler, J. and Öktem, O. (2017). Solving ill-posed inverse problems using iterative deep neural networks. arXiv:1704.04058.

[Adler and Öktem, 2018] Adler, J. and Öktem, O. (2018). Learned primal-dual reconstruction. *IEEE Transactions on Medical Imaging*, 37(6):1322–1332.

[André et al.,] André, R., Bobin, C., Bobin, J., Xu, J., and de Vismes Ott, A. Metrological approach of γ-emitting radionuclides identification at low statistics: application of sparse spectral unmixing to scintillation detectors. revised.

[Andrychowicz et al., 2016] Andrychowicz, M., Denil, M., Gómez, S., Hoffman, M. W., Pfau, D., Schaul, T., Shillingford, B., and de Freitas, N. (2016). Learning to learn by gradient descent by gradient descent. In *Advances in Neural Information Processing Systems 29*, pages 3981–3989.

[Beck and Teboulle, 2009] Beck, A. and Teboulle, M. (2009). A fast iterative shrinkage-thresholding algorithm for linear inverse problems. *SIAM J. Imaging Sciences*, 2:183–202.

[Benjamini and Hochberg, 1995] Benjamini, Y. and Hochberg, Y. (1995). Controlling the false discovery rate - a practical and powerful approach to multiple testing. *J. Royal Statist. Soc., Series B*, 57:289 – 300.

[Berlizov, 2006] Berlizov, A. (2006). *MCNP-CP: A Correlated Particle Radiation Source Extension of a General Purpose Monte Carlo N-Particle Transport Code*, volume 945, pages 183–194.

[Bertero and Bocacci, 1998] Bertero, M. and Bocacci, P. (1998). *Introduction to Inverse Problem in Imaging*.

[Bioucas-Dias et al., 2012] Bioucas-Dias, J. M., Plaza, A., Dobigeon, N., Parente, M., Du, Q., Gader, P., and Chanussot, J. (2012). Hyperspectral unmixing overview: Geometrical, statistical, and sparse regression-based approaches. *IEEE Journal of Selected Topics in Applied Earth Observations and Remote Sensing*, 5(2):354–379.

[Bobin et al., 2019] Bobin, J., Xu, J., de Vismes Ott, A., and Bobin, C. (2019). Learning to unmix from Poisson measurements with application to γ-spectroscopy. In *SPARS 19*, Toulouse, France.

[Boyd et al., 2011] Boyd, S., Parikh, N., Chu, E., Peleato, B., and Eckstein, J. (2011). Distributed optimization and statistical learning via the alternating direction method of multipliers. *Foundations and Trends in Machine Learning*, 3:1–122.

[Briesmeister, 2000] Briesmeister, J. F., editor (2000). *MCNP: A General Monte Carlo N-Particle Transport Code*.

[Caciolli et al., 2012] Caciolli, A., Baldoncini, M., Bezzon, G. P., Broggini, C., Buso, G. P., Callegari, I., Colonna, T., Fiorentini, G., Guastaldi, E., Mantovani, F., Massa, G., Menegazzo, R., Mou, L., Alvarez, C., Shyti, M., Zanon, A., and Xhixha, G. (2012). A new fsa approach for in situ γ ray spectroscopy. *Science of The Total Environment*, 414:639 – 645.

[Chambolle and Pock, 2011] Chambolle, A. and Pock, T. (2011). A first-order primal-dual algorithm for convex problems with applications to imaging. *Journal of Mathematical Imaging and Vision*, 40(1):120–145.

[Chollet et al., 2015] Chollet, F. et al. (2015). Keras. `https://keras.io`.

[Combettes and Pesquet, 2007] Combettes, P. L. and Pesquet, J. (2007). A douglas–rachford splitting approach to nonsmooth convex variational signal recovery. *IEEE Journal of Selected Topics in Signal Processing*, 1(4):564–574.

[Combettes and Wajs, 2006] Combettes, P. L. and Wajs, V. (2006). Signal recovery by proximal forward-backward splitting. *Multiscale Modeling and Simulation*, 4(4):1186–1200.

[DasGupta, 2008] DasGupta, A. (2008). *Asymptotic Theory of Statistics and Probability*.

[Diamond et al., 2017] Diamond, S., Sitzmann, V., Heide, F., and Wetzstein, G. (2017). Unrolled optimization with deep priors. arXiv:1705.08041.

[Dupé and Anthoine, 2013] Dupé, F. and Anthoine, S. (2013). A greedy approach to sparse poisson denoising. In *2013 IEEE International Workshop on Machine Learning for Signal Processing (MLSP)*, pages 1–6.

[Fisher, 1956] Fisher, R. A. (1956). *Statistical methods and scientific inference*. Oliver and Boyd.

[Gilmore, 2008] Gilmore, G. (2008). *Practical Gamma-ray Spectrometry*. Wiley, 2nd edition.

[Gilton et al., 2019] Gilton, D., Ongie, G., and Willett, R. (2019). Neumann networks for inverse problems in imaging. arXiv:1901.03707.

[Gregor and Lecun, 2010] Gregor, K. and Lecun, Y. (2010). Learning fast approximations of sparse coding. Proc. Int'l Conf. Machine Learning.

[Hendriks et al., 2001] Hendriks, P. H. G. M., Limburg, J., and de Meijer, R. J. (2001). Full-spectrum analysis of natural γ-ray spectra. *Journal of Environmental Radioactivity*, 53(3):365–380.

[IEC 62484:2010, 2010] IEC 62484:2010 (2010). Radiation protection instrumentation - spectroscopy-based portal monitors used for the detection and identification of illicit trafficking of radioactive material.

[ISO 11929, 2010] ISO 11929 (2010). Determination of the characteristic limits (decision threshold, detection limit and limits of the confidence interval) for measurements of ionizing radiation — fundamentals and application.

[ISO 13528, 2015] ISO 13528 (2015). Statistical methods for use in proficiency testing by interlaboratory comparison.

[Jeong et al., 2014] Jeong, M., Lee, K. B., Kim, K. J., Lee, M.-K., and Han, J.-B. (2014). Gamma-ray Full Spectrum Analysis for Environmental Radioactivity by HPGe Detector. *Journal of Astronomy and Space Sciences*, 31:317–323.

[Keshava and Mustard, 2002] Keshava, N. and Mustard, J. F. (2002). Spectral unmixing. *IEEE Signal Processing Magazine*, 19(1):44–57.

[Kingma and Ba, 2014] Kingma, D. P. and Ba, J. (2014). Adam: A method for stochastic optimization. cite arxiv:1412.6980Comment: Published as a conference paper at the 3rd International Conference for Learning Representations, San Diego, 2015.

[Kirkpatrick and Young, 2009] Kirkpatrick, J. M. and Young, B. M. (2009). Poisson statistical methods for the analysis of low-count gamma spectra. *IEEE Transactions on Nuclear Science*, 56(3):1278–1282.

[Knoll, 2010] Knoll, G. F. (2010). *Radiation Detection and Measurement*. Wiley, 4th edition.

[Lee and Seung, 2001] Lee, D. and Seung, H. (2001). Algorithms for non-negative matrix factorization. *In Advances in Neural Information Processing*, 13.

[Lépy et al., 2019] Lépy, M., Thiam, C., Anagnostakis, M., Galea, R., Gurau, D., Hurtado, S., Karfopoulos, K., Liang, J., Liu, H., Luca, A., Mitsios, I., Potiriadis, C., Savva, M. I., Thanh, T. T., Thomas, V., Townson, R. W., Vasilopoulou, T., and Zhang, M. (2019). A benchmark for monte carlo simulation in gamma-ray spectrometry. *Applied Radiation and Isotopes*, 154:108850.

[Mallat and Zhang, 1993] Mallat, S. G. and Zhang, Z. (1993). Matching pursuits with time-frequency dictionaries. *IEEE Transactions on Signal Processing*, 41(12):3397–3415.

[Michel, 2016] Michel, R. (2016). Measuring, estimating, and deciding under uncertainty. *Applied Radiation and Isotopes*, 109:6–11.

[Monga et al., 2019] Monga, V., Li, Y., and Eldar, Y. C. (2019). Algorithm unrolling: Interpretable, efficient deep learning for signal and image processing. arXiv:1912.10557.

[Paradis et al., 2020] Paradis, H., Bobin, C., Bobin, J., Bouchard, J., Lourenço, V., Thiam, C., André, R., Ferreux, L., de Vismes Ott, A., and Thévenin, M. (2020). Spectral unmixing applied to fast identification of γ-emitting radionuclides using NaI(Tl) detectors. *Applied Radiation and Isotopes*, 158:109068.

[Parikh and Boyd, 2014] Parikh, N. and Boyd, S. (2014). Proximal algorithms. *Foundations and Trends in Optimization*, 1(3):127–239.

[Pati et al., 1993] Pati, Y. C., Rezaiifar, R., and Krishnaprasad, P. S. (1993). Orthogonal matching pursuit: recursive function approximation with applications to wavelet decomposition. In *Proceedings of 27th Asilomar Conference on Signals, Systems and Computers*, volume 1, pages 40–44.

[Pelowitz, 2011] Pelowitz, D. B., editor (2011). *MCNPX Users Manual Version 2.7.0*. LA-CP-11-00438.

[Sharma et al., 2012] Sharma, S., Bellinger, C., Japkowicz, N., Berg, R., and Ungar, K. (2012). Anomaly detection in gamma ray spectra: A machine learning perspective. In *2012 IEEE Symposium on Computational Intelligence for Security and Defence Applications*, pages 1–8.

[Spiegelhalter et al., 2002] Spiegelhalter, D. J., Best, N. G., Carlin, B. P., and Van Der Linde, A. (2002). Bayesian measures of model complexity and fit. *Journal of the Royal Statistical Society: Series B (Statistical Methodology)*, 64(4):583–639.

[Stoica and Selen, 2004] Stoica, P. and Selen, Y. (2004). Model-order selection: a review of information criterion rules. *IEEE Signal Processing Magazine*, 21(4):36–47.

[Weise et al., 2005] Weise, K., Hübel, K., Michel, R., Rose, E., Schläger, M., Schrammel, D., and Täschner, M. (2005). Determination of the detection limit and decision threshold for ionizing-radiation measurements: fundamentals and particular applications. ISSN 1013-4506.

[Yang et al., 2016] Yang, Y., Sun, J., Li, H., and Xu, Z. (2016). Deep ADMM-net for compressive sensing MRI. pages 10–18.

[Yoshida et al., 2002] Yoshida, E., Shizuma, K., Endo, S., and Oka, T. (2002). Application of neural networks for the analysis of gamma-ray spectra measured with a ge spectrometer. *Nuclear Instruments and Methods in Physics Research Section A Accelerators Spectrometers Detectors and Associated Equipment*, 484(1-3):557–563.

université PARIS-SACLAY

ÉCOLE DOCTORALE
Sciences et technologies de l'information et de la communication (STIC)

Titre: Développement d'outils d'aide à l'expertise en spectrométrie gamma

Mots clés: Spectrométrie gamma, Séparation de source, Optimisation convexe, Algorithmes gloutons

Résumé: La spectrométrie gamma est une des techniques principales pour la mesure de la radioactivité, qui permet d'identifier et quantifier les radionucléides. L'objectif de la thèse est de développer de nouvelles méthodes danalyse des spectres gamma afin d'améliorer les limites de détection. Dans ce contexte, la première contribution est la proposition de nouvelle approches statistiques pour l'estimation des activités en spectrométrie gamma par le démélange spectral, qui consiste à décomposer un spectre gamma mesuré en spectres individuels des radionucléides. Contrairement aux méthodes standard, cette approche permet de traiter un spectre gamma dans sa globalité et prendre en compte la statistique Poisson du processus de détection. En modélisant l'estimation des activités comme un problème inverse sous la contrainte de non- négativité, le démélange spectral parcimonieuse est étudié pour estimer conjointement l'ensemble des radionucléides actifs et leurs activités. La deuxième contribution est l'utilisation métrologique du démélange spectral étudié, qui nécessite en plus l'évaluation des limites caractéristiques pour la prise de décision et l'étalonnage des instruments pour l'analyse quantitative.

Title: Development of analysis tools for gamma-ray spectrometry

Keywords: Gamma-ray spectrometry, Source separation, Convex optimization, Greedy algorithms

Abstract: Gamma-ray spectrometry is one of the main techniques used for the radioactivity measurement, which allows identifying and quantifying radionuclides. The objective of this thesis is to develop new spectrum analysis methods to improve the detection limits. In this context, the first contribution is investigating the activity estimation in gamma-ray spectrometry with spectral unmixing, which decomposes a measured spectrum into individual spectra of radionuclides. Contrary to standard methods, this approach allows accounting for the full spectrum analysis of a gamma-ray spectrum and the Poisson statistics underlying the detection process. By formulating the activity estimation as an inverse problem under non-negativity constraint, the sparse spectral unmixing is investigated to estimate the subset of active radionuclides and their activities jointly. The second contribution is the metrological use of the spectral unmixing, which further necessitates evaluating characteristic limits for decision making purposes and the instruments calibration for quantitative analysis.

Université Paris-Saclay
Espace Technologique / Immeuble Discovery
Route de lOrme aux Merisiers RD 128 / 91190 Saint-Aubin, France